UNIVERSITAT POLITÈCNICA DE VALÈNCIA

Department of Electronic Engineering

Non-invasive Reconstruction of the Myocardial Electrical Activity from Body Surface Potential Recordings

PhD THESIS

Author:
Jorge Pedrón Torrecilla

Supervisors:
María de la Salud Guillem Sánchez
José Millet Roig

Valencia, November 2015

Non-invasive Reconstruction of the Myocardial Electrical Activity from Body Surface Potential Recordings

---

Jorge Pedrón Torrecilla

Dirigida por:
María de la Salud Guillem Sánchez
José Millet Roig

Valencia, Noviembre de 2015

A mi familia y amigos por su comprensión y apoyo incondicional a lo largo de todos estos años.

A mi padre por escuchar mis lamentos y alegrías. Gracias por creer siempre en mí.

Y sobre todo, a mi madre, que, aunque no pueda tenerla cerca, sé que siempre está a mi lado y me acompaña. Todos mis éxitos y logros han sido gracias a ti mamá.

Agradecimientos

Esta tesis doctoral no habría sido posible sin el apoyo científico y personal que he recibido durante todos estos años. A todos ellos quiero expresarles mi más sincero agradecimiento.

A todos mis compañeros de BioITACA, por haber compartido conmigo su experiencia, conocimiento y buenos momentos. Gracias a todos ellos por haberme acompañado en este viaje: María, Andreu, Alex, Miquel, Ramón, Edu, Conra, Xavi, Isma, Adolfo, Cristina, Santi, Paco, Raquel, Toni, Álvaro y Pepe.

A María Guillem y Andreu Climent por su interés y esfuerzo por enseñarme a ser un buen investigador y guiarme a lo largo de estos años de trabajo.

A José Millet por haberme recibido con los brazos abiertos y haberme permitido trabajar en BioITACA.

A Alejandro Liberos y Miguel Rodrigo cuyos modelos matemáticos celulares y estudios sobre el análisis de fase fueron cruciales para el desarrollo de esta tesis.

A los doctores Atienza, Fernández-Avilés, Pérez-David, Josep y Ramón Brugada por permitirnos tomar registros de sus pacientes y su interés por el proyecto.

Al Dr. Berenfeld por sus sabios consejos y recomendaciones.

A todos los pacientes y voluntarios que han participado en los estudios realizados. Sin su colaboración esto no habría sido posible.

CONTENTS

Acronyms

AF	Atrial Fibrillation
AFL	Atrial Flutter
AV	Atrio Ventricular node
AP	Action Potential
BB	Bachmann's Bundle
BEM	Boundary Element Method
BSPM	Body Surface Potential Mapping
BrS	Brugada Syndrome
CAT	Computer Axial Tomography
CFAE	Complex Fractionated Atrial Electrogram
CS	Coronary Sinus
DF	Dominant Frequency
ECG	Electrocardiogram
EGM	Electrogram
FDM	Finite Difference Method
FEM	Finite Element Method
FP	Forward Problem
icEGM	Inverse-computed Electrogram
ICD	Implantable Cardioverter Defibrillator
IPP	Inferioposterior Pathway
IP	Inverse Problem
LA	Left Atrium
LSPV	Left Superior Pulmonary Veins
MRI	Magnetic Resonance Imaging
PV	Pulmonary Vein
RA	Right Atrium

RAA	Right Atrial Appendage
RDM	Relative Difference Measure
RSPV	Right Superior Pulmonary Veins
RVOT	Right Ventricular Outflow Tract
SPDB	Surface Potential Data Base
SR	Sinus Rhythm
SNR	Signal-to-Noise Ratio
VT	Ventricular Tachycardia
VF	Ventricular Fibrillation

Abstract

The behavior of the heart is governed by electrical currents generated in the myocardium, and therefore, the study of the cardiac electrical activity is essential for the diagnosis of cardiac diseases. Electrical currents in the myocardium generate an electric field that propagates through the conductive tissues of the body to reach the torso surface and, consequently, recording the surface potential distribution provides indirect information of the myocardial behavior. The "Body Surface Potential Mapping" (BSPM) technique allows the noninvasive multichannel recording on the surface of the torso, providing a more complete view of the electrical activity by observing events undetectable by conventional techniques.

The mathematical relationship between the myocardial electrical activity and fields recorded on the torso surface can be found by solving either the forward or the inverse problem of electrocardiography. The forward problem of electrocardiography entails the calculation of the torso potentials from the electrical activity of the heart and the 3D body model, while the inverse problem resolution allows the noninvasive reconstruction of the electrical activity of the heart from surface potentials. The inverse problem is of great importance in clinical applications since it allows estimating the electrical activity of the myocardium with only noninvasive recordings. However, inverse problem resolution is still a big challenge in electrocardiography since it is ill-posed, very unstable and has multiple solutions.

In this thesis different algorithms and strategies based on the inverse problem resolution were developed and applied in the noninvasive diagnosis of ventricular and atrial arrhythmias and evaluated with mathematical cellular models and clinical data bases. The thesis focuses on the inverse problem resolution for the noninvasive reconstruction of the myocardial electrical activity for different diseases and propagation patterns, implementing a novel system for complex propagation patterns. The results obtained and propagation patterns were evaluated and classified with the corresponding optimal resolution strategy that minimizes the error and increases the stability of the system, proving its advantages and disadvantages depending on the different diseases and their activation pattern.

A novel iterative method was implemented for the inverse problem dipolar resolution optimized for representing simple propagation patterns, achieving a high stability and robustness against noise by constraining the solution to a limited number of dipoles. However, propagation patterns not representable by few dipoles need to be computed with the inverse problem in terms of epicardial solutions which provide a more detailed estimation of the myocardial activity. Inverse problem resolution in the voltage and phase domains showed a good accuracy for simple and organized propagation patterns. This method allowed the noninvasive diagnosis of

the Brugada syndrome or the location of ectopic focus in atrial arrhythmias by performing a parametric analysis of the electrograms morphology or the activation map reconstruction. However, mathematical and patient results presented in this thesis proved that, for complex propagation patterns like atrial fibrillation (AF), inverse solutions in the voltage and phase domains are over-smoothed and over-optimistic, simplifying the complex AF activity, leading to non-physiological results that do not match the complex intracardiac electrograms recorded in AF patients. In this thesis we proposed a novel technique for the noninvasive identification and location of high dominant frequency AF sources, based on the assumption that in many cases atrial drivers present the highest activation rate with an intermittent propagation to the rest of the tissue that activates at a slower rate. Although, voltage and phase inverse solutions for AF complex propagation patterns were over smoothed and inaccurate, the noninvasive estimation of frequency maps was significantly more accurate, allowing the identification of the AF frequency gradient and location of high frequency sources. This technique may help in planning ablation procedures, avoiding unnecessary interseptal punctures for right-to-left frequency gradients cases and facilitating the targeting of AF drivers, reducing risk and time of the clinical procedure.

Resumen

El comportamiento del corazón se rige por corrientes eléctricas generadas en el miocardio y, por lo tanto, el estudio de su actividad eléctrica es esencial para el diagnóstico de enfermedades cardíacas. Las corrientes eléctricas en el miocardio generan un campo eléctrico que se propaga a través de los tejidos conductores del cuerpo alcanzando la superficie del torso y, por lo tanto, el registro de la distribución de los potenciales de superficie proporciona información sobre el comportamiento eléctrico del miocardio. La técnica del mapeo de potenciales de superficie permite el registro multicanal en la superficie del torso, proporcionando información completa de la actividad eléctrica cardiaca, observando eventos indetectables mediante técnicas convencionales.

La relación matemática entre la actividad eléctrica del miocardio y los campos registrados en la superficie del torso pueden obtenerse mediante la resolución del problema directo o inverso de la electrocardiografía. El problema directo de la electrocardiografía implica el cálculo de los potenciales del torso a partir de la actividad eléctrica del corazón y el modelo 3D del cuerpo, mientras que la resolución del problema inverso permite la reconstrucción no invasiva de la actividad eléctrica del corazón a partir de los potenciales de superficie. La resolución del problema inverso de la electrocardiografía tiene una gran importancia en la práctica clínica dado que hace posible la estimación de la actividad eléctrica del miocardio únicamente a partir de registros no invasivos. Sin embargo, la resolución del problema inverso sigue siendo un gran desafío para la electrocardiografía ya que está mal planteado, es muy inestable y tiene múltiples soluciones.

A lo largo de esta tesis se han desarrollado diferentes estrategias basadas en la resolución del problema inverso, aplicándolas en el diagnóstico no invasivo de arritmias ventriculares y auriculares, verificándolas mediante modelos celulares matemáticos y bases de datos clínicas. La tesis se centra en la resolución del problema inverso para la reconstrucción no invasiva de la actividad eléctrica del miocardio para diferentes enfermedades cardiacas con diferentes patrones de propagación, implementando un novedoso sistema para patrones de propagación complejos. Además, se han validado los resultados obtenidos y se han clasificado los diferentes patrones de propagación con la estrategia de resolución del problema inverso óptima que minimice el error y aumente la estabilidad del sistema, demostrando sus ventajas y desventajas dependiendo de las diferentes enfermedades cardiacas y su patrón de activación.

Un nuevo método iterativo fue implementado para la resolución del problema inverso para fuentes dipolares, siendo óptimo para representar patrones de propagación simples, logrando una alta estabilidad e inmunidad al ruido al restringir la solución a un número limitado de dipolos. Sin embargo, los patrones de

propagación que no pueden ser representados por un número limitado de dipolos deben calcularse mediante la resolución del problema inverso en términos de potenciales epicárdicos, proporcionando una estimación más detallada de la actividad del miocardio. La resolución del problema inverso en el dominio de la tensión y fase mostró ser muy preciso para patrones de propagación simples y organizados. Este método permite el diagnóstico no invasivo del síndrome de Brugada o la ubicación de focos ectópicos en arritmias auriculares mediante un análisis paramétrico de la morfología de los electrogramas o la reconstrucción de los mapas de activación. Sin embargo, los resultados matemáticos y clínicos presentados en esta tesis demostraron que, para patrones de propagación complejos como la fibrilación auricular (FA), los resultados obtenidos mediante la resolución del problema inverso en el dominio de la tensión y fase son demasiado suaves y optimistas, simplificando enormemente la complejidad de la FA, llevando a resultados no fisiológicos que no coinciden con la actividad compleja de los electrogramas intracardiacos registrados en pacientes con FA. En esta tesis, se ha propuesto una novedosa técnica para la identificación y localización no invasiva de fuentes con una frecuencia dominante alta, basado en la suposición de que en muchos casos las fuentes eléctricas que generan y mantienen la FA presentan una tasa de activación más alta, con una propagación intermitente hacia el resto del tejido auricular cuya frecuencia de activación es más lenta. Aunque las soluciones en el dominio de la tensión y fase para patrones de propagación complejos fueron más suaves y menos precisas, la estimación no invasiva de los mapas de frecuencia fue significativamente más precisa, permitiendo la identificación del gradiente de frecuencia y ubicación de las fuentes de FA de alta frecuencia. Esta técnica puede ser de gran ayuda en la planificación de los procedimientos de ablación, evitando punciones interseptales innecesarias para casos con un gradiente de frecuencia de derecha a izquierda y facilitando la localización de las fuentes de alta frecuencia responsables de la FA, reduciendo el riesgo y la duración de la intervención.

Resum

El comportament del cor es regeix per corrents elèctrics generades en el miocardi i, per tant, l'estudi de la seua activitat elèctrica és essencial per al diagnòstic de malalties cardíaques. Els corrents elèctriques en el miocardi generen un camp elèctric que es propaga a través dels teixits conductors del cos assolint la superfície del tors i, per tant, el registre de la distribució dels potencials de superfície proporciona informació sobre el comportament elèctric del miocardi. La tècnica del mapeig de potencials de superfície permet el registre multicanal en la superfície del tors, proporcionant informació completa de l'activitat elèctrica cardíaca, observant esdeveniments indetectables mitjançant tècniques convencionals.

La relació matemàtica entre l'activitat elèctrica del miocardi i els camps registrats a la superfície del tors es poden obtenir mitjançant la resolució del problema directe o invers de l'electrocardiografia. El problema directe de l'electrocardiografia implica el càlcul dels potencials del tors a partir de l'activitat elèctrica del cor i el model 3D del cos, mentre que la resolució del problema invers permet la reconstrucció no invasiva de l'activitat elèctrica del cor a partir de els potencials de superfície. La resolució del problema invers de l'electrocardiografia té una gran importància en la pràctica clínica atès que fa possible una estimació de l'activitat elèctrica del miocardi únicament a partir de registres no invasius. No obstant això, la resolució del problema invers segueix sent un gran desafiament per a la electrocardiografia ja que està mal plantejat, és molt inestable i té múltiples solucions.

Al llarg d'aquesta tesi s'han desenvolupat diferents estratègies basades en la resolució del problema invers, aplicant-les en el diagnòstic no invasiu d'arítmies ventriculars i auriculars, verificant mitjançant models cel·lulars matemàtics i bases de dades clíniques. La tesi se centra en la resolució del problema invers per a la reconstrucció no invasiva de l'activitat elèctrica del miocardi per a diferents malalties cardíaques amb diferents patrons de propagació, implementant un nou sistema per a patrons de propagació complexos. A més se han validat els resultats obtinguts i se han classificat els diferents patrons de propagació amb l'estratègia de resolució del problema invers òptima que minimitze l'error i augmente l'estabilitat del sistema, demostrant els seus avantatges i inconvenients depenent de les diferents malalties cardíaques i el seu patró d'activació.

Un nou mètode iteratiu va ser implementat per a la resolució del problema invers per fonts dipolars, sent òptim per representar patrons de propagació simples, aconseguint una alta estabilitat i immunitat al soroll en restringir la solució a un nombre limitat de dipols. No obstant això, els patrons de propagació que no poden ser representats per un nombre limitat de dipols s'han de calcular mitjançant la resolució del problema invers en termes de potencials epicàrdics, proporcionant una estimació més detallada de l'activitat del miocardi. La resolució del problema invers

en el domini de la tensió i fase va mostrar ser molt precís per a patrons de propagació simples i organitzats. Aquest mètode permet el diagnòstic no invasiu de la síndrome de Brugada o la ubicació de focus ectòpics en arítmies auriculars mitjançant una anàlisi paramètric de la morfologia dels electrogrames o la reconstrucció dels mapes d'activació. No obstant això, els resultats matemàtics i clínics presentats en aquesta tesi van demostrar que, per patrons de propagació complexos com la fibril·lació auricular (FA), els resultats obtinguts mitjançant la resolució del problema invers en el domini de la tensió i fase són massa suaus i optimistes, simplificant enormement la complexitat de la FA, obtenint resultats no fisiològics que no coincideixen amb l'activitat complexa dels electrogrames intracardiacos registrats en pacients amb FA. En aquesta tesi, s'ha proposat una nova tècnica per a la identificació i localització no invasiva de fonts amb una freqüència dominant alta, basat en la suposició que en molts casos les fonts elèctriques que generen i mantenen la FA presenten una taxa d'activació més alta, amb una propagació intermitent cap a la resta del teixit auricular on la freqüència d'activació és més lenta. Encara que, les solucions en el domini de la tensió i fase per patrons de propagació complexos van ser més suaus i menys precises, l'estimació no invasiva dels mapes de freqüència va ser significativament més precisa, permetent la identificació del gradient de freqüència i ubicació de les fonts de FA d'alta freqüència. Aquesta tècnica pot ser de gran ajuda en la planificació dels procediments d'ablació, evitant puncions interseptales innecessaris per a casos amb un gradient de freqüència de dreta a esquerra i facilitant la localització de les fonts d'alta freqüència responsables de la FA, reduint el risc i temps de la intervenció.

1. Introduction

1.1. Motivation

The electrical activity of the heart plays a very important role in its behavior and, therefore, this behavior can be defined and analyzed from the study of the electrical activity in the myocardium. The study of the cardiac electrical activity is essential for diagnosing the different diseases related to abnormal electrophysiological function of the heart. The technology in the medical field is advancing quickly by developing new therapeutic techniques and, specifically, improving techniques for the diagnosis and treatment of the electrical diseases of the heart.

The most common technique in clinical use for recording the electrical activity of the heart is the 12-lead ECG, which allows inferring the general electrical activity of the heart, like the cardiac rhythm or the propagation direction of the main wavefronts. However, this technique obviates a lot of electrical information available on the torso and, consequently, many electrical events of the heart remain undetectable.

Nowadays, it is possible to obtain a greater number of electrical signals by recording non-invasively the electrical activity on the surface of the torso with the "Body Surface Potential Mapping" (BSPM) technique, which allows for a more complete knowledge of the cardiac activity by observing events undetectable by the clinical 12-lead electrocardiogram. However, although this technique implies recording a large amount of information of the electrical knowledge on the torso, it does not record the electrical activity on the myocardium.

The exact knowledge of the electrical activity in the myocardium, which allows the accurate identification and localization of the sources of the arrhythmias, has a great importance in the diagnosis and treatment of many diseases. Currently, the knowledge of the specific electrical activity of the myocardium is known by invasive procedures such as catheterization, with its intrinsic risk, economic cost and time. At this point the main question is: Is there any way to know the specific electrical activity in the myocardium by using noninvasive methods?

This question is an important challenge of the current electrophysiological research, becoming one of the most significant researching lines in this domain. The resolution of this problem, called the inverse problem of electrocardiography, allows the noninvasive reconstruction of the electrical activity of the heart by using numerical methods in conjunction with the electrical activity on the torso recorded with the BSPM technique and the 3D torso model of the patient, build by the computed tomography or magnetic resonance image segmentation. However, inverse problem resolution is still a big challenge in electrocardiography since it is ill-posed, very unstable and has multiple solutions. In this thesis different algorithms

and strategies for the noninvasive reconstruction and source location of the myocardial activity were implemented and validated, comparing and classifying different atrial and ventricular propagation pattern and diseases with the optimal resolution strategy of the inverse problem that minimizes the error and increases the stability of the system, even under high noise conditions or for complex propagation patterns.

1.2. Objectives

The inverse problem is of great importance in clinical applications since it allows estimating the electrical activity of the myocardium by only using noninvasive recordings. However, the inverse problem is still a big challenge in electrocardiography since no method has proved to have a high accuracy independently of the propagation pattern, often achieving over smoothed and inaccurate results, especially for complex propagation patterns. The main objectives of the thesis can be established as:

- To develop and validate different algorithms and strategies for solving the inverse problem of electrocardiography for different source models and domains. The algorithms will be applied in the noninvasive diagnosis of ventricular and atrial arrhythmias and evaluated with mathematical cellular models and clinical data bases.

- To propose different strategies for the inverse problem resolution to minimize the error and increase the stability of the system for different propagation patterns. The advantages and disadvantages of the implemented methods will be also determined in function of the different diseases and their activation pattern.

- To develop and validate a novel technique for the accurate noninvasive identification and location of highest dominant frequency sources for complex propagation patterns commonly present during atrial fibrillation (AF). The novel method will be compared with conventional methods based on the voltage and phase domain resolutions, by validating the results with AF mathematical models and patient data.

1.3. Structure of the thesis

Chapter 2. State of the art. In this chapter, the background and main concepts necessary to understand and appreciate this thesis are described. Cardiac electrophysiological concepts are presented, followed by the different noninvasive techniques used to measure electrical activity of the heart, including the standard electrocardiogram and the body surface potential mapping (BSPM). This work validates and applies the developed algorithms in ventricular and atrial diseases. The pathophysiology and current clinical treatments of the atrial fibrillation and Brugada syndrome diseases are also summarized in this chapter. Moreover, main concepts, current background and mathematical formulation of the forward and inverse problems of electrocardiography are detailed.

Chapter 3. Methods. In this section we exposed the methodology describing the numerical methods and approximations followed for the transfer matrix construction and inverse problem resolution used in the development of the work of this thesis. Mathematical cellular models computation, employed for the algorithm validation was also summarized in this chapter.

Chapter 4. An Iterative Method for Indirectly Solving the Inverse Problem of Electrocardiography. An iterative method for solving the inverse problem in terms of dipoles is presented, reconstructing a dipolar representation of the myocardial activity by finding the optimal dipole linear combination whose forward computed surface potentials best match the surface potentials recorded from a patient. A parametric study was performed to assess the accuracy of the method depending on the system resolution, noise or number of dipoles.

Chapter 5. Characteristics of inverse-computed epicardial electrograms of Brugada syndrome patients. In this study, in order to non-invasively identify Brugada syndrome patients independently of their phenotype, we evaluated morphological indicators from the inverse computed electrograms of 6 patients with diagnosed Brugada syndrome and 6 controls, analysing and comparing the duration, activation time and morphology.

Chapter 6. Noninvasive estimation of the activation sequence in the atria during sinus rhythm and atrial tachyarrhythmia. In this chapter, BSPM and intracardiac electrograms were recorded simultaneously in one patient with paroxysmal AF. Then, inverse problem was solved for reconstructing the atrial activation sequence during normal sinus rhythm and during left superior pulmonary vein pacing, locating non-invasively the pacing site.

Chapter 7. Noninvasive Estimation of Epicardial Dominant High-Frequency Regions during Atrial Fibrillation. In this section, a novel method for noninvasive identifying and locating the high frequency AF sources is proposed. Inverse problem was solved in the voltage, phase and frequency domain for AF complex propagation patterns. This study compared the accuracy and evaluated the feasibility of the inverse reconstruction in the different domains, validating the results with two AF patients and a mathematical model data base. This work proved that inverse problem resolution in the phase or voltage domains for AF complex propagation patterns is not feasible, achieving over simplistic results that do not correspond to the reality. However, AF high frequency driver location was accurately located, even under noise conditions.

Chapter 8. Discussion. In this chapter, the work implemented in this thesis is discussed in detail, summarizing the developed work, comparing it with the literature and commenting its limitations.

Chapter 9. Conclusions and Future work lines. Finally, conclusions are exposed and, in order to complete the work developed in this thesis and overcome their limitations, guidelines for future work is provided.

Chapter 10. Contributions. In this section, the main publications and contributions related to the thesis are listed. Research stays performed during this thesis and their purpose are also listed and explained.

2. State of the art

In this chapter, the background and main concepts necessary to understand and appreciate this work are described. First, the heart, the main character of this thesis, is described; followed by its electrophysiology and the different noninvasive techniques used to measure its electrical activity, including the standard electrocardiogram and body surface potential mapping (BSPM). These techniques are often used to diagnose several ventricular or atrial diseases due to an abnormal electrical behavior; such as atrial or ventricular arrhythmias caused by ectopic foci, genetic diseases that could lead to a sudden death such as Brugada syndrome or one of the most common diseases in patients over 60 years old, the atrial fibrillation. These diseases and their pathophysiology are also explained in this chapter. This thesis proposes a technique to non-invasively reconstruct the electrical activity of the heart by solving the inverse problem of electrocardiography, localizing noninvasively the sources of the arrhythmias and avoiding invasive techniques like catheterisms or drug administrations. The main concepts and the mathematical formulation of the forward and inverse problems of electrocardiography are explained.

2.1. The heart

2.1.1. Anatomy of the heart

The heart is a muscular viscera located in the center of the thoracic cavity. Its main function is to pump blood throughout the body by rhythmic contractions allowing a continuous flow of blood. The heart is composed by four cavities connected two by two, divided by a central wall, or septum, into left and right cavities (see Figure 2.1).

Each half consists of an atrium, which receives blood returning to the heart from the blood vessels, and a ventricle which pumps blood out into cavities. The left side of the heart receives oxygenated blood from the lungs and pumps it to tissues throughout the body. The right side of the heart receives blood from tissues and sends it to the lungs for oxygenation. Although the blood flow in the left and right sides of the heart is separated, the two sides of the heart contract in a coordinated way: first both atria contract together, then the ventricle contracts. In order to avoid the backflow of blood of the cardiac pump, the heart has four valves separating the two atria from the ventricles and two valves at the beginning of the arteries, separating the ventricles from the rest of the circulatory system of the body. The tricuspid valve is located between the right atrium and right ventricle and the mitral valve between the left atrium and ventricle. The pulmonary valve is located between

the right ventricle and the pulmonary artery and the aortic valve is located in the outflow tract of the left ventricle [Malmivuo 1995].

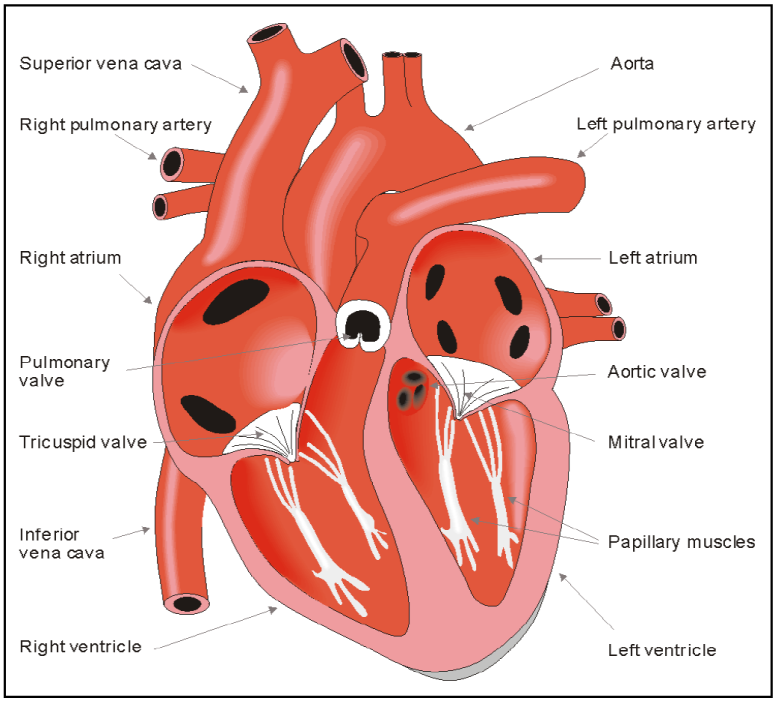

Figure 2.1: Anatomy of the heart [Malmivuo 1995].

2.1.2. Electrophysiology of the heart

The heart contracts synchronously allowing an optimal blood pumping. The protagonist of this synchronized contraction of the regions of the heart is the action potential (AP) and its propagation through various structures of the heart.

The AP is generated by the flux of positive and negative charged ions across the specific channels in the membrane of the myocardial cells (see Figure 2.2). At rest, the cell is polarized and the resting transmembrane potential difference remains constant around -80mV. When one cardiac cell, called cardiomyocyte, is stimulated above a threshold potential, certain ionic channels react by changing their permeability, causing a flow of ions and the consequent transient increase of the intracellular potential, called cellular depolarization. Once a cell is depolarized, it can trigger neighboring cells and cause them to depolarize and contract as well. This phenomenon produces a moving wavefront of varying electric potential, which is called activation wavefront. As a result of this depolarization, the calcium concentration inside the cell increases, which causes the contraction of the cell and

the consequent contraction of the whole heart and the blood pumping. After an electrical activation the cell cannot be stimulated again for a time interval, called refractory period, ensuring a minimum time interval between two consecutive contractions.

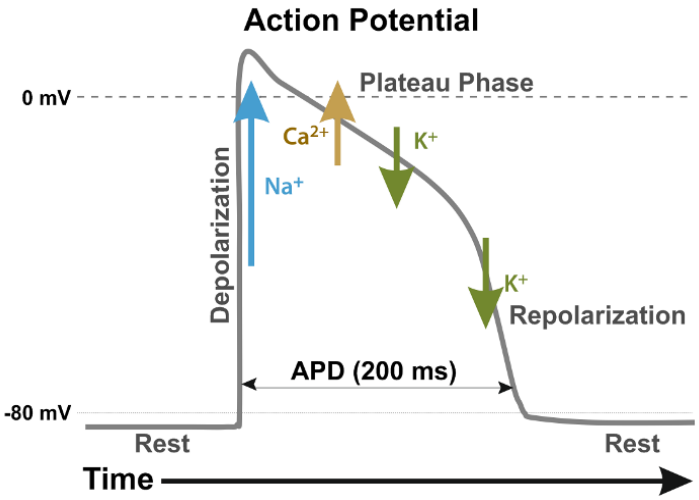

Figure 2.2: Cardiac action potential and ionic flows through the cell membrane [Malmivuo 1995].

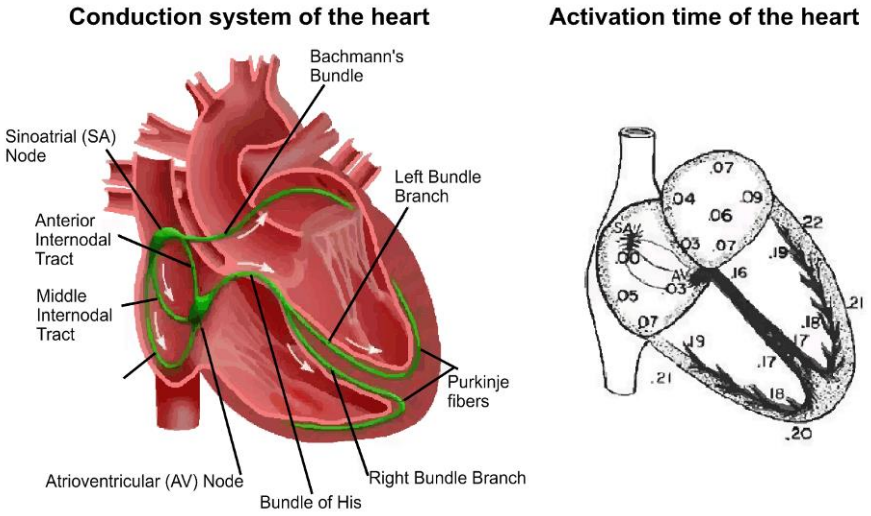

Figure 2.3: Action potential propagation in the heart [Malmivuo 1995] *Left*: Conduction system of the heart. *Right*: Activation time of the heart in seconds.

The initiation of the myocardial stimulus and the structures involved in the propagation of the AP and the effect produced in the cardiac contraction are explained below (see Figure 2.3). The electrical activity begins in the sinoatrial node, also known as the natural pacemaker of the heart, a small mass of specialized cells located in the wall of the right atrium near the entrance of the superior vena cava. These cells have the ability to spontaneously depolarize and generate an action potential on their own. Electrical impulses spread through the intermodal tracts that connect the sinoatrial node to the atrioventricular node (0.02-0.05 m/s), a group of auto-rhythmic cells near the floor of the right atrium, which is the only connection between the atria and the ventricles, delaying the propagation of the impulse to the ventricle. Then the electrical impulse reaches the Bundle of His, which bifurcates into the left and right bundle branches, where the electrical impulses rapidly spreads through the Purkinje (3-3.5 m/s) fibers to the muscle of the right and left ventricles, causing their simultaneous contraction.

2.1.3. The electrocardiogram

The electrocardiogram (ECG) is the simplest noninvasive method for recording the electrical activity of the heart. The ECG was measured for the first time in 1887 by Augustus D. Waller with a mercury capillary electrometer, exhibiting only 2 distorted deflections [Waller 1887]. In 1895 Willem Einthoven described the 5 basic P, Q, R, S, T ECG waves [Einthoven 1895] depicted in Figure 2.4, and in 1903 Einthoven improved the ECG recordings with the introduction of a string galvanometer [Einthoven 1903, Einthoven 1908].

The ECG represents electrical activity of the whole heart, describing the summation of all AP generated by all the myocytes of the heart, as depicted in Figure 2.5. The electrical activity of a group of cells which are simultaneously depolarizing can be represented as an equivalent current dipole source with an associated vector, with three variable parameters: location, magnitude and orientation. Experimental studies in humans proved that 95% of the myocardial electrical activity of a healthy heart can be modelled with a single moving dipole [Frank 1955], called the equivalent dipole model. According to this model, the ECG can be interpreted as the projection of the dipole vector on an equilateral triangle formed by the standard leads I, II and III [Einthoven 1912]. The electrical activity of the heart can be measured indirectly on the surface of the torso by recording an ECG, as depicted in Figure 2.4.

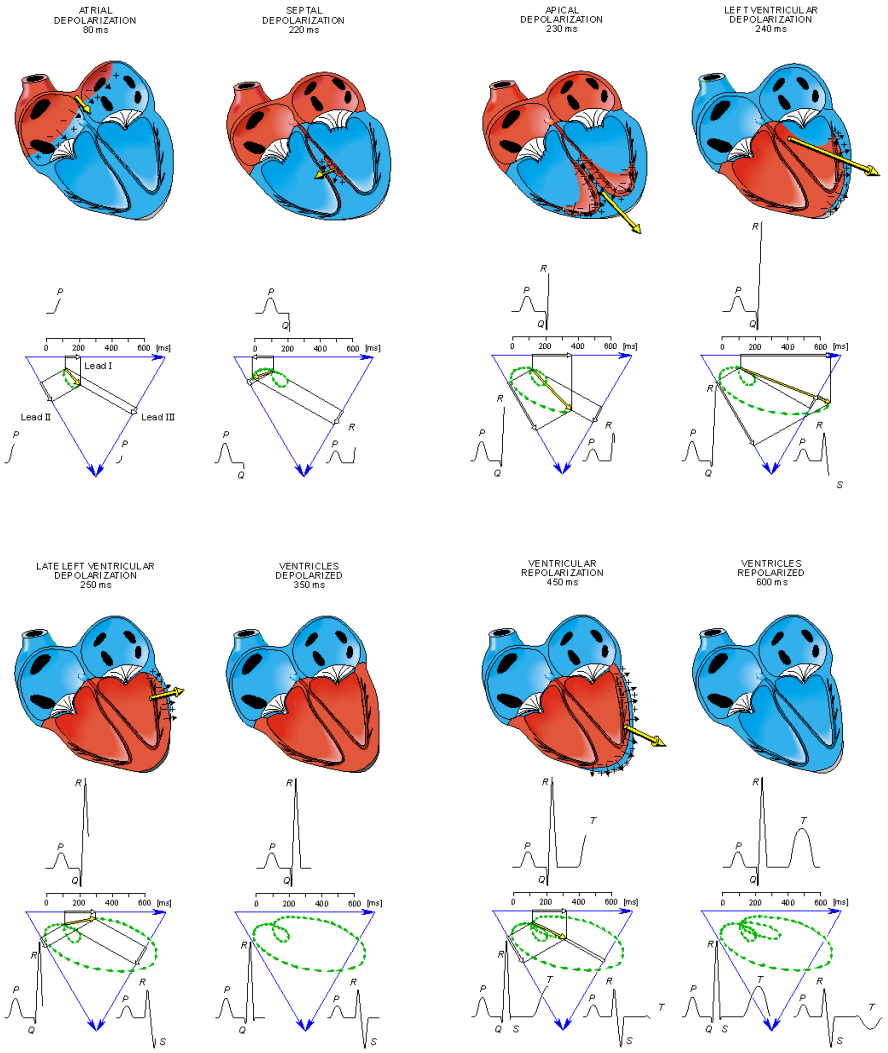

Figure 2.4: ECG generation with the 3 standard derivations and the representation of the equivalent dipole [Malmivuo 1995]

An ECG tracing shows several deflections or waves that reflect the electrical activity of heart chambers. The so-called P wave corresponds to the depolarization of the atria. After the P wave, the QRS complex reflects the ventricular depolarization, whereas the T wave corresponds to the ventricular repolarization or return to the resting state (see Figure 2.5) [Malmivuo 1995].

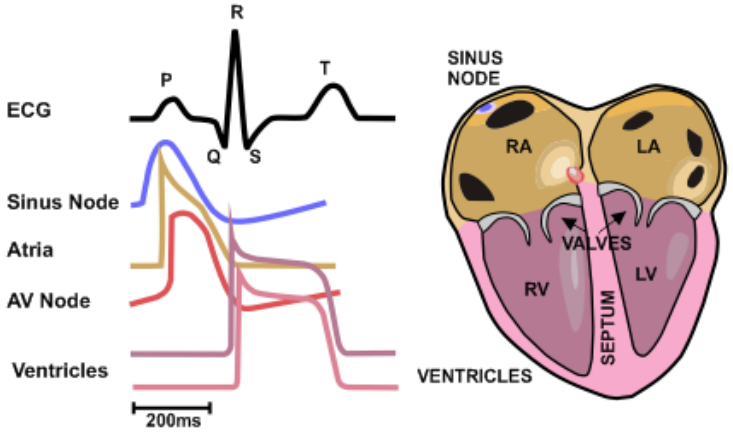

Figure 2.5: Action potentials in the electric conduction system and ECG generation during sinus rhythm (modified from [Malmivuo 1995]).

The ECG can be measured at different points of the body resulting in different leads. In clinical practice *12 standard leads* are used: *three standard leads*, *three augmented leads* and *six precordial leads*:

The three *standard bipolar leads*, used by Einthoven, are recorded from the three limbs (right arm, left arm and left leg), obtaining the other leads as a linear combination of two of the three limbs. The positive terminal is connected to one limb and the negative to the other one. With this configuration an equilateral triangle is formed by the three limbs, on whose vertices the vector corresponding to the electric field generated by the heart is projected, obtaining the electrical activity of the heart, as depicted in Figure 2.6 [Malmivuo 1995, Cooksey 1977].

The *three augmented leads* use the three limbs, as in the previous configuration, however, as we can see in Figure 2.6, the reference point is considered at zero potential, recording the unipolar potential at each of the three leads. The positive terminal is connected to one limb while the negative is connected to the midpoint between the other two.

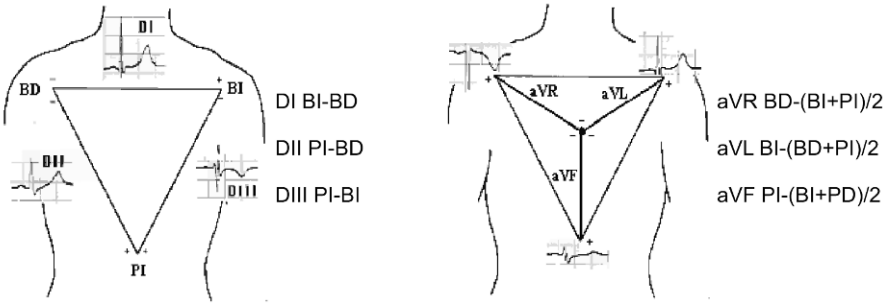

Figure 2.6: ECG-leads. *Left*: Standard leads. *Right*: Augmented leads.

The *six precordial leads* (Figure 2.7) are unipolar leads located on the hemothorax [Malmivuo 1995]. In this case, the electrical reference is the Wilson Central Terminal, obtained from the average of the potentials of the three limbs. It has been shown that, although the standard and augmented leads contain the electrical activity of the heart as a whole, the precordial leads add relevant information [Wilson 1944], being the most used in clinical practice.

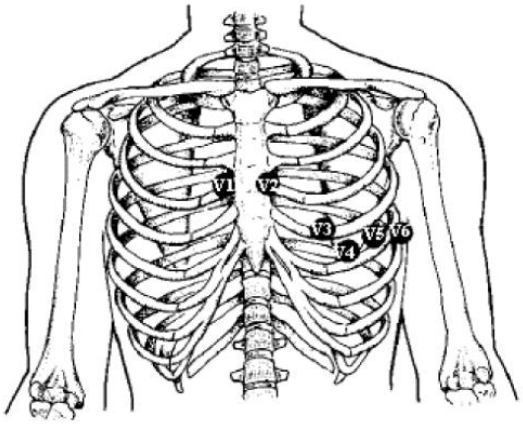

Figure 2.7: The 6 precordial leads

2.1.4. Body Surface Potential Mapping

Body Surface potential Mapping (BSPM) is a technique which allows the construction of potential maps of the torso surface in order to obtain more information of the electrical activity than with conventional techniques like the electrocardiogram. Thereby, it is possible to determine as much as possible the electrophysiology and clinical condition of the heart from surface potential measurements.

For years it was believed that the 12-lead electrocardiogram included all the diagnostic information from the body surface and that the use of a larger number of recording sites would bring only redundant data, deductible from other known points. However, subsequent studies showed that maps obtained by the BSPM technique allow a better detection of heart diseases, since several phenomena are unnoticed with the standard 12-leads technique [Carley 2003, Finlay 2005, Hoekema R 1999, O'Neil 2010, Mitchell 1992, Gardner 1986, De Ambroggi 1986, Urie 1978]. With the BSPM technique, a greater number of electrodes is used (between 32 and 256 electrodes) to record the electrocardiographic information at different points of the torso. There is no agreement on their number or position of electrodes, each research group uses its own configuration, however, their location has to be precisely known to correctly use their information.

As commented before, Frank et al. [Frank 1954] affirmed that approximately 95 % of the QRS complex can be modeled as an equivalent single dipole with a fixed localization, and then, a conventional ECG may account for all relevant information. However, Taccardi et al. [Taccardi 1963] demonstrated that for long ventricular depolarization and for pathological cases, the potential distributions on the torso showed multiple local maxima and minima (see Figure 2.8) and, therefore, for a correct modeling of the electrical activity it was necessary to use 2 or 3 dipoles. This theory can specially be applied to Brugada syndrome [Guillem 2010], since the ventricular electrical activity cannot be modeled with a single dipole. Other diseases like atrial fibrillation in which there are multiple simultaneous propagating waveronts require multiple dipoles for an accurate modeling of these propagation patterns.

Many other studies reported the improvement of the cardiac diagnosis with the BSPM against the conventional systems, which cannot record some of the electrical events, cause of many cardiac diseases. In the field of ventricular arrhythmias, Bruns et al. [Bruns 2002] studied the ST segment in BSPM recordings, proving that upper right precordial leads are great of importance for detecting ECG markers of Brugada syndrome, as depicted in Figure 2.9. On the other hand, Eckardt et al. [Eckardt 2002] showed that the presence of late potentials and ST segment elevation on BSPM recordings is a significant factor for predicting ventricular arrhythmias in Brugada syndrome patients. For the diagnosis of atrial arrhythmias, SippensGroenewegen et al. [SippensGroenewegen 1998] studied BSPM maps in order to identify the origin of focal tachycardias or the reentrant circuit during atrial flutter [SippensGroenewegen 2000]. Guillem et al. demonstrated that the wavefront propagation maps technique can be used to summarize the electrical propagation pattern into a single map during atrial flutter [Guillem 2009_a] and characterize the organization degree during atrial fibrillation [Guillem 2009_b]. Guillem et al. also reported that BSPM allows identifying the activation frequency gradient in patients with atrial fibrillation by computing the power spectral density of BSPM recordings [Guillem 2013].

Another additional advantage of BSPM is to provide an alternative method for displaying data that can be played as a video of a sequence of potential maps allowing spatial and temporal information visualization, providing regional information which allows an estimation of the location in the myocardium of one particular event; unlike the standard ECG that only allows to record signals from a limited region of the heart and may underrepresent the contributions of other regions of the heart.

BSPM noninvasive recordings, in conjunction with the 3D model of the torso and its different volume conductors, obtained by the computed tomography or magnetic resonance images segmentation, are the main inputs used to solve the inverse problem of electrocardiography.

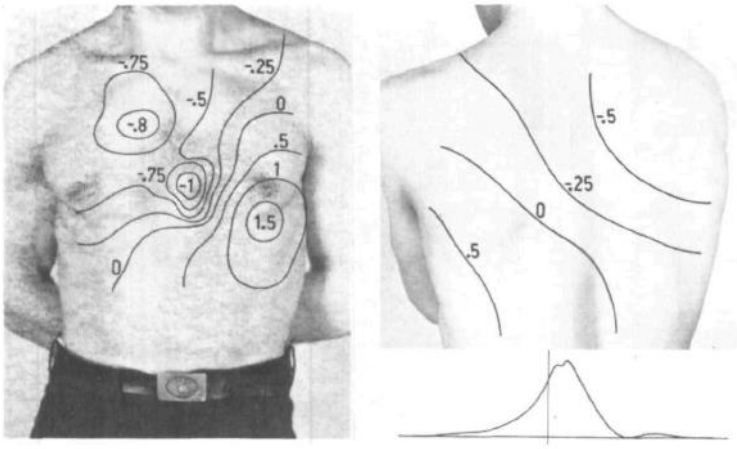

Figure 2.8: Isopotential maps of the thoracic surface of a healthy subject showing the existence of two simultaneous potential minima [Taccardi 1963].

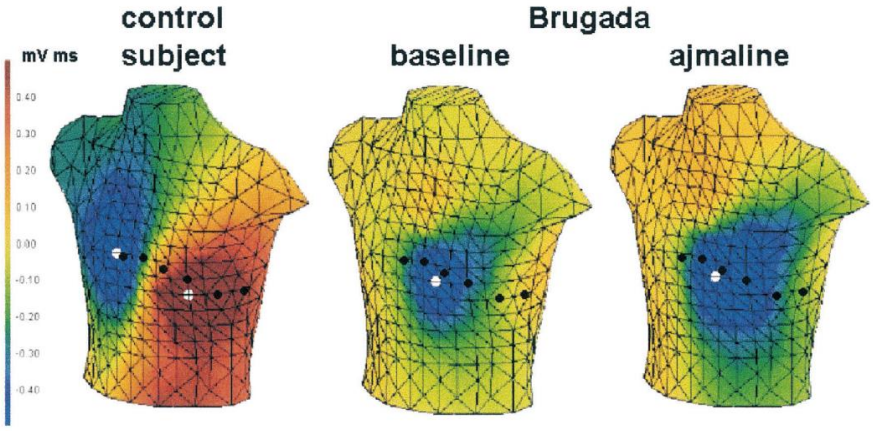

Figure 2.9: Noninvasive contruction of torso surface potential maps from a control subject and Brugada syndrome patient [Bruns 2002]. The black dots indicate the position of the standard leads V1-V6.

2.2. Heart Arrhythmias: Electrophysiology and treatment

2.2.1. Introduction

As we have previously discussed, the mechanical activity of the heart is synchronized by its electrical activity. When the electrical activation of the heart does not follow a natural spontaneous activation of the sinus node (the so-called sinus rhythm), the heart rhythm is referred as a cardiac arrhythmia. Cardiac arrhythmias can be classified as supraventricular arrhythmias, when they involve heart structures above the atrio-ventricular node or as ventricular arrhythmias, when they mainly involve the ventricles. While supraventricular arrhythmias mainly decrease the quality of life of patients, ventricular arrhythmias are lethal. There are several mechanisms that are involved in the development of cardiac arrhythmias. The most frequent cause for the development of arrhythmias is the modification of the myocardial substrate as a consequence of a prolonged ischemia, or lack of oxygen that may result in necrosis of myocardial cells. This modified substrate favors the electrical impulse to reenter and if this reentry perpetuates it leads to an arrhythmia. Modification of the myocardial substrate can also be a consequence of aging and development of fibrosis, which can be favored by genetic factors. Finally, mutations of cardiac channels can also cause a modification of cardiac action potentials that may lead to an increased susceptibility to cardiac arrhythmias. We will introduce some cardiac arrhythmias whose diagnosis can be improved by applying signal processing to cardiac electrical signals.

2.2.2. Atrial arrhythmias: Atrial fibrillation

Most atrial arrhythmias are caused by a macro or micro-reentry of the electrical wavefront in the atria. *Atrial flutter (AFL)* is caused by a macroreentry around an anatomical obstacle in the atria. Typically, this anatomical structure is a heart valve, most commonly the tricuspid valve, which is referred as typical atrial flutter [Olgin 1995]. This electrical behavior in the right atrium is reflected on the ECG by a continuous “sawtooth” pattern between QRST complexes that replaces the P wave which is present during sinus rhythm (see Figure 2.10).

Atrial fibrillation (AF) is the most common supraventricular arrhythmia and is characterized by a chaotic electrical activation of the atria, causing an inefficient blood pumping to the ventricles and increasing the risk of embolism due to blood statis. In contrast to the sinus rhythm, during AF the P wave is absent and substituted by low amplitude and irregular atrial waves (Figure 2.10).

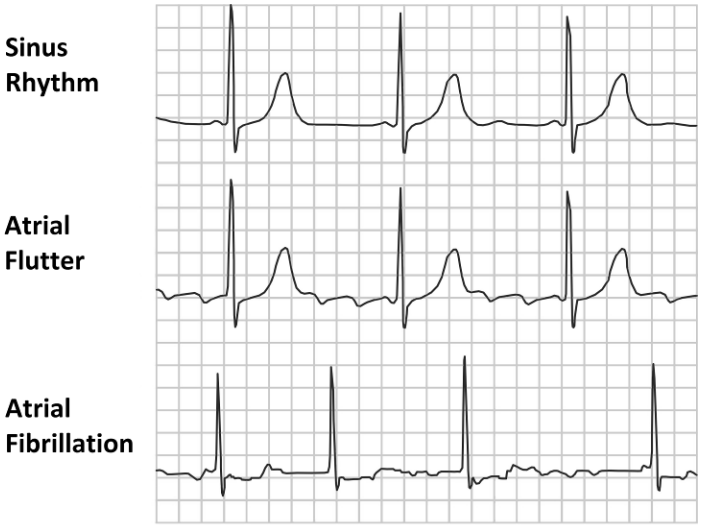

Figure 2.10: Sinus rhythm, atrial flutter and atrial fibrillation wave morphologies.

As it was presented before, the normal electrical activity in the heart is governed by the sinoatrial node, generating electrical stimulations allowing a prior contraction of the atria perfectly coordinated with the ventricles, adapting the contraction rhythm of the heart to the body demand with a beat rate of 60 to 200 beats per minute. However, during the AF the different regions of the atria have an apparent chaotic and uncoordinated behavior, achieving activations of 400 to 600 beats per minute, causing an inefficient blood pumping. Fortunately, the atrio-ventricular (AV) node avoids the propagation of all the stimulus waves generated in the atria, allowing only some of the stimuli to reach the ventricles [Nattel 2002]. As a consequence, the ventricular rate does not follow the activation of the sinus node and thus does not adapt to the activity of the patient, being usually too fast during atrial flutter and irregular during atrial fibrillation. Without the filtering function of the AV node, it would result in a high ventricular activation rate with loss of its effective contraction and causing the death of the patient.

2.2.2.1. Mechanisms of atrial fibrillation initiation and maintenance

The mechanisms underlying the initiation and maintenance of AF are not completely understood and there are several theories that partially explain its clinical manifestation. At the beginning of the 20th century, different ideas for explaining the AF initiation and perpetuation grounded the basis for developing the research in this field: multiple reentry propagating wavelets, focal electrical discharges or functional reentrant activity with fibrillatory conduction (Figure 2.11) [Nattel 2002]. The multiple reentry excitation theory affirms that the cause of the atrial irregular

activity is a consequence of primary source, while other theories support the idea that irregularity is due to interactions between high-frequency wavefronts perpetuated by a rapid focal source or single reentrant circuits, favored by a fibrillatory conduction caused by a variation of the refractory characteristics of the atrial tissue [Nattel 2002]

.

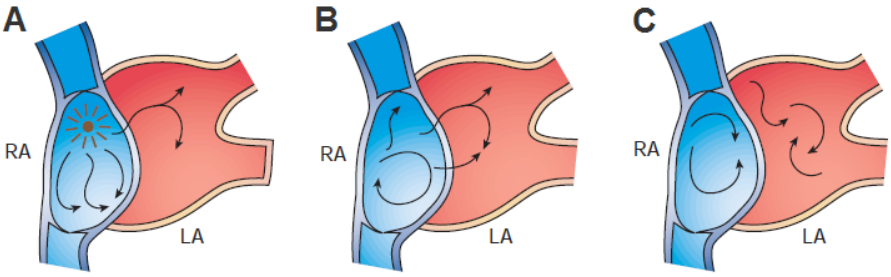

Figure 2.11: Theoretical mechanisms of the atrial fibrillation [Nattel 2002] *(A)* Ectopic foci. *(B)* Single reentrant circuits. *(C)* Multiple reentrant circuits.

Over the last half of the 20th century, it became accepted by the scientific community that AF was a result of a chaotic multiple reentrant wavelet propagation across the atria, which have the ability of perpetuating themselves. This theory was highly supported by the work of Moe et al. [Moe 1959], shelving the theory of the role of ectopic focus and single-circuit in perpetuation of AF.

The work of the group of Allesie has been particularly influential emphasizing the hypothesis of the multiple wavelet reentry. Allessie et al. [Allesie 1977], based on his "leading circle model", affirms that the size of functional re-entry circuits depends on the wavelength (see Figure 2.12), defined as the distance travelled by the electrical impulse in one refractory period. Thereby, the smaller the wavelength is, the smaller the minimum circuit size, increasing the number of circuits that can be accommodated, which in turn favours multiple-circuit reentry as exposed by Moe et al. [Moe 1959], which promotes AF (see Figure 2.12.B). Following this theory, by increasing the refractory period and, consequently also the wavelength, the number of circuit reentries that can be maintained would be limited, thus not allowing AF to sustain itself (see Figure 2.12.C).

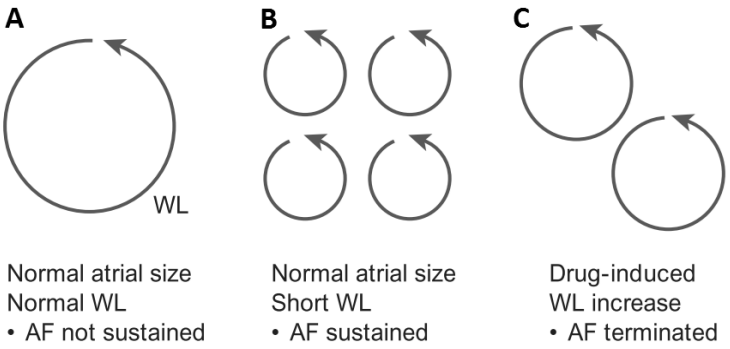

Figure 2.12: Role of wavelength in the stability of atrial fibrillation [Nattel 2002]. The size of functional re-entry circuits depends on the wavelength. Short wavelengths allow several simultaneous circuits to be maintained, favoring perpetuation of atrial fibrillation.

The theories explained by Allesie et al. [Allesie 1977] where supported by Konings et al. with human AF experimentation [Konings 1994]. Related to the multiple circuit reentries and macroreentrant, Konings et al. [Konings 1994] quantified the spatial organization of AF, presenting and quantifying the degree of complexity of different human right atrial (RA) propagation pattern, according to the number of wavelets and conduction blocks, relating the mechanism maintaining the AF for each patient. In order to achieve the study Konings et al. mapped the free wall of the RA by using an electrode containing 244 unipolar leads. Different activation maps were acquired with large interindividual differences and complexities, which were classified in 3 different types (see Figure 2.13), being the Type I the most organized pattern and the Type III the most disorganized. The type I, corresponding to 40 % of the patients, consistent with the theory of a macroreentrancy, consists of single broad wavefronts propagating uniformly. Type II, corresponding to 32 % of the patients, presented activation pattern characterized by single waves associated with a considerable amount of conduction block and/or slow conduction or the presence of two wavelets. Type III, corresponding to 28 % of the patients, is consistent with the multiple reentrant wavelet theory [Moe 1959], presenting an activation pattern highly fragmented with three or more wavelets that changed their direction of propagation due to the numerous arcs of functional conduction block. Konings et al. show that in a same observation area, for AF type I and II, with a larger circuit size, the lower number of wavelets (Figure 2.13), in contrast to AF type III and some of the AF type II that presented small circuit sizes with multiple circuits. These results are consistent with the fact that for a smaller circuit size, the number of reentrant circuits accommodated in a same area increases, favoring the generation of multiple-circuit reentries, and thus perpetuating AF [Allesie 1977].

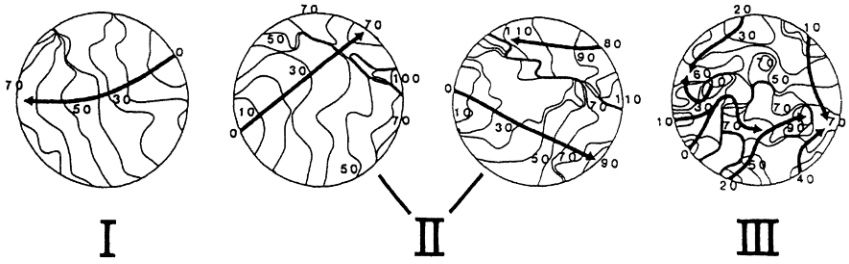

Figure 2.13: Mapping criteria for classification of the complexity of atrial fibrillation [Konings 1994]. Arrows indicate the main direction of propagation.

Allessie et al. [Allessie 2010] continued the work of Konings et al. [Konings 1994] by comparing the spatiotemporal characteristics of the fibrillatory process in patients with normal sinus rhythm and long-standing persistent AF [Allessie 2010], characterizing the substract of AF by in function of (1) the total length of interwave conduction block, (2) the number of fibrillation waves, and (3) the ration of block collision of fibrillation waves (dissociation index). Thereby, Allessie et al. and Groot et al. [Allessie 2010, de Groot 2010] proved that in patients with persistent AF the complexity was significantly much higher than for acute AF (see Figure 2.14) leading to a multiple wave reentry propagation pattern. In patients with persistent AF, the total length of block was more than 6-fold higher than during acute AF and the number of fibrillation waves and the dissociation index were also much larger for persistent AF, showing an AF pattern with similar characteristics to the AF type III presented by Konings.

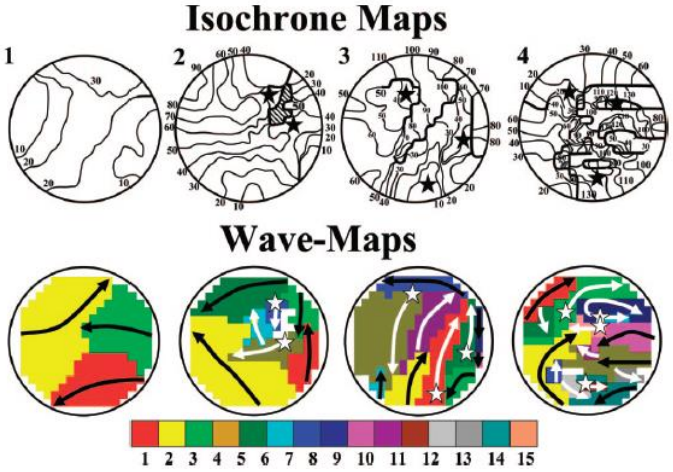

Figure 2.14: Four isochrone maps from the right atria for acute and persistent AF [Allessie 2010]**.** *(1)* and *(2):* Isochrone maps during acute AF. *(3)* and *(4):* Isochrone maps during persistent AF. Thick lines indicate line blocks; asterisks indicate epicardial breakthrough; arrows indicate the main trajectories of the waves.

Although type II and type III present a disorganized electrical activity unexplained by simple propagation pattern theories, 40 % (type I AF) show an organized propagation pattern.

In contrast with the multi reentrant wave propagation, since the 1990s, several mapping studies support the theory of a primary local generator, consisting of either a single small re-entry circuit or an ectopic focus [Mandapati 2000, Haïssaguerre 1998, Mansour 2001].

Single re-entrant circuit maintaining paroxysmal or persistent AF, was supported by experimental studies, affirming that AF depends on the periodic activity of reentries or rotors located in the posterior left atrial (LA) wall-PV region [Jalife 2003]. These rotors activate the atria at an exceedingly high frequency resulting in fibrillatory conduction [Jalife 2003]. The term "rotor" is defined as a stable rotating pattern of reaction and diffusion that surrounds a pivot point, also called "phase singularity" [Winfree 1978]. From a rotor radiates a spiral wavefront to the surrounding tissue. Skanes et al. [Skanes 1998] proved in Langendorff-perfused sheep hearts recorded by optical mapping that AF was caused by sources with spatiotemporally periodic activity, reflected as stationary rotors located on the anterior wall of the LA (Figure 2.15). Despite the uniform activation in LA (Figure 2.15.A and Figure 2.15.B), the electrical activity in the RA was highly heterogeneous (see Figure 2.15.C and Figure 2.15.D). Skanes et al. obtained that the cycle length of spatiotemporal periodic waves correlated with the dominant frequency of their respective optical pseudo-EGMs, especially in the LA, supporting that organized electrograms (EGMs) are caused by a uniform activation and are indicative of the presence of a stationary rotor. In specific examples, sources of periodic activity were seen as rotors or more commonly as periodic breakthroughs. However, in most cases, periodic waves were seen to enter the mapping area from the edge of the field of view [Skanes 1998].

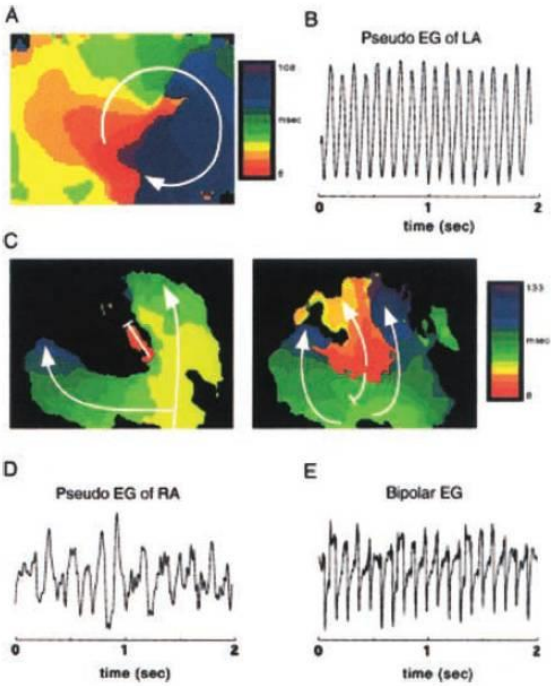

Figure 2.15: Isochrone maps and pseudo-EGMs constructed from LA and RA optical recordings of episode of AF [Skanes 1998]**.** *(A)* Isochrone map of single rotation of stable rotor located in LA. *(B)* Pseudo-EGM of this signal, which is monomorphic. *(C)* two sequential RA isochrone maps during AF. *(D)* RA pseudo-EGM. *(E)* Bipolar EGM, consistent with AF.

Supporting the theory that AF is initiated by an ectopic focus, Haïssaguerre et al. observed that the pulmonary veins in the left atrium seem to have a highly significant role in the initiation and perpetuation of AF [Haïssaguerre 1998, Kumagai 2000, Sueda 2001], being the most common location of the primary local generator, initiating as a rapid atrial tachycardia from the pulmonary veins ectopic foci, leading to a multi circuit reentry myocardial activation.

The hypothesis that a rapid atrial tachycardia as a primary source in the pulmonary veins in the left atrium, caused by either ectopic beats or functional reentries, lead to new working lines for the AF source location by the frequency analysis of the AF signals [Mansour 2001, Atienza 2006]. Mansour et al. affirm that the complexity of the electrical activity from AF sources with a higher activation rate located in the LA, increases while it propagates intermittently to the RA, resulting in left-to-right frequency gradients [Mansour 2001] (see Figure 2.16). The theory of an intermittent blockage of the wave propagation will be the basis of some ablation procedures currently used in the clinical practice, as explained in the following section.

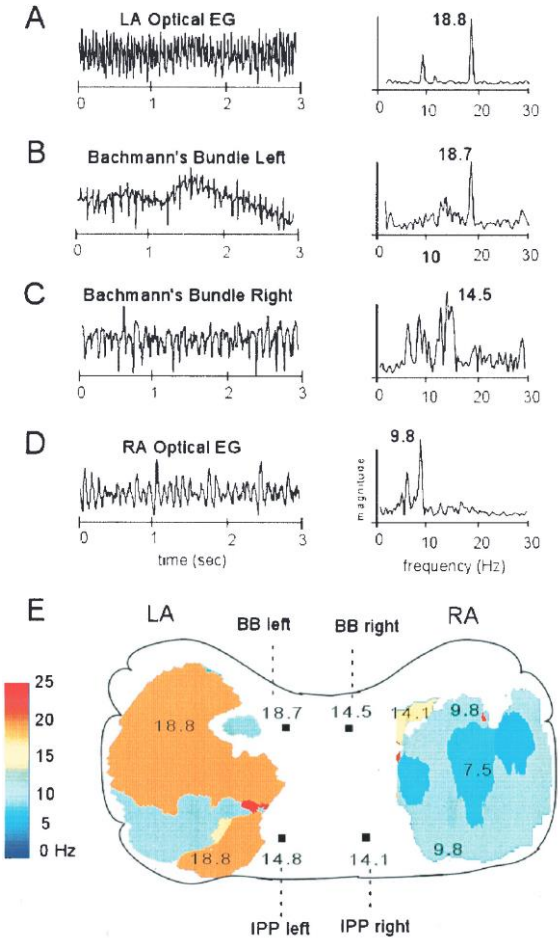

Figure 2.16: Left to right frequency gradient [Mansour 2001]. *(A)* Optical electrogram and power spectrum from the left atrium (LA). *(B, C)* True EGMs and power spectrum from left and right Bachmann's bundle (BB). (*D)* Right atrial (RA) optical EGM and power spectrum. (*E)* Dominant frequency map of RA and LA, including BB and inferoposterior pathway (IPP).

2.2.2.2. Atrial fibrillation clinical treatment

AF has been traditionally treated with antiarrhythmic drugs that control the rhythm by modifying the cardiac electrical properties, avoiding reentries by increasing the cellular refractory period. However, the treatment with drugs have important secondary effects, since it doesn't affect specifically the atria but also the ventricular electrical activity thus increasing the mortality rates [Nattel 2002, Nattel 1998]. Electrical cardioversion is another therapy used to terminate AF by applying

controlled electrical impulses, which synchronize the electrical activity of the atria. However, this technique does not eliminate the cause of AF and thus there may be recurrences after a short period of time.

The ablation therapy is able to cause a controlled damage in the myocardial region causing the arrhythmia and, therefore, eliminates the source of the AF [Nattel 2002, Fuster 2006]. Consequently, the identification and location of this source is an essential goal to achieve before the ablation of this source. While pulmonary veins (PVs) are the most frequent source location due to their especial electrophysiological properties [Jais 2002, Shah 2003], AF sources can also been detected in other regions of the atria such as the superior vena cava, left posterior free wall, crista terminalis or the coronary sinus [Haïssaguerre 1998, Jais 1997].

Currently, due to the important role of the PVs in paroxysmal AF, the most commonly used ablation protocol is the circumferential pulmonary vein isolation [Haïssaguerre 1998, Oral 2002], with success rates of 70% in patients with paroxysmal AF and 22% in patients with persistent AF [Oral 2002]. However, this ablation protocol is still not effective in the restoration of the sinus rhythm in a large number of patients [Atienza 2009]. Consequently, several research groups are studying how to effectively locate and isolate the AF sources by developing different strategies to terminate the arrhythmia. One strategy consists on the extensive anatomical ablation combining PVs isolation with additional linear lesions along the left atrial roof, mitral annulus and other atrial structures [Haïssaguerre 2005]. However, different strategies based on an electrogram-guided identification of the specific primary AF source can be performed in order to increase the success ratios or to decrease the area of the lessions [Calkins 2012], namely the complex fractionated atrial electrogram (CFAE) ablation or the highest dominant frequency (DF) ablation.

The CFAES are related to the complexity of AF activation. CFAE ablation is based on the assumption that primary AF sources are located where the EGMs are more fractionated and complex. However, the results of CFAES location as an AF source are still controversial. While some authors affirm that AF termination by targeting CFAES had success for the 95% of the patients with no drug treatment [Nadenamee 2004], other authors achieved a success for the same conditions of only 20% [Porter 2008], 16% [Oral 2007] or 14% [Verma 2011].

As commented in the previous section, some authors support that the initiation and maintenance of AF, specially paroxysmal AF, is caused by a region with a faster electrical activity [Mansour 2001, Atienza 2006, Atienza 2009] (see Figure 2.17). Atienza et al. and Lazar et al. supported the premise that the ablation of the highest DF of the atria terminates the AF [Lazar 2006, Atienza 2009, Berenfeld 2000]. Atienza et al. also showed that the ablation success in patients without frequency gradients was very low, corresponding in most cases with patients with persistent AF [Lazar 2006, Atienza 2009], allowing not only to locate the AF sources, but also to avoid unnecessary ablation procedures.

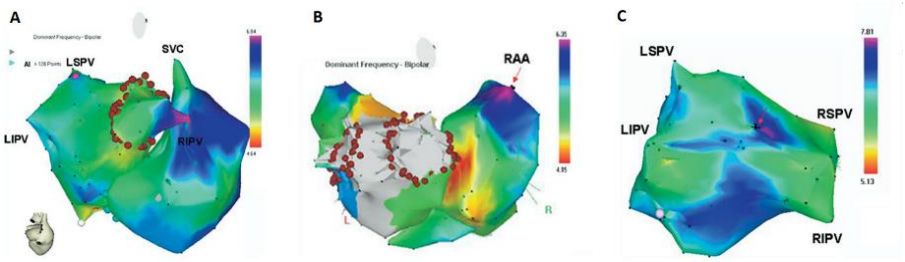

Figure 2.17: Real-time atria DF map obtained by the CARTO system in three AF patients [Atienza 2009]. *(A)* Paroxysmal AF Patient with a high dominant region located in the right superior pulmonary vein. The AF terminated when this region was ablated. *(B)* Paroxysmal AF Patient with a high dominant region located in the right atria appendix. The AF also terminated when this region was ablated. *(C)* Persistent AF patient with no frequency gradient. The AF did not terminate after the ablation procedure.

2.2.3. Ventricular arrhythmias: Brugada syndrome

As opposed to atrial fibrillation, ventricular fibrillation is a lethal arrhythmia, caused by a reentrant activation pattern on the ventricles (Figure 2.18), typically caused by reentry at anatomical obstacles caused by ischemia or infarction, leading to an ineffective contraction of the ventricles and death. ECG tracings during VF present a chaotic signal resulting from the disorganized activity of the ventricles and PQRST complexes cannot be observed (Figure 2.18).

Among non-ischemic causes of VF, mutations in the genes encoding cardiac channels account for 5% sudden cardiac deaths in infants and young adults. *Brugada syndrome* (BrS), is a heritable arrhythmia syndrome that causes sudden death in young adults and, to a lesser degree, in infants and children, with structurally normal hearts [Brugada 1992, Antzelevitch 2005_a]. The disease affects at approximately 0.05 % of the population and is the leading cause of natural death of men under the age of 40 in regions where the disease is endemic [Antzelevitch 2005_a].

BrS has always been linked to mutations in the gene SCN5A that encodes the sodium ionic channel of the cellular membrane. However, although the SCN5A gene is linked to 25-30% of BrS cases, recent studies have identified 16 genes (including SCN5A) that encode mainly subunits of cardiac sodium, potassium and calcium channels responsible for up to 35% of the BrS cases [Campuzano 2013]. However, 65% of the BrS cases still remain with no genetic cause identified.

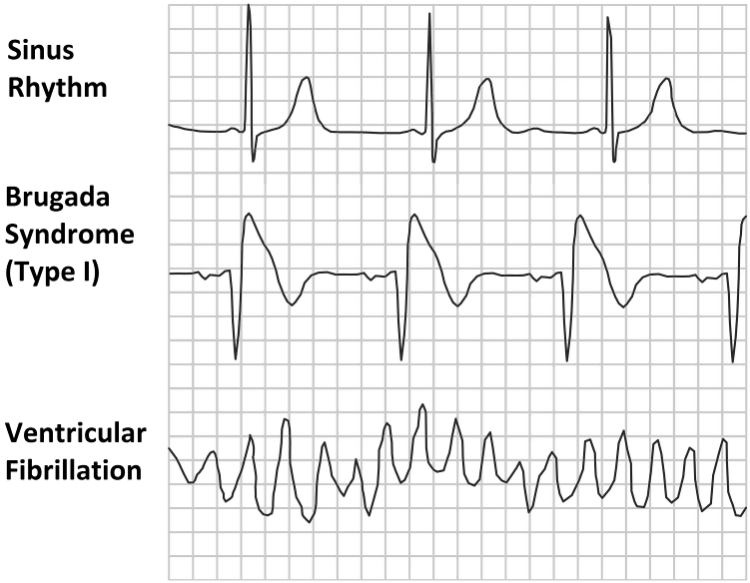

Figure 2.18: Sinus rhythm, Brugada syndrome (Type I) and Ventricular fibrillation wave morphologies.

The clinical manifestation is often dynamic and shows variations over time, which hinders the diagnosis of the syndrome with standard ECGs. Three types of different ECGs have been described (see Figure 2.19). However, 51% of BrS patients could have BrS without presenting any abnormality at the ECG recording [Richter 2009, Wilde 2002]. The type I (BrS-I), consistent in a coved-type ST segment ≥2 mm (0.2 mV) in right precordial leads followed by a negative T wave, is the most characteristic ECG in the BrS but only 24 % of the patients with BrS present it [Richter 2009]. BrS type II or type III (BrS-II and BrS-III) is present in 25% of the patients. BrS-II is characterized by a saddleback appearance with a high take-off ST segment elevation of ≥2mm followed by a trough displaying ≥1mm ST elevation followed by either a positive or biphasic T wave. BrS-III presents a saddleback or coved appearance with a ST segment elevation of <1mm [Wilde 2002, Brugada 1992].

Since BrS has a genetic origin, the clinical and familiar history of the patient is used to predict the syndrome. Due to dynamicity and variations over time of the clinical manifestation, BrS-II or Br-III are not considered as diagnosis unless converted to a type I ECG after administration of ajmaline or flecainide, becoming the main diagnostic tool for BrS [Antzelevitch 2005_a].

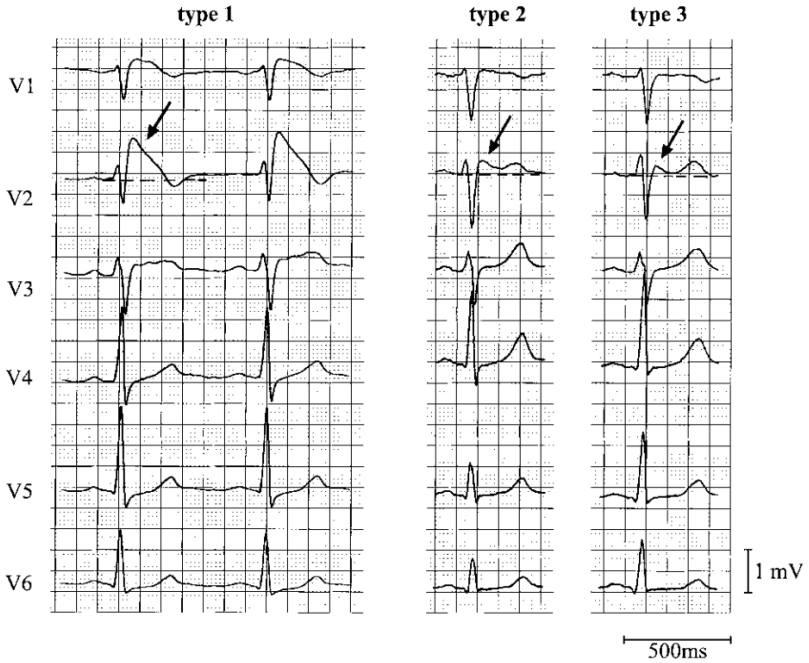

Figure 2.19: Precordial leads of a resuscitated patient with Brugada syndrome [Wilde 2002]**.** The patient presented the 3 different types of the BrS ECG over time.

2.2.3.1. Pathophysiological mechanisms of Brugada syndrome

Experimental studies demonstrated that ECG recordings in BrS patients present late potentials, caused by heterogeneity and slow conduction in the anterior wall of the right ventricular outflow tract (RVOT). However, the relationship between depolarization and repolarization abnormalities and the genesis of the surface ECG is not completely understood, leading to different theories that explain the mechanisms underlying the electrocardiographic and arrhythmic manifestations of the BrS [Wilde 2010, Meregalli 2005]. Some groups support the hypothesis that the main cause of the observed ECG in BrS is a depolarization delay in the RVOT region due to slow conduction and structural abnormalities [Wilde 2010, Postema 2008] as depicted in Figure 2.20, but on the other hand, other groups support that it may be caused by transmural dispersion of repolarization between the endocardium end the epicardium of the RVOT region [Nademanee 2011, Antzelewitch 2002, Antzelewitch 2001, Morita 2010], as depicted in Figure 2.21 and 2.22.

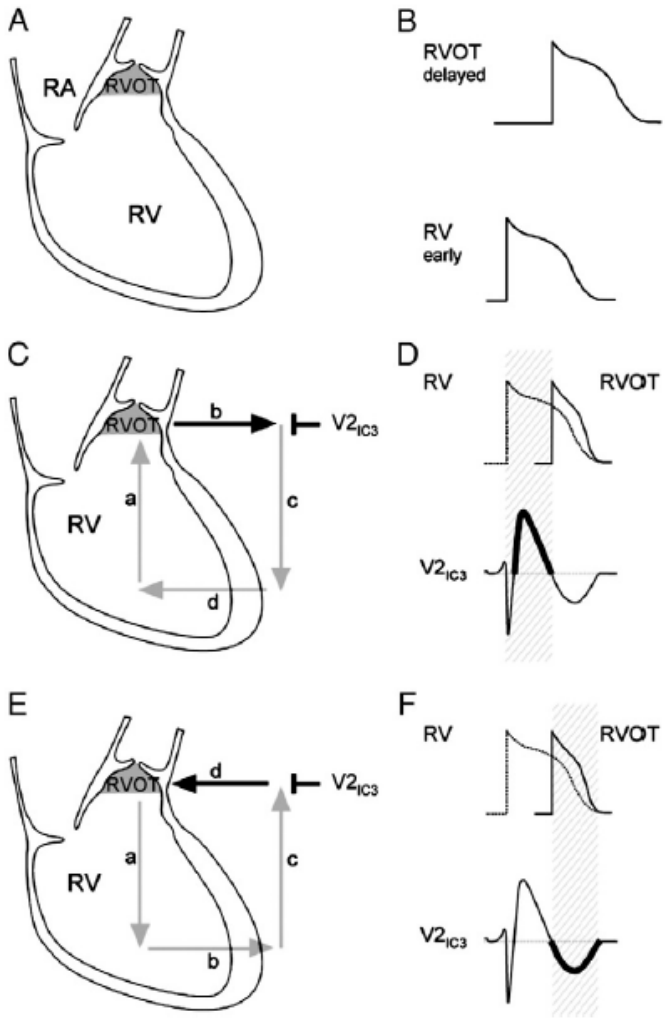

Figure 2.20: Qualitative model of the depolarization hypothesis for the BrS-I ECG [Meregalli 2005, Wilde 2010]**.** *(A and B)* Late activation of the RVOT with respect to the right ventricle (RV). *(C and D)* First depolarization of the RV, RV acts as a current source and RVOT tissue acts as a sink, generating an ST elevation in the V1-V3 electrodes. *(E and F)* Late depolarization of the RVOT, RVOT acts as a current source and RV tissue acts as a sink, resulting in a T negative wave.

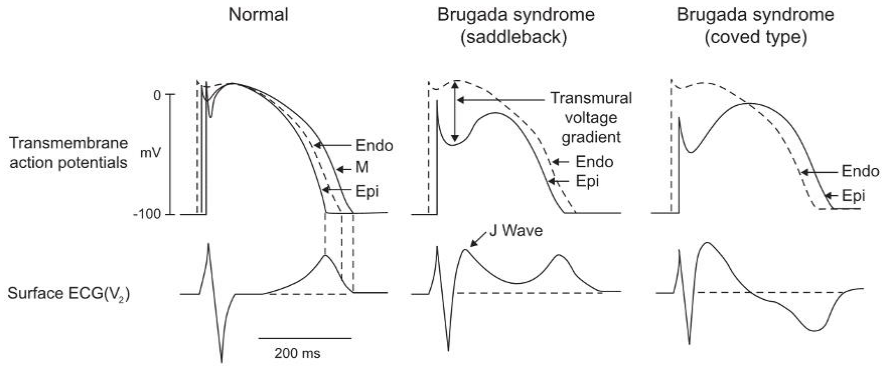

Figure 2.21: Mechanisms underlying abnormal action potential and ST-segment elevation in Brugada syndrome [Antzelevitch 2001, Antzelevitch 2002]. BrS ECG due to transmural dispersion of repolarization between the endocardium end the epicardium of the RVOT region.

Supporting the repolarization theory, Antzelevitch et al. proved the importance of some ionic channels behavior, as I_{Na}, I_K, I_{Cl}, I_{Ca} or I_{to} (Figure 2.22), for the ventricular tachycardia or ventricular fibrillation triggering [Antzelevitch 2001]. Antzelevitch et al. proposed that epicardial and transmural circus movement reentries, favored by a prominent I_{to}, lead to VT and VF (Figure 2.22).

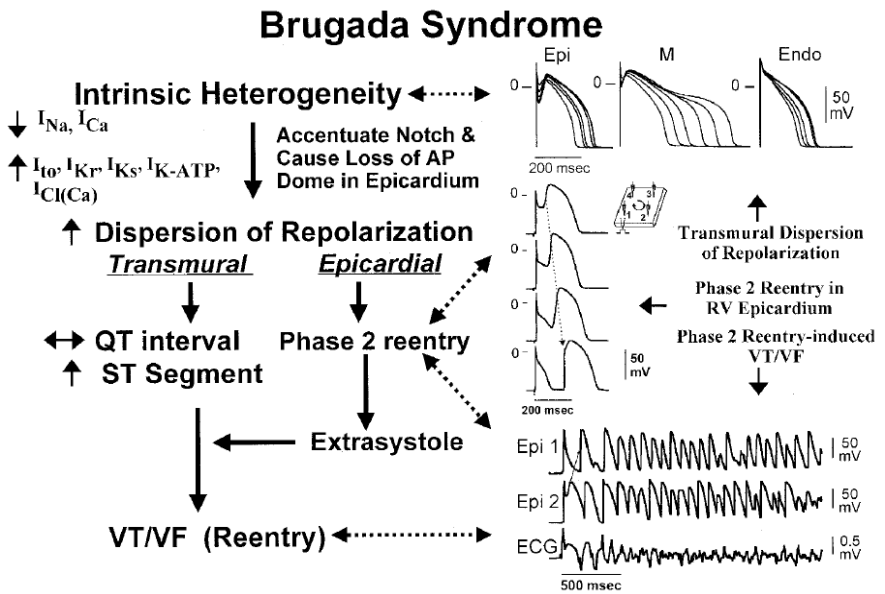

Figure 2.22: Cellular ionic mechanisms proposed for BrS arrhythmogenesis [Antzelevitch 2001]**.**

2.2.3.2. Clinical treatment of Brugada syndrome

In this section we will explain the most important treatments for BrS, the pharmacological and the implantable devices. BrS is due to abnormalities in the function of cellular ionic channels, causing imbalance of inward and outward currents which leads to an action potential modification in the right ventricular epicardium [Antzelewitch 1998]. Different studies have tested pharmacological treatments against BrS like quinidine, tedisamil or 4-aminopyridine, which may restore characteristic action potential dome and electrical homogeneity and, thereby, would terminate the arrhythmia. Quinidine has been found to be effective against BrS, normalizing the ST segment by depressing the effect of the sodium channel current and inhibiting I_{to} in the right ventricular epicardium [Antzelewitch 1998, Yan 1999]. However, although some authors explain that some patients have a poor response to antiarrhythmic drugs [Belhassen 1999, Antzelewitch 2005_a (chap 17)], having no success to prevent new episodes of VF [Brugada 2000, Kuck 2000, Antzelewitch 2005_a (chap 17)], other authors encourage the use of drugs for BrS treatment instead of preventing sudden death directly by using implantable cardioverter defibrillator without a previous study for identifying drug-responder patients [Belhassen 2002].

Some studies affirm that implantable cardioverter defibrillator (ICD) is the only proven effective treatment for BrS [Kuck 2000, Brugada 2000]. Unlike the drug therapy, this method does not solve the underlying cause of BrS but it prevents from the lethal consequence of the disease, VF, proving a high efficacy to revert it [Kuck 2000, Connoly 2000], decreasing the mortality due to the disease.

2.3. The mathematical bioelectrical field formulation

The following section describes the mathematical expressions of the bioelectromagnetic fields that apply to the heart-torso transfer matrix computation [Sarvas 1987, Geselowitz 1967]. The magnetic and electric fields are generated by a current density. To obtain the electric and magnetic fields caused by a low frequency bioelectrical source, Maxwell equations (equations 1) apply [Geselowitz 1967, Plonsey 1969].

$$\vec{\nabla} \cdot \vec{E} = \rho / \varepsilon_0 \tag{1.a}$$

$$\vec{\nabla} \times \vec{B} = \mu_0 \vec{J} + \mu_0 \varepsilon_0 \frac{\partial \vec{E}}{\partial t} \tag{1.b}$$

$$\vec{\nabla} \cdot \vec{B} = 0 \tag{1.c}$$

$$\vec{\nabla} \times \vec{E} = -\frac{\partial \vec{B}}{\partial t} \tag{1.d}$$

$$\vec{J} = \vec{J}^i + \sigma \vec{E} \tag{1.e}$$

In a quasi-static problem, these equations can be simplified as follows:

$$\vec{\nabla} \cdot \vec{E} = \rho / \varepsilon_0 \tag{2.a}$$

$$\vec{\nabla} \times \vec{B} = \mu_0 \vec{J} \tag{2.b}$$

$$\vec{\nabla} \cdot \vec{B} = 0 \tag{2.c}$$

$$\vec{J} = \vec{J}^i + \sigma \vec{E} \tag{2.d}$$

where $\vec{E}$ is electric field; $\vec{B}$ is the magnetic field; $\vec{J}^i$ is the current density generated by the bioelectric source; $\vec{J}$ is the total current density; σ is the conductivity of the medium; ε_0 and μ_0 are the electric and magnetic permeability in vacuum.

$\vec{E}$ is a conservative field $\vec{E} = -\vec{\nabla} V$ and then,

$$\vec{J} = \vec{J}^i - \sigma \vec{\nabla} V \tag{3}$$

And knowing that, following the law of conservation of charge, $\vec{J}$ is a solenoidal field, $\vec{\nabla} \cdot \vec{J} = 0$; therefore:

$$\vec{\nabla}(\sigma \vec{\nabla} V) = \vec{\nabla} \cdot \vec{J}^{\,i} \tag{4}$$

2.3.1. Field in an infinite homogeneous medium

Assuming a constant conductivity σ in the whole space, equation (4) is turned into:

$$\sigma \nabla^2 V = \vec{\nabla} \cdot \vec{J}^{\,i} \tag{5}$$

Solving the Poisson equation (5), the following solution is obtained:

$$V_0(\vec{r}) = -\frac{1}{4\pi\sigma} \int_G \frac{\vec{\nabla}' \cdot \vec{J}^{\,i}(\vec{r}')}{|\vec{r} - \vec{r}'|} dv' \tag{6}$$

where $V_0(\vec{r})$ is the potential at the point $\vec{r}$ in an infinite homogeneous medium; $\vec{r}'$ is the position of the electrical source; G is the volume conductor with a conductivity σ where $\vec{J}^{\,i}$ is located.

Making the following transformations:

$$\vec{\nabla}' \cdot (\vec{J}^{\,i}(\vec{r}')|\vec{r} - \vec{r}'|^{-1}) = |\vec{r} - \vec{r}'|^{-1} \vec{\nabla}' \cdot \vec{J}^{\,i}(\vec{r}') + \vec{J}^{\,i}(\vec{r}') \cdot \vec{\nabla}' \left(|\vec{r} - \vec{r}'|^{-1} \right) \tag{7.a}$$

$$-|\vec{r} - \vec{r}'|^{-1} \vec{\nabla}' \cdot \vec{J}^{\,i}(\vec{r}') = \vec{J}^{\,i}(\vec{r}') \cdot \vec{\nabla}' \left(|\vec{r} - \vec{r}'|^{-1} \right) - \vec{\nabla}' \cdot (\vec{J}^{\,i}(\vec{r}')|\vec{r} - \vec{r}'|^{-1}) \tag{7.b}$$

$$\vec{\nabla}' \left(|\vec{r} - \vec{r}'|^{-1} \right) = |\vec{r} - \vec{r}'|^{-3} (\vec{r} - \vec{r}') \tag{7.c}$$

Replacing the equation (6) with (7.b) and using the transformation in (7.c), we obtain,

$$V_0(\vec{r}) = \frac{1}{4\pi\sigma} \int_G \left[\vec{J}^{\,i}(\vec{r}') \cdot \frac{\vec{r} - \vec{r}'}{|\vec{r} - \vec{r}'|^3} - \vec{\nabla}' \cdot \frac{\vec{J}^{\,i}(\vec{r}')}{|\vec{r} - \vec{r}'|} \right] dv' \tag{8}$$

If the Gauss theorem is applied to the second term of the equation (8), the term $\int_S J^i(\vec{r}')/|\vec{r}-\vec{r}'|\cdot d\vec{S}$ equals 0 because $\vec{J}^i = 0$ on the surface S bounding the volume *G*.

In an infinite homogeneous medium, equation (8) is simplified into equation (9):

$$V_0(\vec{r}) = \frac{1}{4\pi\sigma}\int_G J^i(\vec{r}')\cdot\frac{\vec{r}-\vec{r}'}{|\vec{r}-\vec{r}'|^3}dv' \qquad (9)$$

Finally, by modelling the electric source as a bioelectrical dipole, equation (9) turns into equation (10):

$$V_0(\vec{r}) = \frac{1}{4\pi\sigma}Q\frac{\vec{r}-\vec{r}'}{|\vec{r}-\vec{r}'|^3} \qquad (10)$$

Where *Q* is the bipolar source moment.

2.3.2. Field in a finite inhomogeneous medium: the Boundary Element Method

This section describes the mathematical expressions of the BEM for the field potentials computation in a finite inhomogeneous medium, based on the bioelectromagnetic field formulation and the Green theorem application [Sarvas 1987, Geselowitz 1967], converting the potential volume problem in a surface problem system. This method considers that the volume conductor is divided into different volume regions with homogeneous conductivity limited by a surface boundary S_j, with internal and external conductivities σ' and σ''.

The current, potential, and the distance functions are continuous at each surface boundary and, therefore:

$$\sigma'\vec{\nabla}V'\cdot d\vec{S}_j = \sigma''\vec{\nabla}V''\cdot d\vec{S}_j \qquad (11)$$

$$V'(\vec{S}_j) = V''(\vec{S}_j) \qquad (12)$$

$$\vec{r}'(\vec{S}_j) = \vec{r}''(\vec{S}_j) \qquad (13)$$

where S_j is the interface between volumes with different conductivities; σ' and σ'' are the conductivities of the inner and outer faces respectively; dS_j is a differential element of S_j.

Green's theorem states that [Geselowitz 1967]:

$$\sum_j \int_{vj} \left[\psi \vec{\nabla} \cdot \sigma_j \vec{\nabla} \phi - \phi \vec{\nabla} \cdot \sigma_j \vec{\nabla} \psi\right] dv_j = \sum_j \int_{Sj} \left[\sigma_j' \left(\psi' \vec{\nabla} \phi' - \phi' \vec{\nabla} \psi'\right) - \sigma_j'' \left(\psi'' \vec{\nabla} \phi'' - \phi'' \vec{\nabla} \psi''\right)\right] \cdot d\vec{S}_j \quad (14)$$

where v_j is the volume of a region with a conductivity σ'; dv_j is a volume differential; ψ and ϕ are two functions that exist in each region.

For the particular problem of the bioelectric potential in an inhomogeneous volume conductor calculation: $\psi = 1/\vec{R} = 1/|\vec{r} - \vec{r}'|$, where $\vec{R}$ is the vector distance between the source and the location where the field is calculated, and $\phi = V$ the unknown potentials. Replacing in equation (14),

$$\sum_j \int_{vj} \left[\frac{1}{|\vec{r} - \vec{r}'|} \vec{\nabla} \cdot \sigma_j \vec{\nabla} V - V \vec{\nabla} \cdot \sigma_j \vec{\nabla} \left(\frac{1}{|\vec{r} - \vec{r}'|}\right)\right] dv_j = = \sum_j \int_{Sj} \left[\sigma_j' \left(\frac{1}{|\vec{r} - \vec{r}'|} \vec{\nabla} V' - V' \vec{\nabla} \left(\frac{1}{|\vec{r} - \vec{r}'|}\right)\right) - \sigma_j'' \left(\frac{1}{|\vec{r} - \vec{r}'|} \vec{\nabla} V'' - V'' \vec{\nabla} \left(\frac{1}{|\vec{r} - \vec{r}'|}\right)\right)\right] \cdot d\vec{S}_j \quad (15)$$

Knowing that,

$$\sum_j \int_{vj} \left[\vec{\nabla} \cdot \vec{\nabla} \left(\frac{1}{|\vec{r} - \vec{r}'|}\right)\right] dv_j = 4\pi \quad (16)$$

Simplifying and grouping the two terms of the equation,

$$\sum_j \int_{vj} \left(\frac{1}{|\vec{r} - \vec{r}'|} \vec{\nabla} \cdot \vec{J}^i(\vec{r}') \right) dv_j + 4\pi\sigma(\vec{r})V(\vec{r}) =$$

$$= \sum_j \int_{Sj} \left[\left(\sigma_j' \vec{\nabla} V' - \sigma_j'' \vec{\nabla} V'' \right) \left(\frac{1}{|\vec{r} - \vec{r}'|} \right) - \left(\sigma_j' V' - \sigma_j'' V'' \right) \vec{\nabla} \left(\frac{1}{|\vec{r} - \vec{r}'|} \right) \right] \cdot d\vec{S}_j \tag{17}$$

Solving the equation and using the boundary conditions,

$$V(\vec{r}) = -\frac{1}{4\pi\sigma(\vec{r})} \sum_j \int_{vj} \left[\frac{1}{|\vec{r} - \vec{r}'|} \vec{\nabla} \cdot \vec{J}^i(\vec{r}') \right] dv_j - \frac{1}{4\pi\sigma(\vec{r})} \sum_j \left(\sigma_j' - \sigma_j'' \right) \int_{Sj} \left[V(\vec{r}') \vec{\nabla} \left(\frac{1}{|\vec{r} - \vec{r}'|} \right) \right] \cdot d\vec{S}_j$$

(18)

$$V(\vec{r}) = V_0 - \frac{1}{4\pi\sigma(\vec{r})} \sum_j \left(\sigma_j' - \sigma_j'' \right) \int_{Sj} \left[V(\vec{r}') \vec{n}(\vec{r}') \cdot \vec{\nabla} \left(\frac{1}{|\vec{r} - \vec{r}'|} \right) \right] \cdot dS_j \tag{19}$$

$$V(\vec{r}) = V_0 - \frac{1}{4\pi\sigma(\vec{r})} \sum_j \left(\sigma_j' - \sigma_j'' \right) \int_{Sj} \left[V(\vec{r}') \vec{n}(\vec{r}') \cdot \frac{\vec{r} - \vec{r}'}{|\vec{r} - \vec{r}'|^3} \right] \cdot dS_j \tag{20}$$

where $V(\vec{r})$ is the potential at a point $\vec{r}$; $\vec{n}$ is the normal vector to the different S_j ; $\sigma(\vec{r})$ is the conductivity of the volume conductor at which the potential is calculated.

The integral of equation (20) is not continuous in $\vec{r}$ for a surface S_j, because $\sigma(\vec{r})$ is not continuous in *r*, therefore in this case a new approach is required:

$$\frac{\sigma'_k + \sigma''_k}{2} V(\vec{r}) = \sigma_n V_0(\vec{r}) - \sum_{j=1}^{N} \frac{\sigma'_j - \sigma''_j}{4\pi} \int_{S_j} V(\vec{r}') \vec{n}(r') \cdot \frac{\vec{r} - \vec{r}'}{|\vec{r} - \vec{r}'|^3} dS_j \tag{21}$$

where σ'_k y σ''_k are the conductivities in the inner and outer faces of the boundary surface *k* where the potential is calculated.

2.4. The Forward and Inverse problems of electrocardiography

The main purpose of electrocardiography is to relate the electrical activity generated on the myocardium and the potentials recorded on the torso surface, allowing a better qualitative and quantitative understanding of the electrical activity of the heart. This thesis focuses on the challenge of establishing such relationship by solving the forward and inverse problems of electrocardiography (see Figure 2.23).

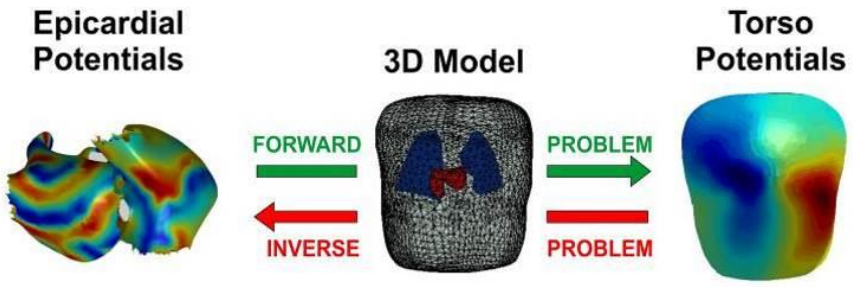

Figure 2.23: Forward and Inverse problem of electrocardiography. In this figure, both problems were solved for the atria of the heart.

The forward problem of electrocardiography involves the computation of the potential on the torso surface by using as inputs the electrical activity of the heart and the transfer matrix heart-torso (Figure 2.23). The transfer matrix is computed by considering the geometry, reconstructed by computer axial tomography or magnetic resonance image segmentation, and the conductivities of the different volume conductors comprising the torso. The forward problem is characterized to be well-conditioned, well-posed and stable, having a unique solution to the mathematical problem that depends continuously with the data that defines the problem. [MacLeod 1998, Hadamard 1902]. The forward problem can be solved according to equation (22):

$$U_T = MU_H \qquad (22)$$

where U_T is the matrix with the potentials on the torso surface, M is the heart-torso transfer matrix, U_H is the matrix with the potentials on the heart.

The forward problem has a limited direct application to clinical field since in the clinical practice we typically know the potentials on the torso and not in the myocardium. However, the forward problem is important to understand the

relationship between the electrical activity of the heart and the recorded ECGs on the torso surface. Cardiac mathematical models are used to simulate cardiac arrhythmias and, in this way, the studied hypothesis of the cardiac diseases mechanisms can be validated by numerically generating the torso potentials associated to the simulated conditions (see Figure 2.24) [Rodrigo 2014, Pedrón-Torrecilla 2014, Liberos 2013]. By using this approach, the effects on the ECG of alteration in ion channels caused by either genetic mutations or drugs, aging or ambient factors can be modeled and compared to the observed ECGs in patients.

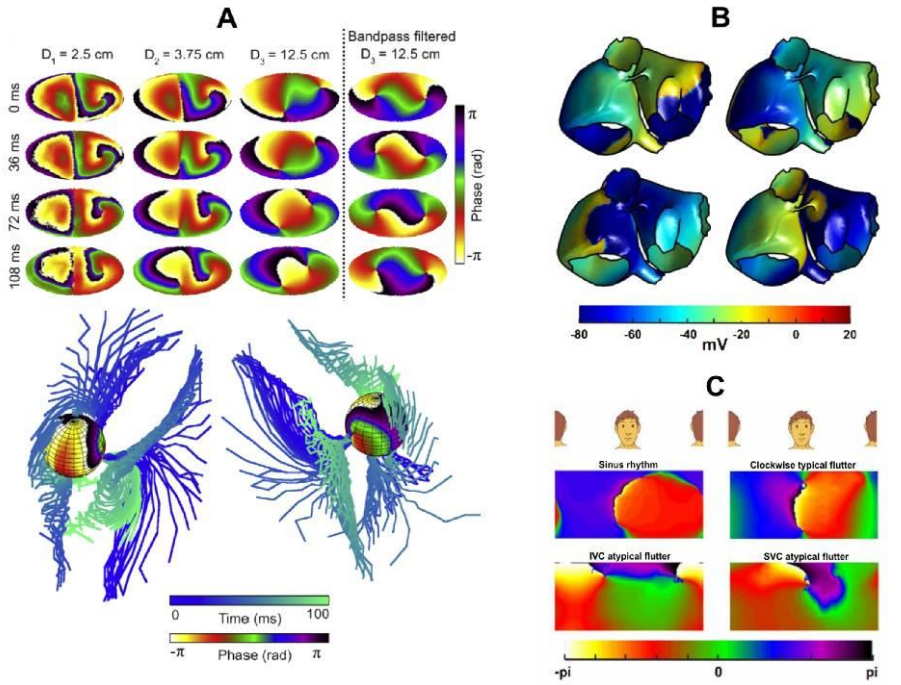

Figure 2.24: Applications of the forward problem for atrial disease studies. *(A)* Epicardial and transition to surface phase maps during AF. Phase maps at 4 instants at increasing distances from the epicardium computed with the forward problem [Rodrigo 2014]. *(B)* Mathematical model computed for atrial clockwise typical atrial flutter (AFL) [Liberos 2014]. *(C)* Calculation of torso phase maps during sinus rhythm, clockwise typical AFL and atypical AFL around inferior vena cava (IVC) and superior vena cava (SVC) [Liberos 2013].

On the other hand, the inverse problem of electrocardiography involves the computation of the electrical activity of the heart by using as inputs the torso surface potentials and the described transfer matrix heart-torso (Figure 2.23). Unlike the forward problem, the inverse problem is of great importance in clinical practice since it allows the noninvasive reconstruction of the myocardial activity, easily

interpretable by medical staff. However, the inverse problem is ill-posed, very unstable and has multiple possible solutions since the equations of the system are almost linearly dependent, presenting a high condition number and then, a small error in the initial data can result in a large error in the solution [Hadamard 1902, Hadamard 1923]. Consequently, it needs additional constrains and numerical regularization methods for the correct torso-heart transfer matrix computation, essential for an accurate resolution of the problem [MacLeod 1998, Tikhonov 1963, Horácek 1997, Rudy 1988]. It is very important to keep always in mind that the inverse problem cannot be solved by using equation (23) directly, because of the ill-conditioned nature of the problem.

$$U_H = M^{-1}U_T \tag{23}$$

The following sections will explain the mathematical procedure to compute the forward and inverse problems of electrocardiography.

2.5. Methods for the computation of the transfer matrix

In order to solve the forward and inverse problem of electrocardiography, the transfer matrix needs to be computed. There are several numerical methods for computing the heart-torso transfer matrix based on differential equations, like the finite element method, the finite difference method and the finite volume method; or fundamental-solution based approaches like the boundary element method. The finite element method (FEM) and the boundary element method (BEM) are the most commonly used [Seger 2005, Fischer 2000].

Differential equation based approaches can deal with inhomogeneous and anisotropic conductivities since they involve discretizing the whole volume conductor. However, they need a full volumetric mesh, considering a large number of unknowns for the system resolution [Seger 2005].

The finite difference method (FDM), as based on differential equations method, discretize the torso volume with a three dimensional grid of nodes. The method is based on the Kirchhoff's law resolution for each node, modelling the torso conductivity by introducing resistive elements between the nodes, resulting in an equation system that relates the potential between adjacent nodes. Accuracy of FDM is sensitive to both the node density and the estimated resistive elements values [Gulrajani 1997, Walker 1987]. The FDM represents a discrete approximation to equation (4), which allows computing the voltage generated by a current density.

The finite element method (FEM) is also based on a three dimensional mesh, however, in this case the geometry is approximated by contiguous volume elements of simple geometrical shapes like tetrahedrons or hexahedrons. This method also solves equation (4) in conjunction with potential and current densities boundary conditions [Gulrajani 1997, Seger 2005, Huebner 1987, Fischer 2000, Yamashita 1984]. FEM equations can be solved by the weighted residual approximation, (i.e. Garleking's method), thus obtaining the following integral expression:

$$\int_{v} \beta_k \left[\vec{\nabla} \cdot \left(\sigma \vec{\nabla} V\right)\right] dv + \int_{v_H} \beta_k \left[\vec{\nabla} \cdot \vec{J}\right] dv = 0 \quad k = 1,2,\ldots,m \qquad (24)$$

where v_H is the volume of the heart (or primary source); v is the volume that is not a primary source; m is the number of the unknown potentials of the system being nodes delimiting the volume. β_k are interpolating polynomials, generally chosen for having a continuous potential distribution between interfaces.

The finite volume method (FVM) is similar to the finite element method but, in this case, the potentials are computed at the center of each volume element having no variation of the potential within an element, needing a fine discretization for achieving a good accuracy [Gulrajani 1997, Abboud 1994, Rosenfeld 1996].

The FVM involves solving then the integral:

$$\int_{v} \vec{\nabla} \cdot \left(\sigma \vec{\nabla} V\right) dv + \int_{v_H} \vec{\nabla} \cdot \vec{J} dv = 0 \qquad (25)$$

The main advantage of fundamental-solution based approach methods, like the BEM, is that they only require discretization of the boundary surfaces of the different conductor volumes that are assumed to be isotropic and homogeneous. Therefore, it is unnecessary to discretize the whole volume conductor, which reduces the amount of nodes used for the calculation of the potential and involves approximations only in the boundaries. The BEM takes advantage of the Green's theorem for converting the potential volume problem in a surface problem (see Equation (14) and (15)). However, the main limitation of this method is that it can only be applied to systems whose conductive regions are isotropic and homogeneous [Seger 2005, Frijns 2000].

2.6. Methods for the inverse problem resolution

As it was exposed previously, the inverse problem is ill-posed and then, very unstable in the presence of noise and geometry-dependent, needing to be stabilized by imposing additional constrains before solving the problem. In this section, different solutions for solving the inverse problem are presented.

For localized sources in the heart, the electrical activity of the heart can be modelled in terms of multiple coefficients, moving-dipole or multiple dipole models, being of great importance in the clinical practice since it is the basis of the ECG generation used to diagnose the cardiac health of a patient [Frank 1954, Pilkington 1982, Malmivuo 1995]. This electrical model is widely studied and evaluated in the electrocardiographic domain for determining the surface potentials from current dipoles by solving the forward problem of electrocardiography [Barr 1966, Geselowitz 1960, Savard 1982]. The calculation of the electrical activity of the heart from the torso potentials in terms of dipolar sources is also possible. The noninvasive determination of the resultant dipole of the heart by solving the inverse problem was first introduced by Gabor and Nelson [Gabor 1954] and is still widely studied by the research community for simple propagation patterns, supporting the method for identifying and locating noninvasively the cardiac sources of electric current and providing the approximate site of origin of a cardiac ectopic activity [Gabor 1954, Lai 2010, Purcell 1991, Hren 1998, Armoundas 2003, Fukuoka 2006].

Different solution for the dipolar inverse problem resolution was proposed by the scientific community:

In the multipole-series modelling, the heart sources are characterized by an infinite series of multipolar current generators like dipoles, quadrupoles, octapoles, etc [Arthur 1972]. These cardiac sources are located at a fixed common origin, i.e. the center of the heart. The solution of the inverse problem can be achieved by minimizing the error between the recorded torso potentials and the computed torso potentials with the multipole coefficient matrix, as described in the following equation:

$$\min\left\{\left\|M\,X - U_T\right\|^2\right\} \tag{26}$$

where X is the multiple coefficient matrix.

Obtaining the following equation:

$$X = \left(M^t M\right)^{-1} M^t U_T \tag{27}$$

Fukuoka et al. and Nelder proposed a solution for locating a single moving dipole for a realistic torso, representing the electrical activity of the heart by one or

two moving dipoles [Fukuoka 2006, Nelder 1965]. This method for inverse-computing the electrical activity of the heart is based on the selection of the amplitude and coordinates of the dipoles within a torso model. This method also solves the equation 2.25 following the same principle of function minimization. However, in this case, the number of unknowns is 6 per dipole in the system (x, y, z dipolar location and x, y, z orientation) [Lai 2010, Nelder 1965] and then, the relation between the potential at an arbitrary site and the coordinates of the dipoles is nonlinear, needing nonlinear iterative techniques, such as the Levengerg-Marquardt method [Ralston 1978] for contracting on to the final minimum error, instead of solving the equation 26 directly.

Although the interpretation of equivalent dipoles is very easy and the inverse problem resolution is less ill-posed due to stronger constrains of the solution, the diagnosis in terms of a dipolar model is typically qualitative rather quantitative and it is based more on pattern recognition than on biophysical modeling [Gulrajani 1997, McLeod 1998]. Hence, inverse problem resolution for one or two moving dipoles can only be used when real heart sources consist of one or two localized centers of activity respectively, without considering multiple wavefronts propagation patterns [Gulrajani 1997].

The more general method for inverse computing the actual intracardiac source is in terms of potential distributions. Although this technique is more ambiguous than the dipolar resolution and requires further processing, it provides the reconstructed intracardiac electrograms for multiple sources propagation patterns [Barr 1976, Barr 1977, Rudy 1988, Horácek 1997, Messinger-Rapport 1990, Cuculich 2010]. The full knowledge of the electrical myocardial activity allows a better resolution in the study of the myocardial activity allowing the analysis of the morphology of the electrograms, the isochrones map representation [Zhang 2013, Pedrón-Torrecilla 2012, Roten 2012], the phase [Haïssaguerre 2013] or in the frequency domain. Moreover, epicardial potentials are often measured using invasive techniques and, thus, the inverse problem resolution in terms of potentials can be validated with the intracardiac recording, providing a useful clinical description [Gulrajani 1997].

Due to its ill-posed nature, the inverse problem is incorrectly solved by computing the inverse of the field transfer matrix heart-torso matrix:

$$U_H = M^{-1}U_T \tag{28}$$

However, M is ill-conditioned and consequently the solution of its inverse cannot be found directly. In order to overcome this limitation, the system needs to be regularized, minimizing a weighted sum of two terms. One term is the residual error and the other is a penalty term describing an undesirable property of the solution.

Tikhonov regularization uses as penalty terms the norm of the solution, constraining an excessive amplitude of the solution, and the norm of its spatial derivative, penalizing the lack of smoothness. An added constraint into the inverse

model is used to control the balance between the two terms, calling this weighting parameter "regularization parameter".

Tikhonov regularization method is based on the minimization of the following equation [Rudy 1988, Horáceck 1997, Tikhonov 1979, Tikhonov 1963]:

$$\min\left\{\left\|M U_H - U_T\right\|^2 + \lambda\left\|B U_H\right\|^2\right\} \quad (29)$$

where λ is the regularization parameter and B is a spatial regularization matrix. Therefore, the inverse problem can be solved by using equation (30):

$$\left(M^t M + \lambda B^t B\right) U_H(\lambda) = M^t U_T \quad (30)$$

$$U_H(\lambda) = \left(M^t M + \lambda B^t B\right)^{-1} M^t U_T \quad (31)$$

$$U_H(\lambda) = M_{inv}(\lambda) U_T \quad (32)$$

where M^t and B^t are the transposed matrix of M and B; $M_{inv}(\lambda)$ is the torso-heart transfer matrix, function of the regularization parameter λ.

The constrain matrix B allows the minimization either of the norm of the epicardial potential distribution, being B the identity matrix (zero order); of the surface gradient, being B a discrete approximation of the spatial gradient (first order); or of the surface Laplacian of the epicardial potential distribution (second order).

Tikhonov variants based on the addition of temporal constraints have also been proposed by the scientific community. Twomey et al. explained that if some a priori estimation U_P of the epicardial potential U_H is known [Twomey 1963], then the method described with the equation (29) can be modified as the following equation:

$$\min\left\{\left\|M U_H - U_T\right\|^2 + \lambda\left\|U_H - U_P\right\|^2\right\} \quad (33)$$

Obtaining the following solution:

$$U_H(\lambda) = \left(M^t M + \lambda I\right)^{-1}\left(M^t U_T + \lambda U_P\right) \quad (34)$$

Twomey's method can be applied for the addition of temporal constraints, considering the solution on two prior sampling instants of the epicardial solution [Oster 1992], defining U_P at an instant *j* as shown in the following equation:

$$U_P^j = 2U_H^{j-1} - U_H^{j-2} \tag{35}$$

However, the success of this method is very sensitive to the accuracy of the previous solution and the initial estimation, and thus it is not suitable for complex propagation patterns.

The optimum choice of the regularization parameter λ is of great importance for a correct computation of the solution. For small values of λ, the solution obtained is under regulated and then, very unstable and sensitive to perturbations, leading to oscillation in the computed epicardial potentials solution. On the other hand, large values of λ lead to overregulated solutions where the constraint condition dominates in the solution computation, obtaining over smoothed epicardial potentials. The optimal λ_{opt} lies between these two extremes, trading off between instability and excessive smoothing.

Different methods for the optimal selection of the regularization parameter are suggested, being the composite residual and smoothing operator (CRESO) and the L-Curve the most accepted by the scientific community.

The method of the discrepancy technique allows the selection of λ using as input the standard deviation of the noise in U_T [Morozov 1984]. However, other methods, such as the generalized cross-validation and the maximum likelihood estimator, were able to find λ_{opt} with no a priori knowledge of the noise in U_T [Wahha 1977, Golub 1979]. The composite residual and smoothing operator (CRESO) proposed by Franzone et al. does not require the knowledge of the noise level in U_T and achieved better results than the generalized cross-validation and the maximum likelihood estimator methods [Franzone 1985]. The CRESO approach is based on the smallest $\lambda > 0$ estimation that results in a relative maximum of the following function:

$$B(\lambda) = \left\| U_H(\lambda) \right\|^2 + 2\lambda \frac{d}{d\lambda} \left\| U_H(\lambda) \right\|^2 \tag{36}$$

The method of the L-curve to obtain the regularization parameter λ is a useful graphical method to solve "ill-posed" problems [Hansen 1993, Miller 1970, Horácek 1997]. The L-curve is a log-log representation of the norm of a regularized solution $y = \log_{10}\left\|BU_H(\lambda)\right\|$ versus the corresponding residual norm $x = \log_{10}\left\|MU_H(\lambda) - U_T\right\|$ for different inverse-computed $U_H(\lambda)$ with different regularization parameters values, selecting the point with the maximum curvature, corresponding to the optimal λ_{opt}. As depicted in Figure 2.25, the vertical portion of the L-curve corresponds to solutions obtained with small values of λ, in which the error dominates due to the under regularization, leading to low unfiltered but very unstable solution. The horizontal portion of the curve corresponds to larger values of λ, for which the inverse problem solutions are over regulated and then, obtains a more filtered solution (see Figure 2.25). The L-curve clearly shows the compromise between the minimization of both quantities.

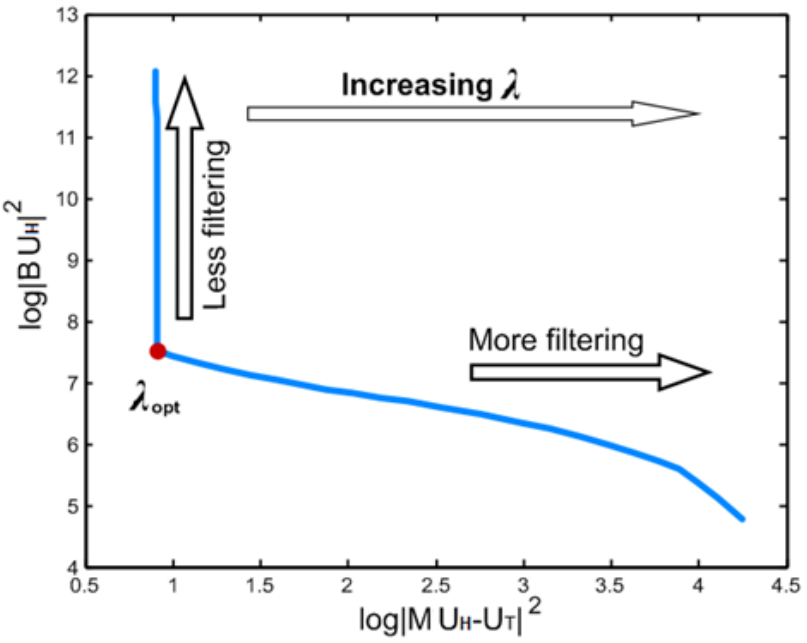

Figure 2.25: L-Curve representation for the inverse problem resolution. λ_{opt} is the optimal regularization parameter selected by the L-Curve, $||BU_H(\lambda)||^2$ is the norm of a regularization solution, $||MU_H(\lambda)-U_T||^2$ is the corresponding residual norm.

3. Methods

3.1. Building the BEM transfer matrix

In this section, the construction of the Boundary Element Method (BEM) transfer matrix and the integral approximations will be presented. Operating with the bioelectromagnetic formulas described in equation (21), we obtain the expression that allows the computation of the potential in an inhomogeneous finite medium [Stenroos 2009, Sarvas 1987, Geselowitz 1967]:

$$\frac{\sigma''_k+\sigma'_k}{2}V(\vec{r})=\sum_{j=1}^{N}\left[\frac{1}{4\pi}\int_{S_j}\frac{\nabla V(\vec{r}')}{|\vec{r}-\vec{r}'|}\vec{n}(\vec{r}')dS_j\right]-\sum_{j=1}^{N}\left[\frac{\sigma'_j-\sigma''_j}{4\pi}\int_{S_j}V(\vec{r}')\vec{n}(\vec{r}')\cdot\frac{\vec{r}-\vec{r}'}{|\vec{r}-\vec{r}'|^3}dS_j\right] \quad (37)$$

The first term in the right side of the equation (37) represents the potential due to a current density associated with the active cells of the myocardium in a homogeneous infinite medium. For a dipolar source case, this term can be replaced by equation (10). The second term represents the contribution of the field arising from surface current distributions of a finite inhomogeneous volume conductor containing a source distribution [Geselowitz 1967]. The contribution of both terms gives the potential at a point of our system.

To solve the problem numerically, the bounding surfaces of the different volume conductors were divided into smaller triangular areas (patches). The potential was calculated assuming that it varies linearly over each triangle and, furthermore, it is continuous in contiguous triangles [De Munck 1992, Schlitt 1995].

We obtained the following equation [Sarvas 1987, Geselowitz 1967]:

$$\frac{\sigma''_k+\sigma'_k}{2}V(\vec{r})=\sum_{j=1}^{N}\left[\frac{1}{4\pi}\sum_{n=1}^{M_j}\Gamma_n\int_{S_n}\frac{dS_n}{|\vec{r}-\vec{r}'|}\right]-\sum_{j=1}^{N}\left[\frac{\sigma'_j-\sigma''_j}{4\pi}\sum_{n=1}^{M_j}U_n\int_{S_n}\frac{\vec{r}-\vec{r}'}{|\vec{r}-\vec{r}'|^3}d\vec{S}_n\right] \quad (38)$$

where U_n is the potential of a patch *n* of the surface S_j of the *j* volume conductor; Γ_n is the gradient of the potential of a patch *n*; dS_n is the differential surface of a

patch of the surface S_j; N is the number of isotropic and homogeneous regions with different conductivities; M_j is the number of patches that integrates each surface of each region j.

Assigning one variable to each integral, they can be simplified as the following equations:

$$\omega_n = \int_{S_n} \frac{\vec{r} - \vec{r}'}{\left|\vec{r} - \vec{r}'\right|^3} d\vec{S}_n \tag{39}$$

$$\alpha_n = \int_{S_n} \frac{dS_n}{\left|\vec{r} - \vec{r}'\right|} \tag{40}$$

where ω_n, is the solid angle subtended at the point $\vec{r}$ by the area dS_n; α_n are coefficients that represent the contribution of the voltage gradient of the surface dS_n at point $\vec{r}$. These integrals were obtained by solving numerical approximation methods which simplify the execution of the algorithm [Barr 1977, Oosterom 1983, De Munck 1992, Cowper 1972].

And simplifying the equation (39) with the equation (40):

$$\frac{\sigma''_k + \sigma'_k}{2} V(\vec{r}) = \sum_{j=1}^{N} \left[\frac{1}{4\pi} \sum_{n=1}^{M_j} \Gamma_n \alpha_n \right] - \sum_{j=1}^{N} \left[\frac{\sigma'_j - \sigma''_j}{4\pi} \sum_{n=1}^{M_j} U_n \omega_n \right] \tag{41}$$

$$\frac{\sigma''_k + \sigma'_k}{2} V(\vec{r}) + \sum_{j=1}^{N} \left[\frac{\sigma'_j - \sigma''_j}{4\pi} \sum_{n=1}^{M_j} U_n \omega_n \right] = \sum_{j=1}^{N} \left[\frac{1}{4\pi} \sum_{n=1}^{M_j} \Gamma_n \alpha_n \right] \tag{42}$$

At this point ω_n and α_n were considered for each triangular patch n. The numerical approximation methods used to solve the corresponding integrals allow working directly with the nodes forming each patch and, consequently, all the nodes of the system. In this way the system will depend on the number of nodes.

With the previous approximation, equation (42) can be represented with the matrix equations system in equation (43) for a system with N different volumes with different conductivities:

$$\left[\begin{pmatrix} \frac{\sigma'_1+\sigma''_1}{2}[I]_{n1\times 1} & \cdots & [0] \\ \vdots & \ddots & \vdots \\ [0] & \cdots & \frac{\sigma'_N+\sigma''_N}{2}[I]_{nN\times nN} \end{pmatrix} + \frac{1}{4\pi}\begin{pmatrix} (\sigma'_1-\sigma''_1)[\Omega_{11}]_{n1\times n1} & \cdots & (\sigma'_N-\sigma''_N)[\Omega_{1N}]_{n1\times nN} \\ \vdots & \ddots & \vdots \\ (\sigma'_1-\sigma''_1)[\Omega_{N1}]_{nN\times n1} & \cdots & (\sigma'_N-\sigma''_N)[\Omega_{NN}]_{nN\times nN} \end{pmatrix}\right] \cdot \begin{pmatrix} [U_1]_{n1\times 1} \\ \vdots \\ [U_N]_{nN\times 1} \end{pmatrix} = \quad (43)$$

$$= \frac{1}{4\pi}\begin{pmatrix} [\alpha_{11}]_{n1\times n1} & \cdots & [\alpha_{1N}]_{n1\times n1} \\ \vdots & \ddots & \vdots \\ [\alpha_{N1}]_{nN\times n1} & \cdots & [\alpha_{NN}]_{nN\times nN} \end{pmatrix} \cdot \begin{pmatrix} [\Gamma_1]_{n1\times 1} \\ \vdots \\ [\Gamma_N]_{nN\times 1} \end{pmatrix}$$

where $[\Omega_{S_X S_Y}]$ is the submatrix which includes all the $\omega_{i,j}$ elements and $\omega_{i,j}$ is the solid angle subtended at point *i* of the surface *X* by point *j* of the surface *Y*; $[\alpha_{S_X S_Y}]$ is the submatrix which includes all the $\alpha_{i,j}$ elements and $\alpha_{i,j}$ is the angle subtended at point *i* of the surface *X* by point *j* of the surface *Y*; $[U_X]$ is the submatrix which includes all the potentials of each node composing the surface *X*; $[\Gamma_X]$ is the submatrix which includes all the gradient potentials of each node composing the surface *X*; *nX* is the number of nodes of the surface X; $[I]$ is an identity matrix.

If we group each term of the previous equation in *D, G*, we obtain the following expressions:

$$D = \begin{bmatrix} \begin{pmatrix} \frac{\sigma'_1+\sigma''_1}{2}[I]_{n1\times n1} & \cdots & [0] \\ \vdots & \ddots & \vdots \\ [0] & \cdots & \frac{\sigma'_N+\sigma''_N}{2}[I]_{nN\times nN} \end{pmatrix} + \\ + \frac{1}{4\pi}\begin{pmatrix} (\sigma'_1-\sigma''_1)[\Omega_{11}]_{n1\times n1} & \cdots & (\sigma'_N-\sigma''_N)[\Omega_{1N}]_{n1\times nN} \\ \vdots & \ddots & \vdots \\ (\sigma'_1-\sigma''_1)[\Omega_{N1}]_{nN\times n1} & \cdots & (\sigma'_N-\sigma''_N)[\Omega_{NN}]_{nN\times nN} \end{pmatrix} \end{bmatrix}$$

$$G = -\frac{1}{4\pi}\begin{pmatrix} [\alpha_{11}]_{n1\times n1} & \cdots & [\alpha_{1N}]_{n1\times n1} \\ \vdots & \ddots & \vdots \\ [\alpha_{N1}]_{nN\times n1} & \cdots & [\alpha_{NN}]_{nN\times nN} \end{pmatrix} \tag{44}$$

$$\begin{pmatrix} D_{11} & \cdots & D_{1N} \\ \vdots & \ddots & \vdots \\ D_{N1} & \cdots & D_{NN} \end{pmatrix} \cdot \begin{pmatrix} U_1 \\ \vdots \\ U_N \end{pmatrix} = -\begin{pmatrix} G_{11} & \cdots & G_{1N} \\ \vdots & \ddots & \vdots \\ G_{N1} & \cdots & G_{NN} \end{pmatrix} \cdot \begin{pmatrix} \Gamma_1 \\ \vdots \\ \Gamma_N \end{pmatrix} \tag{45}$$

where D_{XY} is the coefficient submatrix that represents the contribution of the potential of a surface *Y* to a surface *X;* G_{XY} is the coefficient submatrix that represents the contribution of the voltage gradient of a surface *Y* to a surface *X;* U_X is the vector with the potentials for each node of a surface *X;* G_X is the vector with the potentials gradients for each node of a surface *X*.

In this work we worked with only 2 volume conductors, heart (ventricle or atria) and torso, and then, simplifying the volume conductor model by restricting the system to heart and torso (2 volume conductors) [Horáceck 1997], we obtain equation (46). The ventricle or both atria are considered for calculating matrices $D_{HH}, D_{TH}, D_{HT}, G_{HH}, G_{TH}$ used for the transfer matrix calculation, applying the source superposition theorem.

$$D=\begin{pmatrix} \frac{\sigma'_H+\sigma''_H}{2} I_{N_H} & 0 \\ 0 & \frac{\sigma'_T+\sigma''_T}{2} I_{N_T} \end{pmatrix} + \frac{1}{4\pi}\begin{pmatrix} (\sigma'_H-\sigma''_H)\Omega_{HH} & (\sigma'_T-\sigma''_T)\Omega_{HT} \\ (\sigma'_H-\sigma''_H)\Omega_{TH} & (\sigma'_T-\sigma''_T)\Omega_{TT} \end{pmatrix}$$

$$G=-\frac{1}{4\pi}\begin{pmatrix} \alpha_{HH} & \alpha_{HT} \\ \alpha_{TH} & \alpha_{HT} \end{pmatrix} \quad (46)$$

$$\begin{pmatrix} D_{HH} & D_{HT} \\ D_{TH} & D_{TT} \end{pmatrix} \cdot \begin{pmatrix} U_H \\ U_T \end{pmatrix} = -\begin{pmatrix} G_{HH} & G_{HT} \\ G_{TH} & G_{TT} \end{pmatrix}\begin{pmatrix} \Gamma_H \\ \Gamma_T \end{pmatrix} \quad (47)$$

where U_H is the potential on the myocardium of the heart; U_T is the potential at the surface of the torso; Γ_H is the gradient of the potential of the heart; Γ_T is the gradient of the potential of the torso; D_{HH} is the coefficient matrix that represents the contribution of the potential of a point of the heart to a point of the heart*;* D_{HT} is the coefficient matrix that represents the contribution of the potential of a point of the torso to a point of the heart*;* D_{TH} is the coefficient matrix that represents the contribution of the potential of a point of the heart to a point of the torso*;* D_{TT} is the coefficient matrix that represents the contribution of the potential of a point of the torso to a point of the torso*;* G_{HH} is the coefficient matrix representing the contribution of the voltage gradient of a point of the heart to a point of the heart; G_{HT} is the coefficient matrix representing the contribution of the voltage gradient of a point of the torso to a point of the heart; G_{TH} is the coefficient matrix representing the contribution of the voltage gradient of a point of the heart to a point of the torso; G_{TT} is the coefficient matrix representing the contribution of the voltage gradient of a point of the torso to a point of the torso; I_{N_X} is an identity matrix with the same number of columns and rows that nodes in the surface X (i.e. *Nx*).

The primary source if located only in the heart (atria and ventricles) and, consequently, Γ_T=0, resulting in the following matrix equation:

$$\begin{pmatrix} D_{HT} & D_{HH} \\ D_{TT} & D_{TH} \end{pmatrix} \cdot \begin{pmatrix} U_T \\ U_H \end{pmatrix} = -\begin{pmatrix} G_{HH} \\ G_{TH} \end{pmatrix} \Gamma_H \tag{48}$$

Grouping the previous matrix equation in two terms that depend on heart and torso parameters, respectively:

$$\begin{pmatrix} G_{HH} & D_{HH} \\ G_{TH} & D_{TH} \end{pmatrix} \cdot \begin{pmatrix} \Gamma_H \\ U_H \end{pmatrix} = -\begin{pmatrix} D_{HT} \\ D_{TT} \end{pmatrix} U_T \tag{49}$$

By operating with the equation system (49), we obtain that $\Gamma_H = -G_{HH}^{-1}(D_{HT}U_T + D_{HH}U_H)$ and we can finally solve the equation which gives the potential on the torso U_T through a transfer matrix heart-torso M and the potentials on the heart U_H [Geselowitz 1967, Sarvas 1987, Horácek 1997]:

$$U_T = MU_H \tag{50}$$

$$M = \left[D_{TT} - G_{TH}G_{HH}^{-1}D_{HT}\right]^{-1} \cdot \left[G_{TH}G_{HH}^{-1}D_{HH} - D_{TH}\right] \tag{51}$$

$$U_T = \left[D_{TT} - G_{TH}G_{HH}^{-1}D_{HT}\right]^{-1} \cdot \left[G_{TH}G_{HH}^{-1}D_{HH} - D_{TH}\right] \cdot U_H \tag{52}$$

3.1.1. Numerical computation of D (the solid angle Ω integral)

Using equation (52), the coefficient matrix D_{XY} is calculated as described in equation (53) for two different surfaces and as described in equation (54) for contributions from a surface to itself:

$$D_{XY} = \frac{1}{4\pi}\left[(\sigma_Y' - \sigma_Y'')\Omega_{XY}\right] \tag{53}$$

$$D_{XX} = \frac{1}{4\pi}\left[(\sigma_X' - \sigma_X'')\Omega_{XX}\right] + \left(\frac{\sigma_X' + \sigma_X''}{2}\right) I_{N_X} \tag{54}$$

where σ'_X y σ''_X are the conductivities in the inner and outer faces of the boundary surface *X;* σ'_Y and σ''_Y are the conductivities in the inner and outer

faces of the boundary surface *Y*, I_{N_X} is an identity matrix with the same number of columns and rows that nodes in the surface X (i.e. *Nx*); Ω_{XY} is the matrix of solid angles between surface *X* and surface *Y*:

$$\Omega_{XY} = \begin{pmatrix} \omega_{1,1} & \cdots & \omega_{1,N_Y} \\ \vdots & \ddots & \vdots \\ \omega_{N_X,1} & \cdots & \omega_{N_X,N_Y} \end{pmatrix} \tag{55}$$

Each component of matrix Ω_{XY}, $\omega_{i,j}$, is the solid angle subtended at the point *i* of surface *Y* by the area around point *j* of surface *X* and can be numerically calculated as the summation of the contributions of each triangular patch surrounding point *j* [De Munck 1992]:

$$\omega_{i,j} = \sum_{t=1}^{N_t} \omega_{i,j}^t \tag{56}$$

where $\omega_{i,j}^t$ is the estimation of the solid angle between the triangular patch *t* around the node *j* and the node *i* assuming a non-constant value of the potential inside the triangular patch, and N_t is the total number of triangular patches surrounding node *j*. Considering $\vec{y}_1$, $\vec{y}_2$ and $\vec{y}_3$ the vectors between the node *i* and the tree vertex of the triangle *t* and assuming that $\vec{y}_1$ connects the point *j* and the point *i*, $\omega_{i,j}^t$ can be calculated according to the linear interpolation over the triangles (see Figure 3.1) with the following expression [De Munck 1992]:

$$\omega_{i,j}^t = 2A^{-2}\left(\begin{array}{l} (\vec{y}_2 \times \vec{y}_3)\cdot(\vec{y}_2 \times \vec{y}_3 + \vec{y}_3 \times \vec{y}_1 + \vec{y}_1 \times \vec{y}_2)\omega'^t_{i,j} + \\ + \vec{y}_1 \cdot (\vec{y}_2 \times \vec{y}_3)(\vec{y}_2 - \vec{y}_1)\cdot \sum_{k=1}^{3} (\vec{y}_k - \vec{y}_{k+1})\gamma_k^0 \end{array} \right) \qquad \vec{y}_4 \equiv \vec{y}_1 \tag{57}$$

where A is the area of the triangle *t*; $\omega'^{t}_{i,j}$ is the solid angle of a patch when the potential is assumed as constant over the triangle and can be calculated as described in equation (58); and γ^{0}_{k} is a term calculated according to the equation (59):

$$\omega'^{t}_{i,j} = 2\arctan\frac{\vec{y}_1\cdot(\vec{y}_2\times\vec{y}_3)}{|\vec{y}_1|\|\vec{y}_2\|\vec{y}_3|+|\vec{y}_1|(\vec{y}_2\cdot\vec{y}_3)+|\vec{y}_3|(\vec{y}_1\cdot\vec{y}_2)+|\vec{y}_2|(\vec{y}_3\cdot\vec{y}_1)} \tag{58}$$

$$\gamma^{0}_{k} = \frac{-1}{|\vec{y}_{k+1}-\vec{y}_k|}\cdot\ln\frac{|\vec{y}_k\|\vec{y}_{k+1}-\vec{y}_k|+\vec{y}_k\cdot(\vec{y}_{k+1}-\vec{y}_k)}{|\vec{y}_{k+1}\|\vec{y}_{k+1}-\vec{y}_k|+\vec{y}_{k+1}\cdot(\vec{y}_{k+1}-\vec{y}_k)}$$

$$\vec{y}_4\equiv\vec{y}_1 \qquad \vec{y}_0\equiv\vec{y}_3 \tag{59}$$

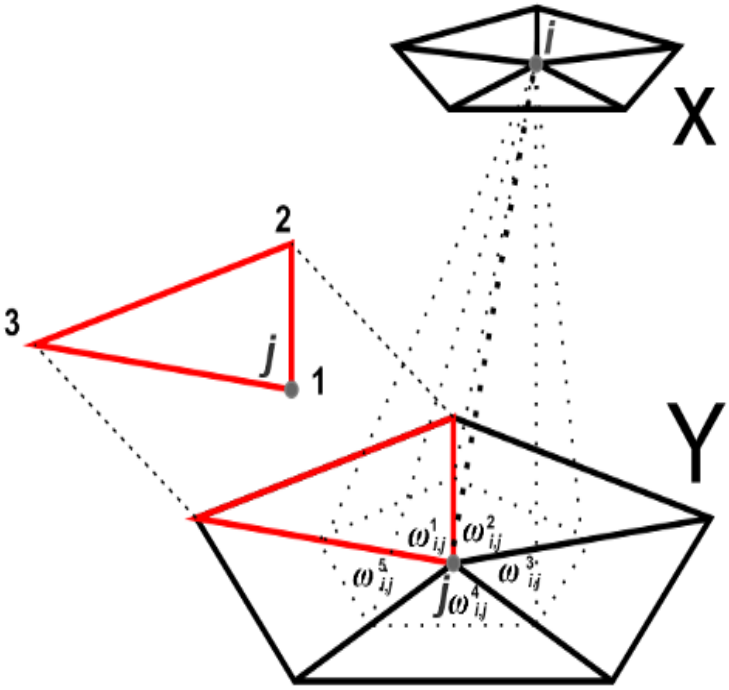

Figure 3.1: $\omega_{i,j}$ computation assuming a potential that varies linearly over each patch.

3.1.2. Numerical computation of *G* (the dS/r integral)

The coefficient matrix G_{XY} of equation (52) is calculated as described in equation (60) [Horácek 1997]:

$$G_{XY} = -\frac{1}{4\pi}\begin{pmatrix} \alpha_{1,1} & \cdots & \alpha_{1,N_Y} \\ \vdots & \ddots & \vdots \\ \alpha_{N_X,1} & \cdots & \alpha_{N_X,N_Y} \end{pmatrix} \tag{60}$$

$\alpha_{i,j}$ are coefficients that represent the contribution of the voltage gradient of the surface around point *j* of surface *X* in point *i* of surface *Y*; N_X and N_Y are the number of nodes of surfaces *X* and *Y* respectively. The numerical resolution of this contribution was calculated by using the Gaussian quadrature of seven points (see Figure 3.2) in each triangular patch around the point *j* [Stenroos 2008, Cowper 1972, Dunavant 1985]:

$$\alpha_{i,j} = \sum_{t=1}^{N_t} \alpha_{i,j}^{t} \tag{61}$$

$$\alpha_{i,j}^{t} = A\left[\sum_{n=0}^{6} \nu_n \left(\frac{\xi_n}{|\vec{q}_n|}\right)\right] \tag{62}$$

where N_t is the number of triangular patches surrounding node *j*; *A* is the area of the triangle; ν_n and ξ_n are the seven Gaussian quadrature weights corresponding to the different coordinate regions inside the triangle and $\vec{q}_n$ are the coordinates of each of these seven points referred to the observation point *i* [Dunavant 1985].

The Gaussian quadrature weights that we used are:

$$\xi_0 = 1/3 \tag{63.a}$$

$$\xi_1 = \frac{9-2\sqrt{15}}{21} \tag{63.b}$$

$$\xi_2 = \xi_3 = \frac{6+\sqrt{15}}{21} \tag{63.c}$$

$$\xi_5 = \xi_6 = \frac{6-\sqrt{15}}{21} \tag{63.d}$$

$$\xi_4 = \frac{9+2\sqrt{15}}{21} \tag{63.e}$$

$$v_0 = \frac{9}{40} \tag{63.f}$$

$$v_1 = v_2 = v_3 = \frac{\left(155+\sqrt{15}\right)}{1200} \tag{63.g}$$

$$v_4 = v_5 = v_6 = \frac{\left(155-\sqrt{15}\right)}{1200} \tag{63.h}$$

The $\vec{q}_n$ coordinates were calculated from vectors $\vec{y}_1$, $\vec{y}_2$ and $\vec{y}_3$ between node *i* and the tree vertices of the triangle *t* around the point *j* according to equations (64):

$$\vec{q}_0 = \frac{\vec{y}_1 + \vec{y}_2 + \vec{y}_3}{3} \tag{64.a}$$

$$\vec{q}_1 = \frac{9-2\sqrt{15}}{21}\vec{y}_1 + \frac{6-\sqrt{15}}{21}\left(\vec{y}_2 + \vec{y}_3\right) \tag{64.b}$$

$$\vec{q}_2 = \frac{9-2\sqrt{15}}{21}\vec{y}_2 + \frac{6-\sqrt{15}}{21}\left(\vec{y}_1 + \vec{y}_3\right) \tag{64.c}$$

$$\vec{q}_3 = \frac{9-2\sqrt{15}}{21}\vec{y}_3 + \frac{6-\sqrt{15}}{21}\left(\vec{y}_1 + \vec{y}_2\right) \tag{64.d}$$

$$\vec{q}_4 = \frac{9+2\sqrt{15}}{21}\vec{y}_1 + \frac{6+\sqrt{15}}{21}\left(\vec{y}_2 + \vec{y}_3\right) \tag{64.e}$$

$$\vec{q}_5 = \frac{9+2\sqrt{15}}{21}\vec{y}_2 + \frac{6+\sqrt{15}}{21}\left(\vec{y}_1 + \vec{y}_3\right) \tag{64.f}$$

$$\vec{q}_6 = \frac{9+2\sqrt{15}}{21}\vec{y}_3 + \frac{6+\sqrt{15}}{21}\left(\vec{y}_1 + \vec{y}_2\right) \tag{64.g}$$

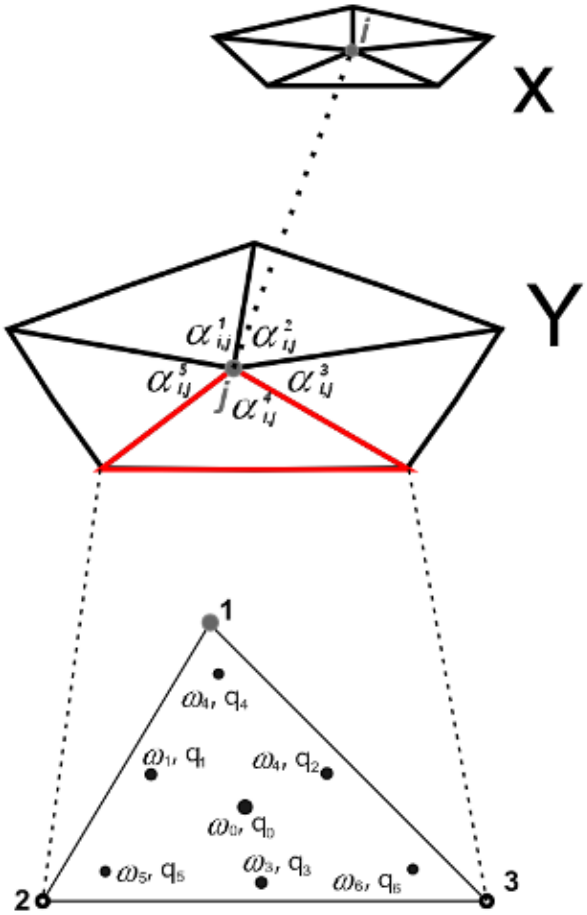

Figure 3.2: $\alpha_{i,j}$ computation considering an approximation of the integral with the Gauss Quadrature of order 5 (7 points). Dots locate the 7 Gaussian point, the size is proportional to the values.

3.2. The inverse problem resolution methodology

The regularization method used for solving the inverse problem of electrocardiography was the zero-order Tikhonov method (see equation (31)), and then B is the identity matrix.

The λ_{opt} regularization parameter, which allows the optimal inverse problem resolution, was selected with the L-Curve method. The optimal regularization parameter λ_{opt} corresponds to the first corner of the L which forms the curve, where it can be selected mathematically as the point at which the curvature $\kappa(\lambda)$ of the curve is maximum, corresponding point λ_{opt}. Equation (65) shows the curvature expression [Johnston 2000]:

$$\zeta(\lambda) = \log_{10}\left\|MU_H(\lambda) - U_T\right\|; \eta(\lambda) = \log_{10}\left\|BU_H\right\|$$
$$\kappa(\lambda) = \frac{\zeta'\eta'' - \zeta''\eta'}{\left[(\zeta')^2 + (\eta')^2\right]^{3/2}} \qquad (65)$$

where ζ', η' and ζ'', η'' denote the first and second derivatives of ζ and η with respect to λ.

A combined time-space regularization method was applied for the L-curve regularization parameter calculation [Greensite 2003], considering the torso and epicardial potential matrices for the different instants, instead of one single vector potential.

3.3. Validation with mathematical cellular model

Before processing the clinical data base with the implemented algorithms, they were validated in-silico with a realistic atria-torso model. Using mathematical models for researching has many advantages for validating experimental methods, against the in-vivo, ex-vivo or in-vitro techniques, allowing the complete control and monitoring of all physiological parameters, avoiding technical, economical or ethical issues. The active tissue of the atria used to validate the developed algorithms consisted of 577264 nodes that represent a realistic human morphology [Harrild 2000].

Electrophysiology of cardiac cells is typically modelled by the Hodgkin and Huxley differential equations formalisms, explaining the ionic mechanisms underlying the initiation and propagation of action potentials [Hodgkin 1952]. Hodgkin-Huxley model treats each component of an excitable cell as an electrical element including the ionic currents (I_{ion}), pumps (I_{pumps}) and exchangers (I_{exch}), the membrane capacity (C_m) and the externally applied current (I_{stim}). The transmembrane potential (V_m) can be computed with these electrical elements as showed in equation (66):

$$\frac{dV_m}{dt} = -\frac{I_{ion} + I_{stim} + I_{pumps} + I_{exch}}{C_m} \tag{66}$$

The action potential of each node was simulated by using a modified version of Courtemanche's mathematical model which includes the commented ionic currents, pumps and exchangers [Courtemanche 1998] in which $I_{K,Ach}$ current was introduced [Atienza 2006]. The cardiac tissue is described by monodomain equations, which assume that it behaves as an excitable medium, with diffusion and local excitation of the cellular membrane, according to:

$$\frac{dV_m}{dt} = \nabla\left(D\nabla V_m\right) - \frac{I_{total}}{C_m} \tag{67}$$

where I_{total} summarizes the contribution of all transmembrane currents, ∇ is the gradient operator, D is a diffusion tensor.

Atrial fibrillation in the realistic model was induced in-silico by a S1-S2 stimulation protocol. Mathematical computations were performed by using an adaptive time-step solver on a Graphical Processing Unit (NVIDIA Tesla C2075 6G) [García 2011, Garcia-Molla 2014]. Transmembrane potentials were computed for a simulation time of 4 seconds after stabilization of the model and were resampled to 1 kHz.

Simulated electrograms (EGMs) were computed by using transmembrane potentials according to equation (68) at 1 mm distance from the epicardial surface [Harrild 2000]:

$$EGM = \sum_{\vec{r}} \left(\frac{\vec{r}}{r^3} \right) \cdot \vec{\nabla} V_m \qquad (68)$$

where $\vec{r}$ is the distance vector between the measuring point and a point in the tissue domain, $\vec{\nabla}$ denotes the gradient operator, and V_m is the transmembrane potential.

For validating our methods by using as input the ECG generated by the mathematical model EGMs, body surface potential signals were computed on the outer surface from EGMs by solving the forward problem with the Boundary Element Method. Specifically, ECGs on a realistic torso model with 771 nodes and 1538 faces were estimated [MacLeod 1991].

4. An Iterative Method for Indirectly Solving the Inverse Problem of Electrocardiography

4.1. Introduction

The inverse problem of electrocardiography consists in the noninvasive determination of the electrical activity of the heart from measurements of potentials on the surface of the torso [MacLeod 1998, De Guise 1985]. There are two alternatives for solving the electrocardiographic inverse problem based on different formulations of the intra-cardiac sources: (1) a distribution of electrical potentials on the epicardial surface and (2) dipolar representations. Solutions based on the retrieval of the electrical activity on the surface of the epicardium have an ill-posed nature and high sensitivity to noise, leading to non-physiological solutions under low signal-to-noise ratios [De Guise 1985, Liu 2006]. Solutions based on the simplification of the electrical activity of the heart into a limited number of electrical dipoles may be less accurate than those based on the retrieval of potentials on the entire epicardial surface but more easily interpreted for physicians. Restrictions on the number of electrical dipoles to be retrieved allow for reasonable computing times and physiologically possible solutions.

Different approaches have been proposed for the solution of the inverse problem of electrocardiography in terms of electrical dipoles. The single moving dipole model [De Guise 1985] is the most straightforward approach but restricted to a representation of the electrical activity of the heart as a unique and spatially localized wavefront. A multipolar approach [Geselowitz 1960] is more realistic, but more noise sensitive and susceptible to crosstalk errors between different dipoles [De Guise 1985]. The two moving dipole model offers a compromise between accuracy and crosstalk effects, although is restricted to a dipolar representation of the electrical activity of the heart.

In this work the inverse problem of electrocardiography is solved by an alternative indirect method based on a multipolar representation of the heart electrical activity. Surface potentials generated by multiple dipoles are iteratively combined to maximize the similarity between computed and recorded potentials. The performance of the algorithm is tested by localizing electrical dipoles from simulated surface potentials in an eccentric spheres model of the human torso. Although this study focuses on the parametric analysis of the noninvasive computation of dipolar sources by using a high resolution spherical model, a feasibility study with a realistic torso model is introduced.

4.2. Methods

4.2.1. Approach for ECG inverse problem

The present approach for indirectly solving the ECG inverse problem is based on an iterative search for the combination of surface potentials generated by single dipoles which best describes the recorded surface potentials. Surface potentials produced by single dipoles at multiple sampled locations and linearly independent orientations (x,y,z) at each location are computed and stored by solving the forward problem with the boundary element method (BEM), constituting our surface potential database (SPDB). Potentials in the SPDB are iteratively combined and compared with the recorded potentials in terms of their relative difference measure (RDM*). The combination of single dipoles that generates a lower RDM* is selected, as depicted in Figure 4.1.

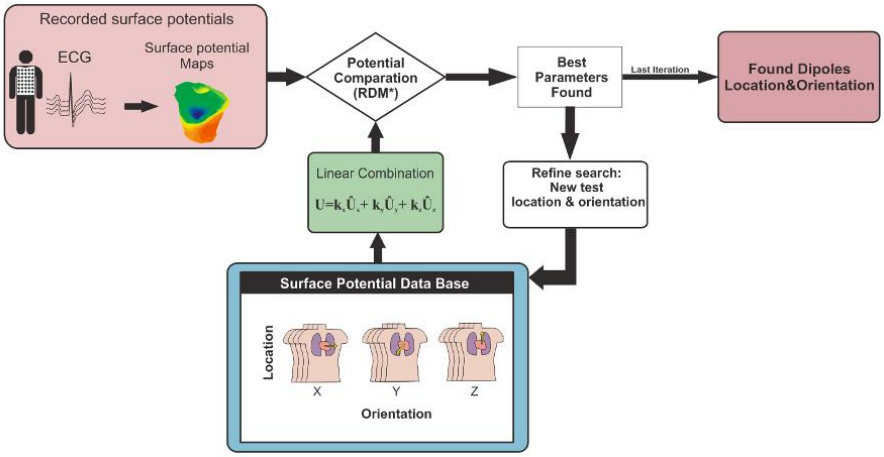

Figure 4.1: Methodology of the iterative method for solving the inverse problem with dipolar sources.

4.2.2. Potential database generation

This study focuses on the parametric analysis of the noninvasive computation of dipolar sources by using a high resolution spherical model. However, feasibility studies with this method were also performed with realistic torso models obtained by MRI image segmentation, presenting the same behaviour of the error, as shown in section 4.3.6 [Pedrón-Torrecilla 2010_b, Pedrón-Torrecilla 2010_c].

The torso model used to generate surface potentials (see Figure 4.2) was based on the eccentric spheres model proposed in the literature [Rudy 1979] with inner organs being modeled as spheres with homogeneous conductivities: blood σ_1=0.006

S/cm, heart muscle σ_2=0.002 S/cm, lungs σ_3=0.0005 S/cm, muscle σ_4=0.00125 S/cm, subcutaneous fat σ_5=0.0004 S/cm and external air σ_6=0 S/cm.

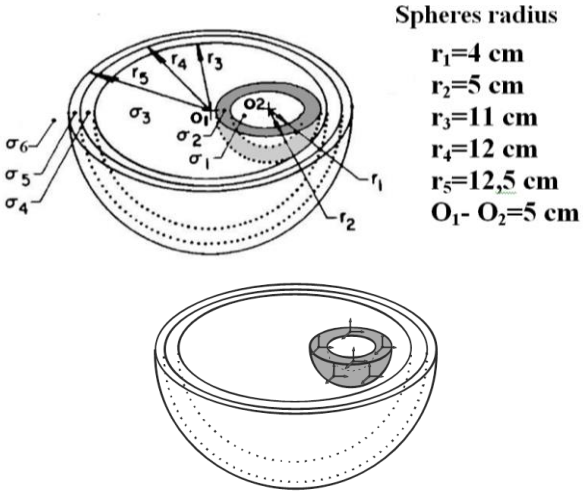

Figure 4.2: Spherical torso model employed [Rudy 1979]. The shaded volume conductor corresponds to the myocardium.

Surface potentials constituting the SPDB were computed by solving the forward problem on the surface of each sphere constituted by 162 nodes by means of the BEM for a set of electrical dipoles. Formulas related with the computation of the potentials on the torso surface by mean of dipolar sources are shown in Equations 10 and 37. Electrical dipoles with unitary amplitude and x, y or z orientation where located inside the myocardial spherical volume at N_r, N_θ and N_φ discrete positions equally spaced in r, θ and φ respectively in a coordinate system centered at O_2. (i.e. for N_r=3, N_θ=9 and N_φ=8 the SPDB is constituted by potentials generated by unitary dipoles at 216 locations and 3 orientations for each location). In this way, potential U generated on the torso surface by a single dipole with an arbitrary orientation and location $\vec{r}$, being $\vec{r}$ function of r, θ and φ, can be computed by a linear combination of the potentials generated on the torso by 3 linearly independent unitary dipoles (U_x, U_y, U_z) also located at $\vec{r}$, and then $U = k_x U_x + k_y U_y + k_z U_z$ (see Figure 4.1).

4.2.3. Iterative search algorithm

Potentials on the surface of the outer sphere generated by multiple dipoles can be computed as a linear combination of potentials generated by single dipoles. Electrical dipoles generating a given potential distribution (V, the test or recorded potential) could be estimated by choosing the linear combination of potentials generated by single unitary dipoles (U, the estimated potential) which results in a higher similarity of both potential distributions.

An exhaustive search, testing all possible combinations of dipoles at any position and with any orientation, requires high computation times which make this approach impractical. For this reason, we propose the use of an iterative algorithm for minimization of the dissimilarity of surface potentials. Dissimilarity of surface potentials was measured as their *RDM** value:

$$RDM^* = \sqrt{\frac{RDM^2 - (1 - MAG)^2}{MAG}} \tag{69}$$

where RDM and MAG are defined as [Meijs 1989]:

$$RDM = \sqrt{\frac{\sum (V - U)^2}{\sum V^2}} \qquad MAG = \sqrt{\frac{\sum U^2}{\sum V^2}} \tag{70}$$

For the first iteration only linear combinations of potentials generated by single dipoles at the center of the myocardial ($\vec{r} = (r_2 - r_1)/2$) wall are computed with steps in θ and φ equal to π/2 and possible weightings (k_x, k_y, k_z) equal to -1, 0 and 1. The combination with lower RDM* is chosen and thus an initial guess of the location (defined by r, θ and φ) and orientation (defined by k_x, k_y, k_z) for each searched dipole is obtained. Iteratively, search intervals in r, θ and φ are decreased and weighting coefficients ranging from -5 to 5 are applied to each unitary dipole. Weightings, and location of unitary dipoles that minimize RDM* for each searched dipole are chosen as the initial guess for subsequent iterations. As a consequence of the search strategy implemented, computing times will be dependent on the number of dipoles to be searched.

4.3. Results

4.3.1. Accuracy in single dipole location

Accuracy in the location of a single dipole is compromised by two factors: (1) selection of an iterative algorithm as opposed to an exhaustive search and (2) location of dipoles is not restricted to possible locations selected for the generation of the SPDB.

In order to quantify the errors introduced by the search strategy implemented, test potentials were obtained by solving the forward problem by BEM. A total of 1000 single dipoles at arbitrary locations among those stored in the SPDB (N_r=6, N_θ=17, N_φ=16) and with orientations among those that will be evaluated by the search algorithm were simulated. Surface potentials were used by the present iterative algorithm for the computation of the location and orientation of the

electrical dipole which best matches with simulated potentials. Errors in location (ε_D) and orientation (ε_O) for each simulation were computed.

Location of single dipoles was accomplished with no error in 85.8% simulations, whereas in the remaining cases the most proximal location possible was chosen. Estimation of location of single dipoles was accomplished with errors in location equal to 1.2±3.1 mm and errors in orientation equal to 4±11 º. Errors in orientation occurred for those dipoles whose location was not accurately determined and compensate for the error in location, resulting in low RDM* values.

4.3.2. Influence of SPDB resolution

Since indirect location of dipoles is restricted to the location of dipoles included in our database, the amount of dipoles that constitutes our database may have a great influence on the performance of the presented algorithm. In order to quantify the influence of the database resolution in the performance of the algorithm, surface potentials generated by a single dipole were obtained by forward BEM computation for 1000 different dipoles at arbitrary location and orientation within the myocardial wall. Location and orientation of dipoles generating such surface potentials were obtained by the present algorithm with 3 different database sizes: (1) Np=216 with N_r=3, N_θ=9, N_φ=8; (2) Np=1632 with N_r=6, N_θ=17, N_φ=16; (3) Np=11616 with N_r=11, N_θ=33, N_φ=32. Errors in location (ε_D) and orientation (ε_O) were computed. Also, the percentage of accurate dipole locations (ADL) was calculated as the percentage of dipoles located with errors under 10 mm.

Table 4.1 and Figure 4.3 shows the errors in dipole calculation for the three database resolutions tested. Notice that errors when dipole locations are not restricted to locations included in the SPDB are higher than those obtained when dipoles are located at positions included in the database for the same database size (5.4 mm vs. 1.2 mm). This error is due to the existent free space between the stored dipole locations in the SPDB and thus resulting locations are restricted to a subset of locations. In the best case, the algorithm will converge to the nearest r, θ, φ in the stored subset and thus, the larger the SPDB resolution, the smaller distance error is obtained. The distance error vs. percentage of occurrences presented a Rayleigh distribution, for the three database resolutions, centred on 8 mm, 5 mm and 3 mm distance error for SPDB resolutions 1, 2 and 3, respectively.

Table 4.1. Performance for different database resolutions

SPDB resolution	Np=216	Np=1632	Np=11616
ε_D (mean±SD)	9±5	5±3	4±2
ε_O (mean±SD)	29±21	18±15	14±12
ADL (%)	57.7	90.9	97.8

ε_D: location error (mm); ε_O:orientation error (º)

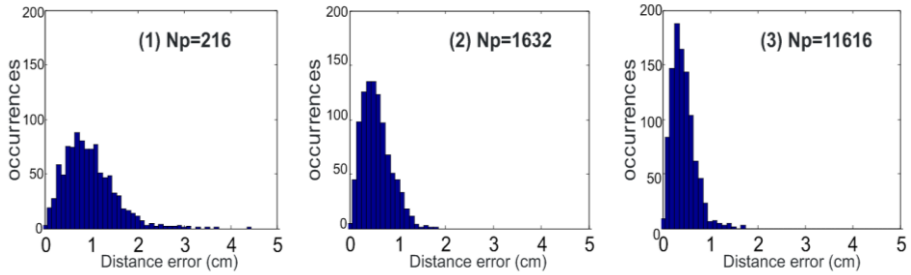

Figure 4.3: Influence of SPDB resolution.

4.3.3. Influence of noise

In order to evaluate the influence of noise in the accuracy of the present method, white noise was added to surface potentials before iteratively computing dipole locations. Surface potentials generated by 1000 simulations of single dipoles at arbitrary locations and orientations were contaminated with white noise with different signal-to-noise ratios (SNR): 20 dB, 10 dB, 6 dB and 3 dB. Surface potentials with added noise were used to estimate dipole locations with the present algorithm by using a constant SPDB size (Np=1632 with N_r=6, N_θ=17, N_φ=16).

Table 4.2 and Figure 4.4 show the performance of our method under the presence of noise. For SNR higher than 6 dB, mean location errors were found to be lower than 10 mm and more than 90% dipoles were accurately located. For a SNR equal to 3 dB 82% dipoles were accurately located.

Table 4.2. Performance under noise influence for a single dipole

SNR	20 dB	10 dB	6 dB	3 dB
ε_D (mean±SD)	5±3	5±4	6±6	8±9
ε_O (mean±SD)	18±15	18±16	19±17	20±18
ADL (%)	91.8	91.2	90.0	82.0

ε_D: location error (mm); ε_O:orientation error (^{o})

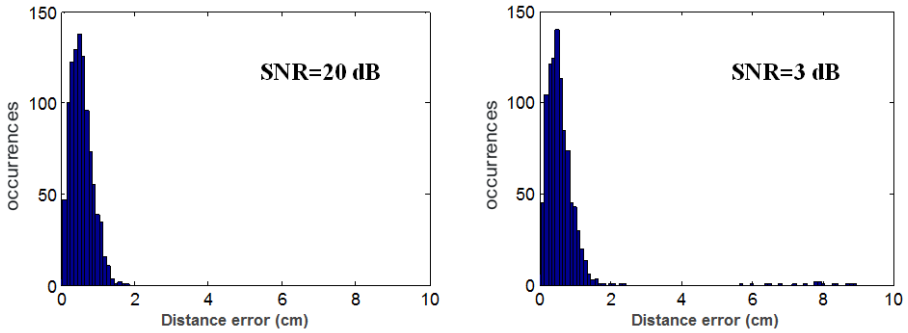

Figure 4.4: Influence of noise in a single dipole location. Distance error in inverse dipole location after noise addition with a SNR of 20 dB and 10 dB for a single dipole location.

4.3.4. Accuracy in double dipole location

Performance in the location of double dipoles was tested by locating two simultaneous dipoles inside the myocardial wall. A total of 1000 double-dipole configurations were tested by computing surface potentials by forward BEM, adding noise to surface potentials and iteratively search for the location and orientation of both dipoles by the presented method. Again SNR ratios equal to 20 dB, 10 dB, 6 dB and 3 dB were used and the same SPDB resolution used for previous simulations (Np=1632 with N_r=6, N_θ=17, N_φ=16). Mean errors in the location of the two simultaneous dipoles were computed.

Mean errors for double dipole location are shown in Table 4.3 and Figure 4.5. Mean errors exceed 10mm even for low noise added and do not increase significantly for higher SNR. Crosstalk error may have a greater influence on the performance of the algorithm than addition of noise.

Table 4.3. Performance for double dipole location

SNR	20 dB	10 dB	6 dB	3 dB
ε_D (mean±SD)	12±18	17±23	16±23	16±23
ε_O (mean±SD)	20±16	20±17	22±18	22±20
ADL (%)	77.5	72.0	72.0	72.0

ε_D: location error (mm); ε_O:orientation error (º)

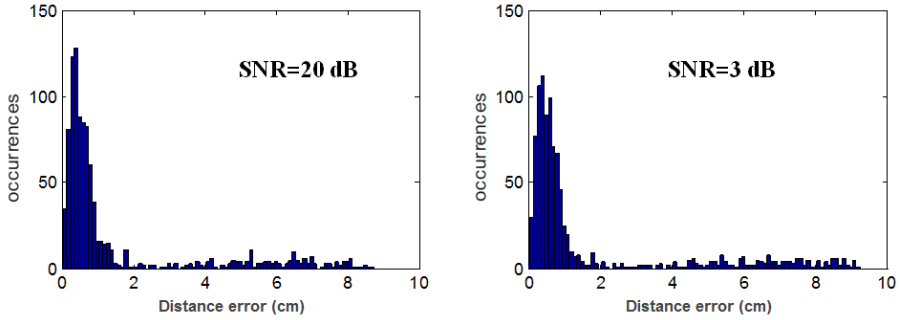

Figure 4.5: Influence of noise in double dipole location. Distance error in inverse dipole location after noise addition with a SNR of 20 dB and 10 dB for a double dipole location.

4.3.5. Computing time

Computing times were measured for the experiments described in sections 3.2 and 3.4 and compared to those required for an exhaustive search strategy. The processor used was an Intel Core2Duo-P8400, 2.26 Ghz and 4GB RAM. Times required for an exhaustive search increase exponentially with SPDB resolution. Required computing times are greatly reduced by using an iterative search strategy, reduction more pronounced for large SPDB resolution (Table 4.4). Computing time is also dependent on the number of searched dipoles, increasing from 0.35s for localizing a single dipole for a medium SPDB size (Np=1632) to 91±18 s for a double dipole search and the same SPDB size. This computing time greatly reduces the required time for an exhaustive search ($8 \cdot 10^8$ s).

Table 4.4. Computing times in seconds for the iterative and exhaustive search algorithms for a single dipole location

SPDB resolution	Np=216	Np=1632	Np=11616
Exhaustive search	48 s	369 s	2628 s
Iterative search (mean ± SD)	0.26±0.02 s	0.35±0.03 s	1.86±0.27 s

4.3.6. Study with a realistic torso model

A parametric study of the iterative method was explained in previous sections in a spherical model. A feasibility study was also performed with a realistic torso model [MacLeod 1991, Cerqueira 2002], presenting the same behaviour of the error [Pedrón-Torrecilla 2010_b, Pedrón-Torrecilla 2010_c].

In this case, the SPDB resolution was lower than with the spherical model, having a maximum of 23 possible locations homogeneously distributed in the myocardium [Cerqueira 2002], as depicted in Figure 4.6. The maximum distance between two regions of the segmented myocardium and therefore, between two possible locations of the dipoles stored in the SPDB, is $SPDB_D$=2.6 cm. Although the SPDB resolution is lower, the main purpose in clinical practice is to know the patterns of activation of the different myocardial regions and then, a small resolution of the SPDB would be enough to identify diseases with a simple propagation pattern.

In this case, the ADL was considered as the percentage of dipoles located with errors under the $SPDB_D$.

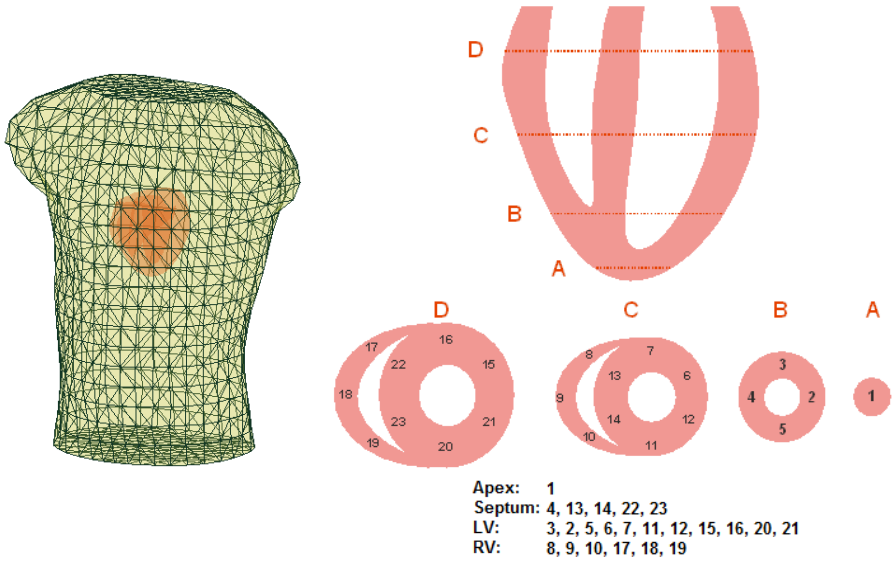

Figure 4.6: Torso model and segmentation of the ventricular myocardium in 23 regions [MacLeod 1991, Cerqueira 2002]. The 23 regions are 23 possible locations of the dipoles stored in the SPDB.

As it is shown in Figure 4.7 and Table 4.5, for a single dipole location, an error of 1.49 cm and 1.54 cm was obtained for a SNR of 20 and 3 dB, respectively. On the other hand, as it is shown in Figure 4.7 and Table 4.6, for double dipoles location, an error of 2.03 cm and 2.11 cm was obtained for a SNR of 20 and 3 dB, respectively. For the realistic model, the algorithm located accurately 95% of simple dipoles for a SNR of 3 dB, showing a similar performance for different SNRs. However, in the case of two simultaneous dipoles about 73% of the dipoles were accurately located, independently of the SNR, showing a greater influence to crosstalk noise.

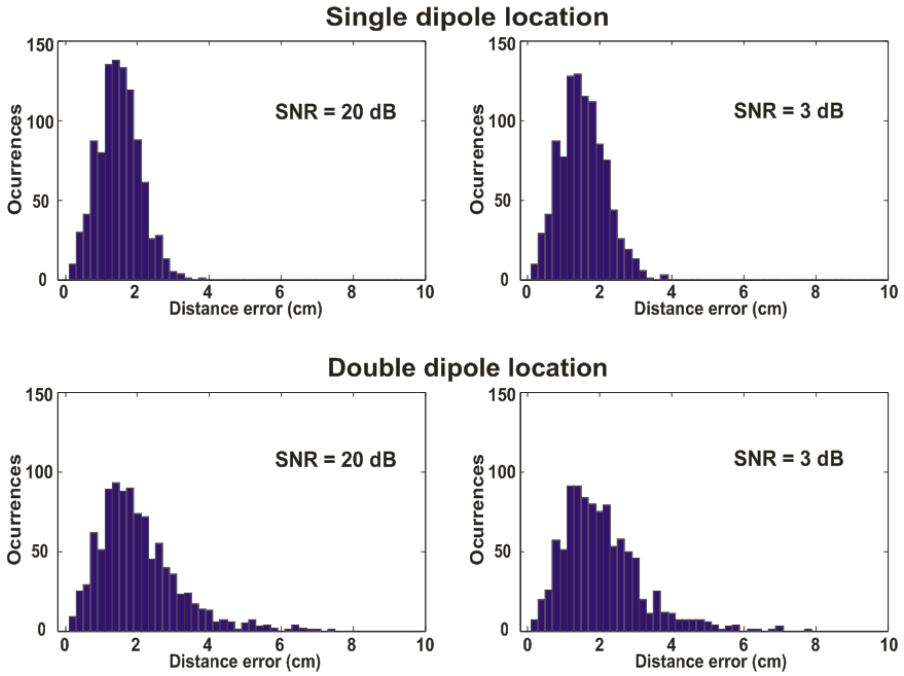

Figure 4.7: Influence of noise in dipole location in a realistic torso model. Distance error in inverse dipole location after noise addition with a SNR of 20 dB and 10 dB for simple and double dipole location.

Table 4.5. Performance for a single dipole location in a realistic torso

SNR	20 dB	10 dB	6 dB	3 dB
ε_D (mean±SD)	1.49±0.57	1.49±0.57	1.50±0.58	1.54±0.62
ε_O (mean±SD)	8±6	8±6	8±6	8±6
[ε_D < $SPDB_D$=2.6] (%)	96.3	96.2	96.1	95.0

ε_D: location error (cm); ε_O:orientation error (º)

Table 4.6. Performance for double dipole location in a realistic torso

SNR	20 dB	10 dB	6 dB	3 dB
ε_D (mean±SD)	2.03±1.13	2.05±1.15	2.08±1.18	2.11±1.17
ε_O (mean±SD)	26±20	26±20	26±20	27±20
[ε_D < $SPDB_D$=2.6] (%)	75.3	74.7	74.2	72.9

ε_D: location error (cm); ε_O:orientation error (º)

4.4. Discussion

We have shown that the inverse problem in electrocardiography can be solved indirectly by comparing the recorded surface potentials with stored surface potentials generated by known sources. The accuracy in this indirect method will be dependent on the amount of surface potentials stored for comparison which limits the spatial resolution of the algorithm to the spatial resolution used for the construction of the database.

Although an exhaustive search of all combinations of stored potentials for solving the inverse problem is possible, the computing time of this approach is excessive. An iterative algorithm has been proposed as a more time-efficient approach, and tested on a database of simulated potentials computed for an eccentric spheres model.

The present method has shown to be accurate in the localization of single dipoles with intermediate database resolutions (1632 locations) even under the presence of considerable amounts of noise. However, accuracy of the iterative search strategy presented has shown to be inferior to that of the exhaustive search algorithm because the best match may not always be tested.

Limitations of the iterative search strategy presented are more evident when two simultaneous dipoles are searched. Accuracy in the presence of two simultaneous dipoles is notably reduced mainly due to crosstalk, which compromises the performance of the method to a higher extent than the presence of noise. The performance of the algorithm could be improved if search intervals for each parameter were not fixed and adapted to RMD* gradient, allowing larger search intervals until a moderate RMD* value is achieved.

The present method for indirectly solving the inverse problem of electrocardiography has been tested for an eccentric spheres model, taking advantage of the ease of a high resolution SPDB generation and the parametric analysis computing. The same methodology could be used for realistic torso models obtained by MRI or CAT image segmentation, as presented in feasibility studies, showing similar performance as with spherical models. Also, it has been tested for searching up to two dipoles, but could be applied for searching a reduced number of dipoles, although the computing time will increase with the number of searched dipoles. In order to reduce computing times, initial conditions could be introduced into the model. For solving the inverse problem in electrocardiography during a ventricular activation, the use of the solution obtained for a preceding time instant could serve as an initial condition and thus speed up calculations.

4.5. Conclusion

A new iterative algorithm, based on comparison of stored surface potentials to recorded potentials was implemented and tested, solving the inverse problem for simple propagation patterns, showing accurate results even under noise conditions.

5. Characteristics of inverse-computed epicardial electrograms of Brugada syndrome patients

5.1. Introduction

Brugada syndrome (BrS) is a heritable arrhythmia syndrome that causes sudden death in young adults with structurally normal heart [Antzelevitch 2005_a]. BrS is diagnosed on the basis of the clinical and family history of the patient and a characteristic ECG pattern displaying a coved-type ST segment $\geq$ 0.2 mV (2 mm) in right precordial leads (referred as type I ECG) [Brugada 1992]. However, the clinical manifestation is often dynamic and shows variations over time, including transient normalization of the ST segment and conversion to a saddleback-type pattern [Antzelevitch 2005_a]. Specifically, BrS patients present spontaneous type I ECGs or a saddleback-type ECG with similar probability during follow-up but about half of their ECGs may not present any abnormality [Richter 2009]. Although saddleback-type ST segments are linked to BrS since they are usually found in this group of patients, they are not considered as diagnostic unless converted to a type I ECG after administration of ajmaline or flecainide [Antzelevitch 2005_b].

Experimental studies have demonstrated that heterogeneity and conduction delay within the epicardium of the right ventricular output tract (RVOT) contribute to the ECG characteristics observed in BrS patients [Berruezo 2004], [Morita 2008]. However, the contribution of depolarization and repolarization abnormalities in the genesis of the surface ECG is still a matter of debate [Wilde 2010]: while some groups believe that a depolarization delay in the RVOT is the main cause of the observed ECG in BrS [Morita 2010], [Postema 2008] other groups support the hypothesis that it may be caused by transmural heterogeneities in the shape of action potentials in the RVOT region [Morita 2009], [Nademanee 2011]. Although these hypotheses are not completely exclusive they may be of importance to determine the prevalent mechanism in BrS patients in order to develop diagnostic tools which may increase the sensitivity in the diagnosis of the syndrome.

Analysis of the electrical activity by recording epicardial or endocardial electrograms (EGM) is a valuable tool for the understanding of this pathological condition. In fact, EGMs recorded in the RVOT have revealed that the electrical activation in this region is delayed and discontinuous, which is reflected in delayed and fractionated EGMs [Lambiasee 2009]. However, recording of EGMs is an invasive procedure only performed in patients already diagnosed with the syndrome. In this study, we computed EGMs from noninvasive recordings by solving the

inverse problem of electrocardiography in BrS patients. Inverse-computed EGMs of BrS patients were compared to those of control subjects in terms of their activation times and duration.

5.2. Methods

5.2.1. Patient Population

In this study, 6 patients diagnosed with BrS and 6 control subjects were included. The clinical diagnosis of BrS was established prior to our study and was based on the presence of a coved-type S-segment elevation ≥ 0.2 mV in two right precordial leads either spontaneously or after ajmaline or flecainide administration. Selected normal subjects had no history of previous heart disease and a normal resting ECG.

5.2.2. BSPM recording

A total of 64 chest and back leads were acquired simultaneously for each subject in addition to the standard limb leads for 2 minutes. Electrodes were mounted on an adjustable vest [Guillem 2010] at locations depicted in Figure 5.1. Signals were acquired at a sampling rate of 2048 Hz, with a resolution of 1 μV and a bandwidth of 500 Hz. Before acquisition, signal quality of all leads was visually inspected and ECG recordings were stored for off-line processing.

Standard ECG leads were computed from BSPM leads recorded at positions more similar to the standard ECG leads (see Figure 5.1).

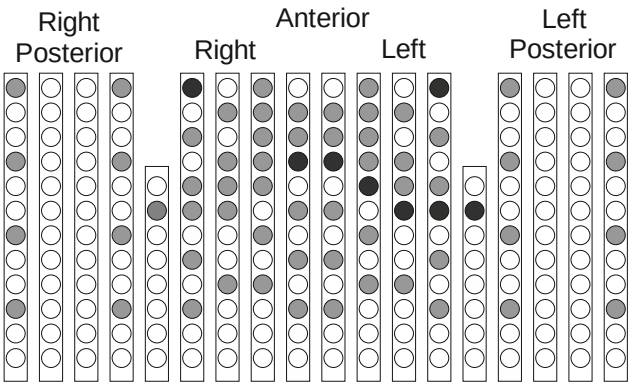

Figure 5.1: Electrode positions in our BSPM system for the recording of the Brugada syndrome. Black circles correspond to the approximate location of precordial, right and left arm leads.

5.2.3. ECG signal processing

ECG signals were processed using Matlab 7.10.0 (The Mathworks Inc, The Netherlands). First, the baseline was estimated by filtering with a butterworth 10th order low-pass filter with a cut-off frequency of 0.6 Hz after decimation to a sampling frequency of 51.2 Hz. Baseline was interpolated to 2048 Hz and subtracted to the original recording. Then, ECG signals were filtered with a 10th order, low-pass Butterworth filter with a cut-off frequency of 70 Hz. Power spectral density of all signals was computed by using a Welch periodogram with a hamming window of 8 seconds and 50% overlap. Leads presenting more than 0.5% of their spectral content at 50Hz were filtered with a 2nd order IIR notch filter centered at 50 Hz. All leads were visually inspected after filtering and leads with noticeable noise or very low amplitude were excluded from further analysis.

QRS complexes were detected by selection of local maxima after steeper slopes in a simplified ECG obtained by polyline splitting [Jain 1995]. Then, averaged PQRST complexes were obtained by template matching-averaging 120 seconds of the recordings. Fiducial points in averaged beats were detected by selecting points preceding or following segments with steeper slopes in a simplified beat obtained by polyline splitting. Fiducial point detection was then manually verified. P_{onset} and T_{offset} served as anchoring points for baseline estimation on the averaged beats and the remaining baseline was subtracted.

5.2.4. EGM measurements

Computed epicardial electrograms (EGMs) were analyzed in terms of their activation times and the duration of the QRS complex. Activation times were computed as those instants with a maximum –dV/dt. Activation time was defined as the difference between each activation time and the earliest. Duration of QRS complexes was measured by an experienced observer on the EGM tracings.

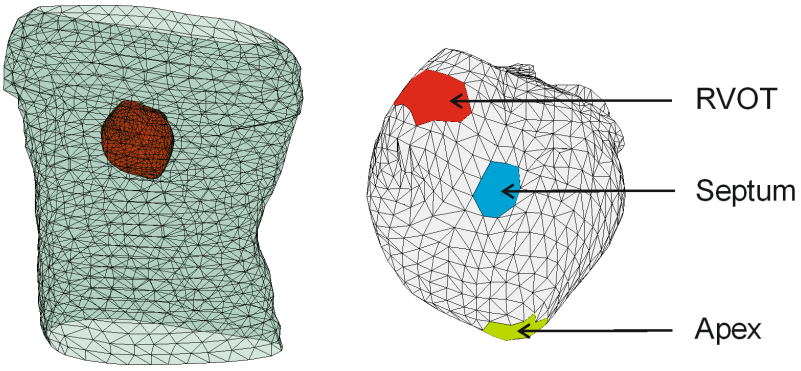

Figure 5.2: Heart and torso model used and studied epicardial regions.

5.2.5. Statistical analysis

Activation delays and durations of BrS patients and controls were compared for different regions of the heart. EGMs from septum, apex and RVOT region were analyzed (see Figure 5.2) and values were given as mean ± std. Differences in measurements between BrS patients and controls were evaluated in each heart region by using an unpaired Student's t test. A *p* value lower than 0.01 was considered significant.

5.3. Results

Type I ECGs were found in the computed standard twelve-lead ECG in 3 patients (BrS-I) at the time of the BSPM recording, while 3 patients presented a non-type I ECG (BrS-nI). Computed electrograms of three subjects (control, BrS-I and BrS-nI) are depicted in Figure 5.3. EGMs at the RVOT region were noticeably longer and more fractionated in BrS patients as compared to controls both for BrS-I and BrS-nI groups. EGMs computed for other regions of the epicardium presented less fractionation and shorter QRS complexes.

As depicted in Figure 5.3, computed activation times were consistent with experimental observations, with a first depolarization of the septum, followed by the apex and a later depolarization of the RVOT, both for controls and BrS patients.

Differences in activation times between controls and BrS patients for septum (15 ± 2 vs. 17 ± 3 ms) and apex (31 ± 2 vs. 33 ± 4 ms) were not significant. However, activation delay in the RVOT region in controls vs. BrS patients differed significantly: 39 ± 5 vs. 58 ± 7 ms ($p<0.01$).

Duration of QRS complexes in the EGMs of controls vs. BrS patients did not differ significantly for septum (84 ± 13 vs. 91 ± 17 ms) or apex (79 ± 6 vs. 88 ± 10 ms), as it can be observed in Figure 5.4. EGMs at the RVOT region of controls were significantly shorter than those of BrS patients: 85 ± 8 vs. 122 ± 22 ms ($p<0.01$).

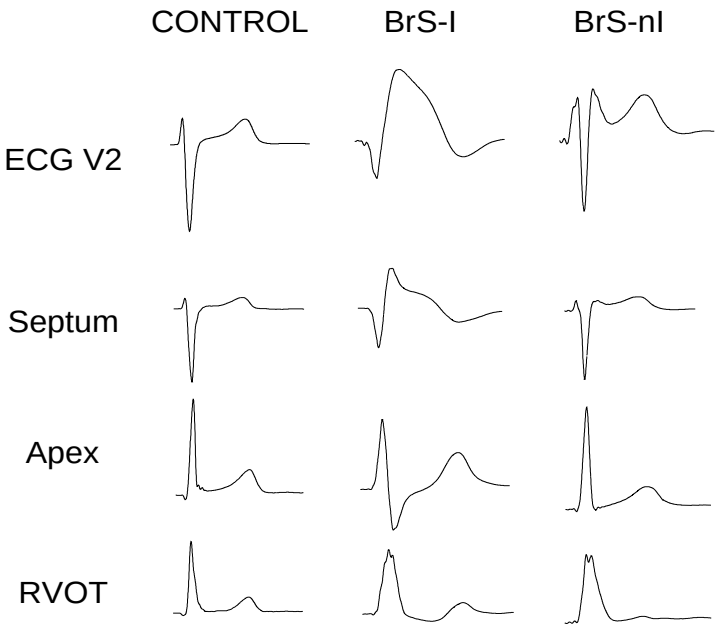

Figure 5.3: Electrocardiograms and computed electrograms of controls and BrS patients from septum, apex and RVOT.

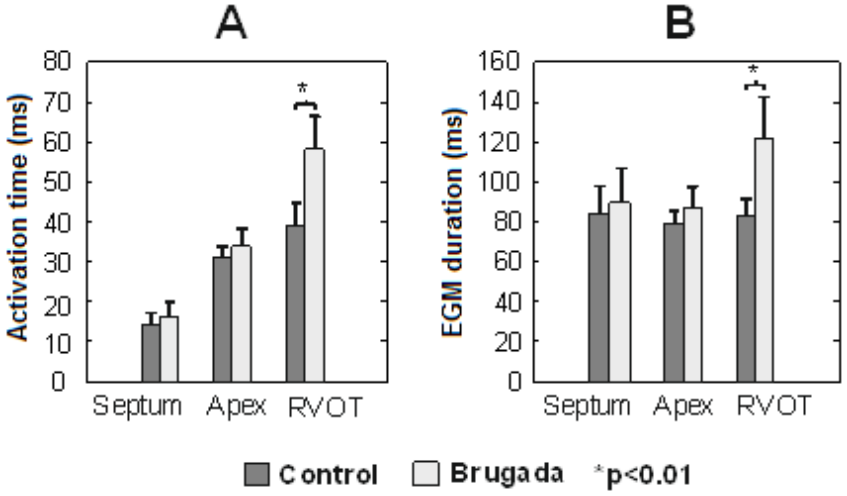

Figure 5.4: Duration and activation times of EGMs in controls and BrS patients from septum, apex and RVOT.

5.4. Discussion

5.4.1. Main findings

In this research, we have obtained epicardial electrograms of controls and BrS patients by solving the inverse problem of electrocardiography. Inverse-computed EGMs of BrS patients have shown a delayed activation of the RVOT and long and fractionated EGMs in the same region. EGMs obtained for other regions of the epicardial surface did not present durations and/or activation times that differed from those obtained for control subjects.

5.4.2. Comparison with previous studies

Diagnosis of BrS patients based on the standard ECG lacks sensitivity due to the dynamic nature of ST elevation. However, analysis of BSPM maps has shown that QRS complexes of BrS patients present specific characteristics that may allow the identification of these patients even in the absence of a type I ECG [Guillem 2010]. Analysis of the inverse-computed electrograms of BrS patients has shown an abnormal activation in the RVOT and this suggests that this region may be involved in these non-transient specific characteristics observed in BSPM maps of BrS patients.

Characteristics of our inverse-computed EGMs are consistent with experimental results in human healthy subjects, reflecting the expected sequence of activation and EGMs of similar duration all over the epicardium. More importantly, computed EGMs of BrS patients are also consistent with recent electrophysiological studies [Antzelevitch 2005_a, Lambiase 2009], reflecting delayed and fractionated activations in the RVOT region.

5.4.3. Limitations and future work

Although our findings are consistent with those presented in the literature, we do not have simultaneous recordings of EGMs and BSPMs which may be useful for validating our computed EGMs.

Our results suggest that inverse-computed EGMs may help in diagnosing BrS. However, a larger population of BrS patients, controls and patients with other electrophysiological disorders should be included in our study in order to elucidate the sensitivity and specificity of the EGM measurements that can be obtained.

The same torso model was used for all the patients in our study. Although variations in shape do influence the computed EGMs and thus customized torso models may allow a more accurate calculation of EGMs it may not feasible to obtain customized torso models for a large population of BrS patients. However, we believe that the proposed methodology allows comparison of the computed EGMs among different groups of patients.

5.5. Conclusion

Inverse-computed EGMs of BrS patients show activation abnormalities in the RVOT region, consistent with experimental observations. Analysis of EGMs morphologies computed by solving the inverse problem of electrocardiography in terms of myocardial potentials appears as a promising tool in the noninvasive diagnosis of the Brugada syndrome.

6. Noninvasive estimation of the activation sequence in the atria during sinus rhythm and atrial tachyarrhythmia

6.1. Introduction

Atrial arrhythmias are great of concern in clinical electrocardiology. Atrial fibrillation (AF) and other arrhythmias have a great clinical impact in morbidity and mortality in developed countries [Fuster 2006, Calkins 2007]. These arrhythmias can be maintained by a small tissue area [Haïssaguerre 1998] and, therefore, ablation procedures have become one of the most efficient treatments since isolation of these regions usually results in termination the arrhythmia.

In the clinical settings, identification of ablation targets is achieved by electroanatomical mapping. Nowadays, electroanatomical mapping is the most common used technique in clinical practice. This technique can be only used to detect stable foci in the atria or to characterize a re-entrant pattern during atrial flutter, however, location of atrial sources during AF is more complicated since contact mapping is performed sequentially and it is not possible to acquire a long time recording in multiple points of the atria under a non-stationary activation. A noninvasive reconstruction of the atrial activation sequence based on the recording of multiple simultaneous ECGs may overcome this limitation. Furthermore, the prior knowledge of source location may help ablation planning and reducing the procedure time.

The aim of this study is to evaluate the noninvasive electrocardiographic imaging technique as a clinical tool for the identification of the origin of atrial tachycardias and during sinus rhythm, focusing the study in both stationary propagation patterns. Real body surface potential mapping recordings were used to reconstruct the epicardial activity in the atria. Results were validated by using simultaneous intracardiac recordings.

6.2. Methods

Methodology section describes the clinical case study used to illustrate the performance of the technique.

6.2.1. Clinical case study

The included case study was a patient admitted for ablation of drug-refractory paroxysmal atrial fibrillation. The subject was in sinus rhythm at the beginning of the intervention. During the electrophysiological study, 15 bipolar EGMs and a 64-channel BSPM recording were registered simultaneously (see Figure 6.1). In order to illustrate the presented methodology recordings during two propagation patterns are used; (1) during sinus rhythm (SR) and (2) during an atrial tachycardia generated by pacing from the left superior pulmonary vein (LSPV).

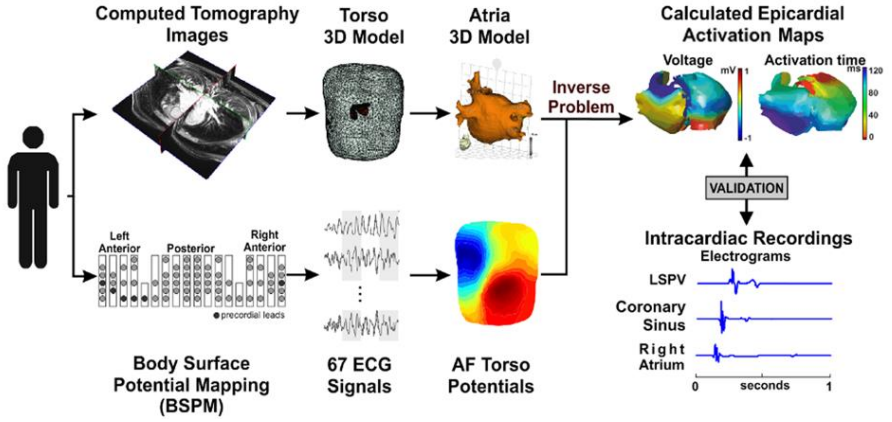

Figure 6.1: Methods for the noninvasive reconstruction of the activation maps for sinus rhythm atrial tachyarrhythmia.

Prior to the ablation procedure, computer axial tomography (CAT) images with a spatial resolution of 0.5 mm were acquired to build the 3D atrial and torso models (see Figure 6.1) and segmented by using 3D Slicer [Feodov 2012]. Specifically, heart and torso conductive volumes were segmented from CAT images and isotropic and homogeneous conductivities of 0.6 S/m and 0.2 S/m respectively. Both surfaces were tessellated into flat triangles, using 3615 nodes and 7222 faces for the atrial surface and 2689 nodes and 5374 faces for the torso surface.

During the entire ablation procedure, patients wore a custom-made adjustable vest with 64 electrodes covering the entire torso surface (Figure 6.2) plus 3 electrodes used for recording the limb leads. The vest included recording electrodes in the anterior (N=28), posterior (N=34) and lateral sides (N=2) of the torso. Signals were acquired at a sampling rate of 2048 Hz, with a resolution of 1 μV and a bandwidth of 500 Hz. Before acquisition, signal quality of all leads was visually inspected and ECGs were stored for off-line processing [Guillem 2009]. Additionally, 15 bipolar EGMs were simultaneously recorded by using a standard tetrapolar catheter in the right atrial (RA) appendage; 2) a deflectable 4 mm mapping catheter (Marinr, Medtronic Inc., Minneapolis, USA) in the distal coronary sinus (CS); 3) a decapolar

circular mapping Lasso catheter (Biosense-Webster, Diamond Bar, CA, USA) used to map the left superior pulmonary vein (LSPV); and 4) a Navistar catheter (3.5 mm tip, 2-5-2 interelectrode distance, Thermo-Cool, Biosense-Webster, Diamond Bar, CA, USA) used to stimulate. EGM signals were acquired at a sampling rate of 977 Hz, with a resolution of 1 μV.

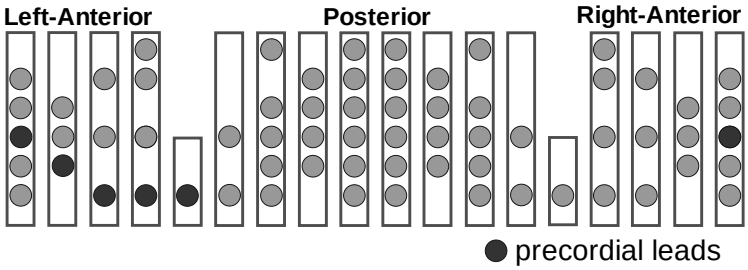

Figure 6.2: Electrode position in our BSPM system for recording atrial signals. Black circles correspond to the approximate location of precordial, right and left arm leads.

ECG signals were processed using Matlab 2010 (The Mathworks Inc, The Netherlands). First, the baseline was estimated by filtering with a butterworth 10th order low-pass filter with a cut-off frequency of 0.8 Hz after decimation to a sampling frequency of 51.2 Hz. Baseline was interpolated to 2048 Hz and subtracted to the original recording. Then, ECG signals were filtered with a 10th order, low-pass Butterworth filter with a cut-off frequency of 70 Hz. Power spectral density of all signals was computed by using a Welch periodogram with a Hamming window of 8 seconds and 50% overlap. Leads presenting more than 0.5% of their spectral content at 50 Hz were filtered with a 2nd order IIR notch filter centered at 50 Hz. All leads were visually inspected after filtering and leads with noticeable noise or very low amplitude were excluded from further analysis.

Two representative P-waves were used for noninvasive estimation of intracardial electrograms by using the methodology described above (i.e. one during sinus rhythm and one during LSPV stimulation). The reconstructed atrial propagation pattern was compared with the 15 simultaneously recorded intracardiac catheter signals, quantifying the difference between the maximum and minimum of the myocardial activation time and the inverse-computed activation error in ms. Accuracy of reconstructed EGMs was quantified by measuring the relative error between normalized voltage of the modelled EGMs and inverse computed EGMs (icEGMs).

6.3. Results

6.3.1. Mathematical model validation

In order to validate the noninvasive imaging method and algorithms implemented for the isochrone map reconstruction, mathematical model was performed, as described in section 3.3, for a sinus rhythm propagation pattern by applying a 5 ms stimulus from the region of the sinus node.

In Figure 6.3.A, the isochronal map of the reconstructed activation sequence from the simulated data is depicted. The solution of the inverse problem showed an activation sequence starting at the sinus node that propagates to the right and left atria across the Bachmann's bundle. In Figure 6.3.B three EGMs from the RA, CS and LSPV are depicted which are consistent with the reconstructed activation sequence. Difference between the activation times in atria and those computed after inverse problem solution was 2.19 ± 10.58 ms. Relative error between the modeled EGMs and icEGM voltages during sinus rhythm was 9.2 ± 4.8 %.

6.3.2. Clinical case study

The reconstruction of the epicardial activation sequence during sinus rhythm allowed the identification of a propagation pattern from the right to the left atrium (Figure 6.4.A). Recorded EGMs were consistent with the computed activation sequence: the activation can be first observed in the RA catheter, followed by the CS and the LSPV (Figure 6.4.B). EGMs showed a difference between the activation of the RA and LSPV of 93 ms. Noninvasively computed activation times of the RA and the LA showed a maximum time difference of 102 ms.

When the LSPV was paced, EGMs showed an earlier activation in the LSPV followed by an activation in the CS and a final activation of the RA (Figure 6.4.D). The difference in the activation time between LSPV and RA EGMs was 49 ms. Inverse reconstruction of the epicardial propagation pattern showed one wavefront starting at the LSPV (Figure 6.4.C) and a depolarization of the most distal part of the RA taking place 71 ms after the stimulation.

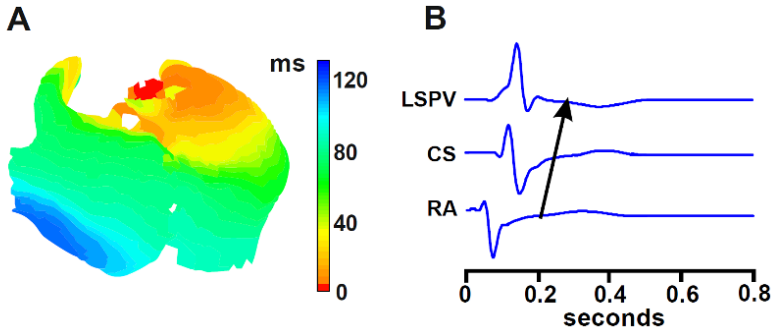

Figure 6.3: Reconstructed activation sequence and simulated EGMs. *(A)* Activation sequence obtained by solving the inverse problem in the mathematical model during sinus rhythm. *(B)* Simulated unipolar EGMs obtained at the left superior pulmonary vein (LSPV), coronary sinus (CS) and right atrium (RA).

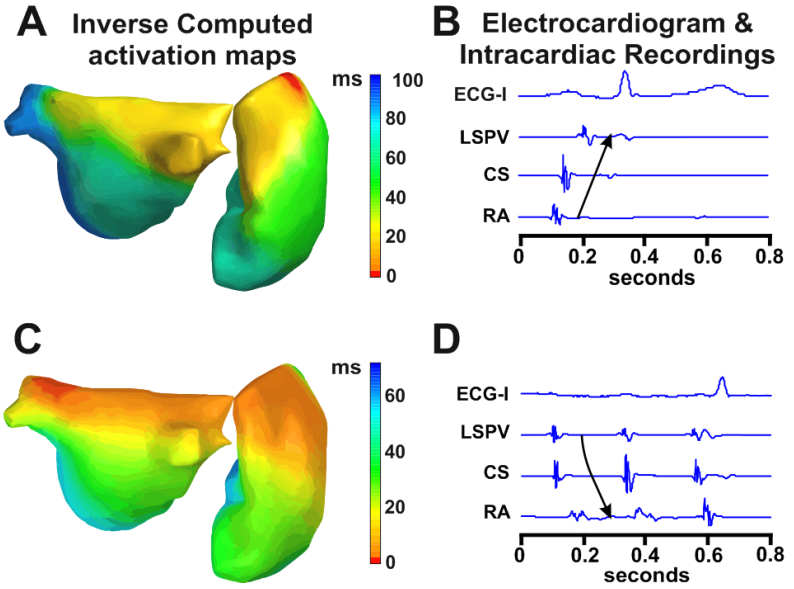

Figure 6.4: Noninvasive reconstruction of the isochrones maps during sinus and atrial tachyarrithmia. *(A)* Noninvasive reconstruction of activation sequences during sinus rhythm and *(C)* left atrial stimulation. *(B, D)* Lead I on the standard ECG and bipolar EGMs from the left superior pulmonary vein (LSPV), coronary sinus (CS) and right atrium (RA).

6.4. Discussion

In the present study, noninvasive recordings and the solution of the inverse problem of electrocardiography were used to estimate the epicardial activation sequence from a patient under sinus rhythm and atrial tachycardia generated by pacing at the left superior pulmonary vein. Experimental results were consistent with simultaneously recorded intracardiac EGMs and measured and inverse-computed activation times were comparable.

In addition, mathematical simulations were used to quantify the accuracy of reconstructed activation sequences. The origin of electrical activation could be determined within a few mm and activation times were reconstructed with an almost negligible error. By using this detailed ionic model of the atria, different clinical scenarios could be simulated (i.e. sinus rhythm, atrial tachycardia, atrial flutter or atrial fibrillation) and used to evaluate the accuracy of the inverse problem solution to estimate more complex propagation patterns and to clarify the relation between epicardial propagation patterns and its representation on the torso [Guillem 2009].

The methods described in this work may be useful for planning an ablation procedure. During the last years, different groups have developed and tested the methodology to noninvasively reconstruct the epicardial activation sequence during atrial tachycardias [Ramanathan 2004, Roten 2012], atrial flutter [Wang 2007] and atrial fibrillation [Cuculich 2010]. Although cardiac mapping can be used to detect stable foci in the atria or to characterize a re-entrant pattern during atrial flutter, location of atrial sources during fibrillation is more complicated since contact mapping is performed sequentially. A noninvasive reconstruction of the atrial activation sequence based on the recording of multiple simultaneous ECGs may overcome this limitation.

6.5. Conclusion

Inverse computed isochrones maps were consistent with intracardiac mapping, locating accurately the source of the activation waves during sinus rhythm and atrial tachyarrhythmia. Noninvasive reconstruction of the activation map has demonstrated to be a promising tool in the diagnosis of myocardial diseases with simple propagation patterns due to a limited number of ectopic focis.

7. Noninvasive Estimation of Epicardial Dominant High-Frequency Regions during Atrial Fibrillation

7.1. Introduction

Atrial fibrillation (AF) has a great clinical impact in morbidity and mortality in developed countries [Fuster 2006, Calkins 2007]. Treatment with antiarrhythmic drugs is not always effective and has many secondary effects. These limitations have led to the development of new therapeutic strategies, such as radiofrequency ablation with current success rates in arrhythmia control of 50 to 80 % [Fuster 2006, Calkins 2007].

The use of advanced signal analysis methods has shown that AF is maintained by high-frequency sources located at the junction of the atria with the left pulmonary veins (PV) and less frequently at other sites of the atria, both in animal models and in humans [Mandapati 2000, Mansour 2001, Sanders 2005, Sahadevan 2004, Lazar 2004, Atienza 2006, Lin 2003].

Several clinical studies have shown that, instead of empirically targeting the PVs [8] AF may be eliminated by directly ablating AF-driving sources or "rotors," that maintain the fibrillation with a hierarchical pattern from dominant frequency (DF) regions [Atienza 2009, Atienza 2014, Narayan 2012]. Thus, noninvasive identification of high frequency sources location prior to the ablation procedure could be used to select patients and to guide the ablation procedure.

Previous studies on inverse problem resolution during AF have shown paradoxically simple activation patterns [Haïssaguerre 2013, Cuculich 2010] which do not correspond with the complex propagation patterns recorded either in animal models [Mandapati 2000, Mansour 2001, Berenfeld 2000] or epicardially in patients [Sahadevan 2004, Allessie 2010]. For these reasons, the acceptance of the inverse-problem resolution as a guidance for AF ablation is still controversial. We have recently described the limitations encountered during the estimation of detailed voltage and phase propagation patterns during AF from noninvasive recordings [Rodrigo 2014]. In contrast, activation frequencies computed using spectral analysis has shown to be preserved on the torso surface [Guillem 2013]. The aim of the present study is to evaluate the performance of the inverse problem solution to detect and characterize intracardiac DF distributions during AF. To this purpose, we: 1) determined the feasibility and accuracy of computing dominant frequency (DF) maps from noninvasive recordings in two representative patients with a left-to-right atrial DF pattern and with a right-to-left atrial DF pattern; and 2) assessed the

accuracy of the inverse problem resolution in the voltage, phase and frequency domains by using realistic AF mathematical models, to guide interpretation of the recorded body surface potentials in patients.

7.2. Methods

7.2.1. Simultaneous body surface and intracardiac recordings in AF patients

Patients admitted for ablation of drug-refractory paroxysmal AF (males with paroxysmal AF, 49 and 50 years old) were studied. The ablation protocol as previously described was approved by the Institutional Ethics Committee of our institution and both patients gave informed consent [Guillem 2013]. Both patients arrived in sinus rhythm and AF was induced using electrical burst pacing [Atienza 2011].

In order to reconstruct the heart surface electrical activity by solving the inverse problem of electrocardiography, CAT images were adquired with a spatial resolution of 0.5 mm and multichannel electrocardiograms (ECGs) were recorded with a custom-made vest with 67 chest ECG leads by using the BSPM technique, explained in section 6.2 and shown in Figure 7.1.

Body surface recordings were simultaneously obtained with intracardiac EGMs from the following catheters: (1) a standard tetrapolar catheter in the right atrial appendage (RAA); (2) a decapolar circular mapping Lasso catheter (Biosense-Webster, Diamond Bar, CA) placed either at the left superior pulmonary vein (LSPV) or right superior pulmonary vein (RSPV); and (3) a Navistar catheter (3.5-mm tip, 2-5-2 interelectrode distance; Thermo-Cool, Biosense-Webster, Diamond Bar, CA) used to obtain a DF map of both atria by sequentially obtaining EGMs at different atrial sites (>200 points) for at least 5 seconds. Biatrial intracardiac signals were sequentially acquired at a sampling rate of 977 Hz and dominant frequency (DF) analysis was performed in real time using a CARTO navigation system with embebbed spectral capabilities (CARTO XP, version 7.7; Biosense-Webster, Diamond Bar, CA). Once the highest DF site was identified, the ablation catheter was placed at that site (i.e. LSPV for patient 1 and RAA for patient 2) and a central venous bolus of adenosine (12-18 mg) was administered to produce significant transient atrioventricular block avoiding ventricular activity [Rodrigo 2014, Guillem 2013].

7.2.2. Computational models of the atria and torso

Realistic mathematical models of the atria and torso were used to evaluate the performance of the inverse problem solution during different AF impulse propagation patterns by comparing the generated EGMs to those computed by

solving the inverse problem of electrocardiography (see Figure 7.2). Briefly, the electric potentials on the epicardium were calculated from a realistic computerized model of the atria and used to compute the body surface potentials by applying the forward problem of electrocardiography by using the Boundary Element Method. Simulated ECGs were used to estimate the inverse computed epicardial electrograms (icEGM) by solving the inverse problem of electrocardiography as described below. In order to evaluate the performance of the inverse problem under a realistic noisy situation, icEGM were calculated before and after the addition of white noise in the computed ECG signals (i.e. signal to noise ratio of 10dB).

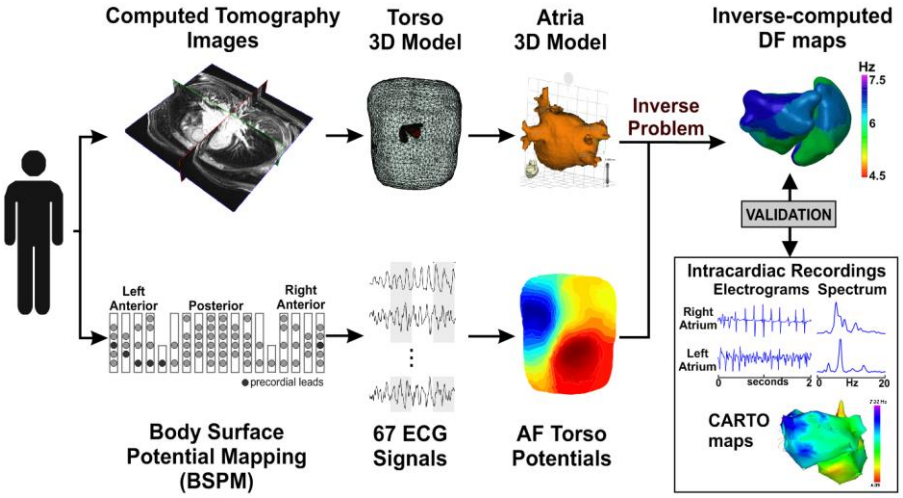

Figure 7.1: Methods for the noninvasive reconstruction of the frequency maps in patients during atria fibrillation.

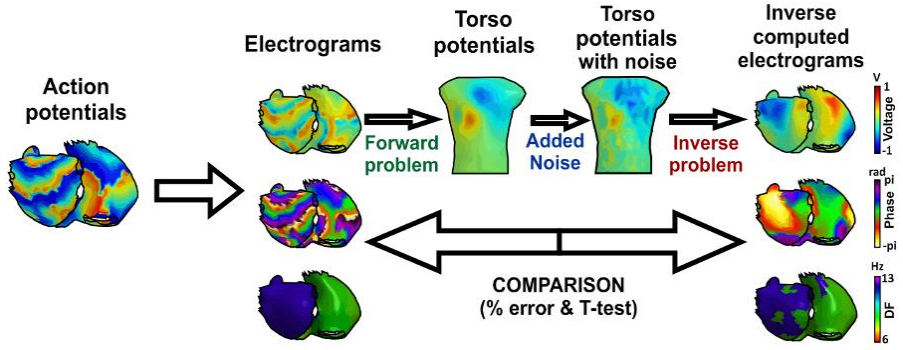

Figure 7.2: Methods for the inverse problem validation in the voltage, phase and frequency domain with mathematical models.

7.2.3. Noninvasive Characterization of Epicardial AF Activity

We estimated icEGM from both patient recordings and body surface voltages computed from mathematical models, by solving the inverse problem of electrocardiography. The transfer function from noninvasive recordings to the epicardium was regularized by using zero-order Tikhonov's method [Tikhonov 1963]. The accuracy of the icEGM was compared for the (1) voltage, (2) phase and (3) frequency domains. Specifically: 1) instantaneous phase was computed by applying the Hilbert's transform [Rodrigo 2014]; 2) power spectral density and DF were computed by using Welch's periodogram with a Hamming window of 2 seconds, 50% overlap and a resolution of 0.25 Hz; and 3) voltage was obtained from preprocessed bipolar intracardiac recordings [Botteron 1996].

Accuracy of reconstructed EGMs was quantified by measuring the relative error between normalized voltage, phase and DF of recorded or modelled EGMs and icEGM. In AF patients, icEGMs were compared with the simultaneously recorded endocardial EGM in three simultaneously recorded catheters; RAA, LSPV and RSPV. In mathematical models, electrograms from 5988 points of the realistic atria were compared. Statistical significance ($p<0.05$) was assessed using the T-test mean difference between the relative errors for the three domains (i.e. voltage, phase and frequency) at each node in the atrial model. The relative error for each node in the voltage and phase domain was computed as the mean relative error over the 5-seconds signal. For the frequency domain, the relative error of the selected highest DF for each node was computed.

7.3. Results

7.3.1. Noninvasive Identification of Atrial DFs during AF

Performance of the inverse problem for the voltage, phase and frequency domains was obtained by comparing simultaneous intracardiac electrograms with the estimation of the inverse problem solution in two AF patients with different distribution patterns of activation frequency. In Figure 7.3.A and Figure 7.3.B, intracardiac EGMs of patient 1 with a left-to-right dominant frequency pattern with increasing activation rates from the RA, to RSPV and LSPV at 5.75 Hz, 6.75 Hz and 7 Hz, respectively are shown. Comparing the intracardiac EGMs (i.e. blue) with the icEGMs (i.e. red), there was a significant error for both the voltage and the phase, whereas the morphology of the power spectrum and the measured DF values were similar. In fact, similar DF values were found on the RA, the LSPV and the RSPV after solving the inverse problem to those obtained in the simultaneous EGMs. As shown in Figure 7.3.C, these results were also supported by the CARTO maps, showing a high similarity to the reconstructed DF maps, also presenting the highest frequency region in the left superior pulmonary veins and, therefore, a righ-to-left frequency gradient.

Patient 2 (Figure 7.4.A and Figure 7.4.B) presented a right-to-left dominant frequency pattern with activation frequencies progressively decreasing from the RA, to RSPV and LSPV at 8 Hz, 6.25 Hz and 5.75 Hz, respectively. Frequencies estimated from the icEGMs presented a similar activation pattern and frequency values as those measured invasively, whereas the reconstruction of the EGMs or the instantaneous phases presented a lower similitude. As it is shown in Figure 7.4.C, these results were also supported by the CARTO maps, showing a high similarity to the reconstructed DF maps, also presenting similar high dominant frequency distributions in the RA and LSPV and right-to-left frequency gradient. However, in this case, unlike the noninvasive DF maps and simultaneous intracardiac recordings, CARTO maps detected 6.25 Hz in the RSPV.

Systematic comparison between intracardiac and icEGMs for the two AF patients corroborated those results with significantly lower relative error for frequency spectrum estimation than for the voltage or the instantaneous phase (i.e. 8.8±4.4% vs. 32±4% and 65±4% respectively, $p<0.01$). Additionally, the inverse problem allowed the reconstruction of the entire atrial DF maps for the same time interval as shown in Figure 7.3.B and Figure 7.4.B. Global DF map determination enabled the location of the highest DF site in the LSPV for patient 1 and in the RAA for patient 2, which is consistent with the DFs measured in the intracardiac recordings.

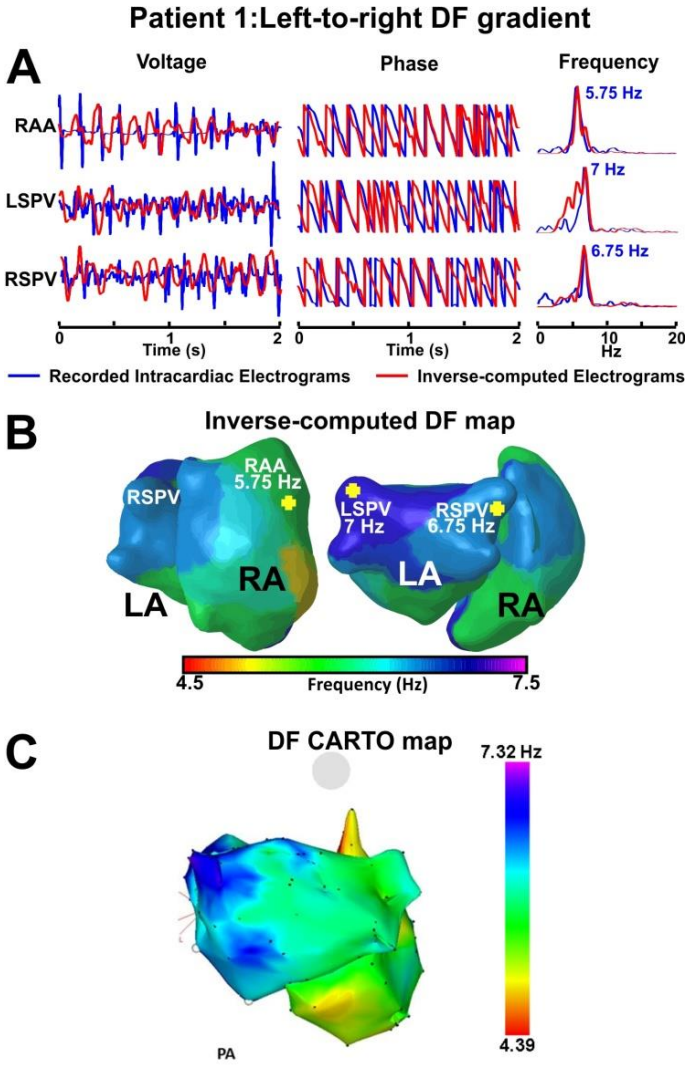

Figure 7.3: Validation of the inverse problem during AF with a left-to-right dominant frequency gradient for the voltage, phase and frequency domains. *(A)* Intracardiac (blue) and icEGMs (red) at the right atrial appendage (RAA), Right Superior Pulmonary Vein (RSPV) and Left Superior Pulmonary Vein (LSPV) and their corresponding instantaneous phase and spectra for patient 1, with a left-to-right DF gradient. *(B)* Inverse-computed DF maps, posterior (right) and right lateral (left) biatrial views. *(C)* DF CARTO map.

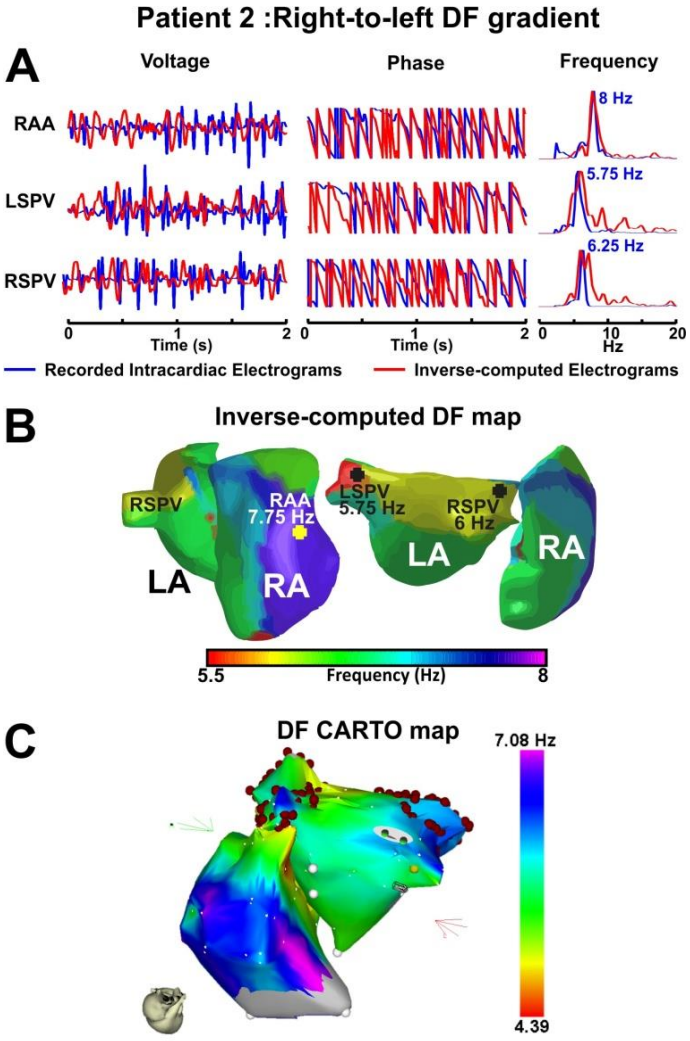

Figure 7.4: Validation of the inverse problem during AF with a right-to-left dominant frequency gradient for the voltage, phase and frequency domains. *(A)* Intracardiac (blue) and icEGMs (red) at the right atrial appendage (RAA), Right Superior Pulmonary Vein (RSPV) and Left Superior Pulmonary Vein (LSPV) and their corresponding instantaneous phase and spectra for patient 2, with a right-to-left DF gradient. *(B)* Inverse-computed DF maps, posterior (right) and right lateral (left) biatrial views. *(C)* DF CARTO map.

7.3.2. Accuracy of the Inverse Problem Resolution

In Figure 7.5, a mathematical model with a left-to-right DF gradient is shown. In this case, the DF gradient is governed by a rotor located at the left atrium as visible from the voltage and phase maps (Figure 7.5.A). Under an ideal situation, in which the representation of the cardiac activity in the torso and the subsequent inverse problem resolution are performed without the addition of noise, inverse-computed voltages and phases represent a smoothened version of original epicardial potentials. However, while some activation wavefronts are properly estimated other activation wavefronts are missed (icEGMs in Figure 7.5.B). On the other hand, dominant frequencies are accurately estimated by solving the inverse problem in most parts of the atria except for certain sites near the inter-atrial septum.

Epicardial potentials reconstructed after addition of noise at 10 dB signal-to-noise (SNR) present an increased smoothening of both voltage distribution and phase to an extent at which activation wavefronts do not match after forward and inverse problem resolution (Figure 7.5.C). Dominant frequency estimation was again performed accurately for most of the atrial surface.

Figure 7.6 shows a mathematical model with a dominant rotor located at the right atrium giving rise to a right-to-left DF gradient. As in the previous example, the resolution of the inverse problem produced a simplified version of the activation pattern of the potential and phase maps, especially under a realistic scenario with a signal to noise ratio of 10 dB. Nevertheless, the addition of the noise did not modify the DF map.

The accuracy of the icEGM to represent the voltage, phase and frequency domains of original EGMs was systematically analyzed with and without the addition of white noise (Figure 7.7). As shown in Figure 7.7.A, error obtained for the frequency DF distribution was lower than the error obtained for the voltage and phase domains, both in the absence and presence of noise (i.e. $p<0.01$). Notice that the addition of noise produced increased relative errors for the three domains. Nevertheless, the error increase was significantly smaller in the frequency domain than in the other two domains (i.e. $p<0.01$), confirming our hypothesis that the frequency domain was the most robust parameter against noise.

The effect of noise in the performance of the inverse problem resolution can also be observed in Figure 7.7.B, where a representative example of EGM from the model in Figure 7.5 is shown. In the absence of added noise, reconstructed EGMs matched modelled EGMs, although sharp voltage transitions were smoothened. However, after the addition of noise to surface potentials, a more pronounced filtering effect of higher order spectral components was observed, resulting in spatial smoothening and a poorer estimation of voltages and phases. This effect might be due to the need to select a higher regularization parameter with added noise. Notice that smoothening produced a non-linear modification of the instantaneous phases for each instant which may explain the poor spatiotemporal reconstruction of the AF

propagation patterns shown in Figure 7.5. In the spectral domain, the dominant peak was well preserved with a reduced power of higher order spectral components confirming that, although the inverse problem may have limitations to reconstruct AF propagation patterns, it allows an accurate reconstruction of DF maps.

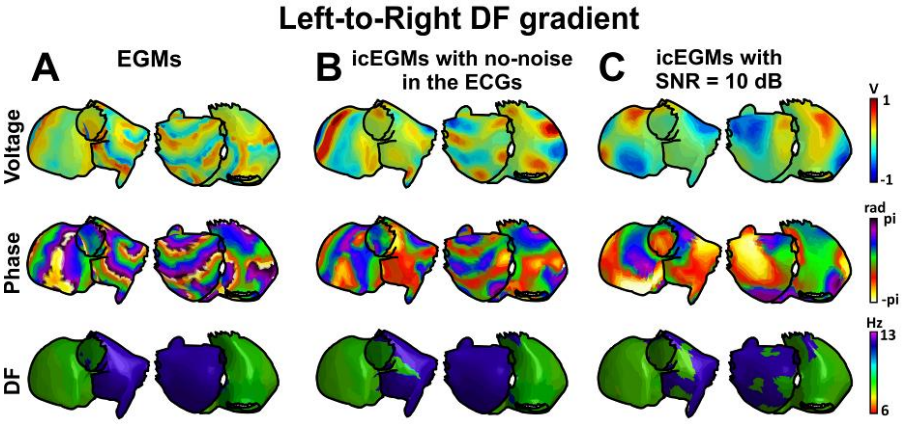

Figure 7.5: Inverse-computed voltage, phase and dominant frequency (DF) maps for simulated AF with a left-to-right DF gradient. *(A)* Voltage, phase and DF maps for generated epicardial EGMs. *(B)* Voltage, phase and DF maps for icEGMs without added noise. *(C)* Voltage, phase and DF maps for icEGM with added noise on surface potentials at 10 dB SNR.

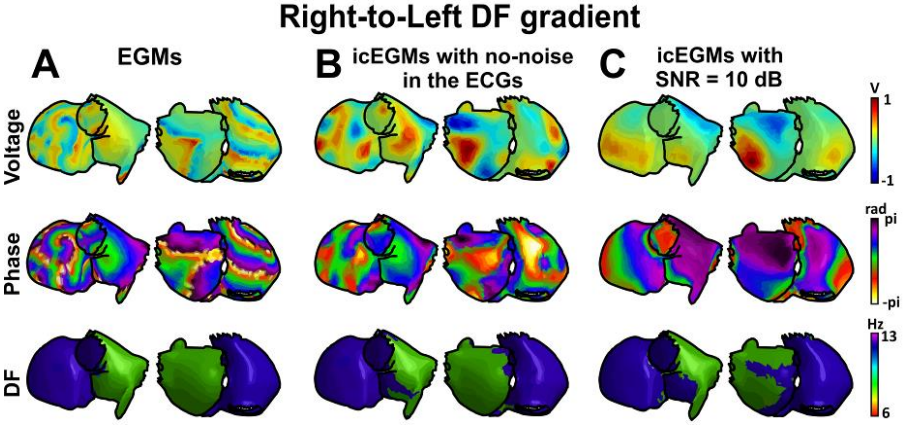

Figure 7.6: Inverse-computed voltage, phase and dominant frequency (DF) maps for simulated AF with a right-to-left DF gradient. *(A)* Voltage, phase and DF maps for generated epicardial EGMs. *(B)* Voltage, phase and DF maps for icEGMs without added noise. *(C)* Voltage, phase and DF maps for icEGM with added noise on surface potentials at 10 dB SNR.

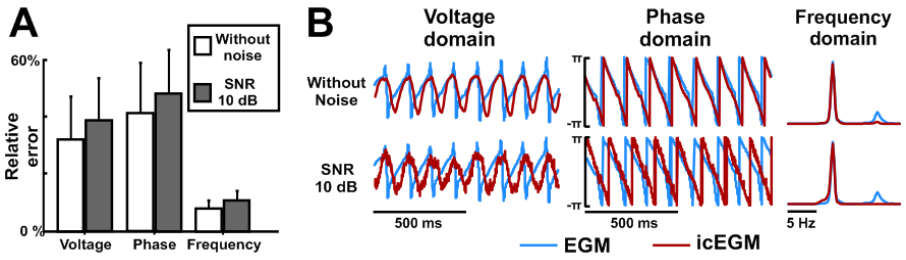

Figure 7.7: Comparison between simulated and inverse-computed EGMs. *(A)* Relative error between icEGMs and original EGMs with and without the addition of white noise to the surface electrocardiograms (i.e. SNR of 10dB). *(B)* Comparison between the original EGMs and icEGMs at a selected atrial site.

7.4. Discussion

The main finding of the present study is that noninvasive estimation of activation frequencies in the atria by solving the inverse problem of electrocardiography is feasible and can be used to accurately compute activation frequency maps during AF. Here, we show that inverse quantification of atrial DF is more accurate than estimation of voltage distributions or their instantaneous phase.

7.4.1. Noninvasive Estimation of Atrial Activation Patterns

The inverse problem of electrocardiography was first applied for solving the electrical activity in the atria for the determination of earliest activation sites during atrial ectopies or pacing [Cuculich 2010, Roten 2012, Pedrón-Torrecilla 2012]. Solution of the inverse problem during non-fibrillatory rhythms has already been proven to be accurate by comparing inverse-computed and intracardially recorded isochronal maps. However, inverse-computed isopotential maps show paradoxically simple patterns during AF that have not been validated with simultaneous intracardiac data [Haïssaguerre 2013, Cuculich 2010]. According to our results, voltage maps may not be inverse-reconstructed accurately, because there is a trade-off between the smoothening introduced by large regularization parameters and an over-reconstruction of noise in the computed electrograms due to small regularization parameters and, consequently, the optimal regularization parameters tended to underestimate the complexity of AF patterns.

7.4.2. Noninvasive Estimation of Atrial Dominant Frequencies

There are experimental and clinical data supporting that in many cases AF is maintained by a region with the highest activation rate [Atienza 2009, Narayan 2012, Lazar 2006]. Ablation of the highest DF in the atria has shown to be an effective therapy for terminating with the arrhythmia [Atienza 2009]. We have recently demonstrated in a randomized clinical trial that in patients with paroxysmal AF, ablation of high frequency sites only is non-inferior and safer that empirically performing circumferential ablation of all PVs. Interestingly, this result was obtained isolating only a mean of 2.22±1.1 PVs [Atienza 2014].

Atrial dominant frequencies have been estimated from surface recordings for decades [Bollmann 1998] and have shown good correlation with global intracardiac atrial DFs [Dibs 2008, Petrutiu 2009]. In a more recent study, we have shown that extensive recordings of surface potentials by BSPM allow detecting the highest dominant frequencies and not only the global activation rate of the overall atrial tissue [Guillem 2013]. However, surface frequency maps only provide a rough estimation of the location of the highest DF site.

Here we have shown that solution of the inverse problem of electrocardiography allows locating this highest DF site in a patient-specific model of the atria, observation that has been validated by using simultaneously recorded intracardiac electrograms. Our simulation study suggests that inverse estimation of spectral features of atrial electrograms during AF is more accurate than the estimation of temporal-based features such as isopotential or phase maps, especially under a realistic noise scenario. The smoothing effect of the torso at non negligible distances from the atria results in the summation of nearby potentials [Rodrigo 2014]. The smoothing effect during classic inverse problem solution using quadratic regularization parameters is required in the presence of noise, but introduces phase distortions that preclude an accurate reconstruction of spatiotemporal variations of non-stochastic phenomena like AF [Allessie 2010]. However, despite those limitations, in the present study we have demonstrated that the inverse problem can be used to reconstruct the DF map and consequently detect the region of the atria that hierarchically maintains AF.

7.4.3. Limitations of the study

In this study we have validated the estimation of inverse-computed DF maps with a limited number of simultaneous intracardiac recordings. Validation with simultaneous basket catheters may provide more insights into the accuracy of inverse computed potentials and DFs. However, contact in basket catheters is also compromised which would also be a limitation. In our study, DF maps were also validated with CARTO maps with hundreds of mapping points. However, CARTO maps were not simultaneously acquired to the BSPM recordings, and thus the actual activation frequencies cannot be compared, although the global hierarchical pattern

was preserved. In addition, surface maps were recorded during intravenous adenosine injection which does not only produce a transient atrio-ventricular block but also accentuates the highest frequencies, without affecting the atrial frequency gradient or the location of the highest DF site [Atienza 2006, Atienza 2007].

However, we made use of mathematical models in which the activity in the entire atria is known to support our observations regarding the superiority of DF estimation over time-based metrics. Although the mathematical models employed may be over-simplistic, they were complex enough to validate our hypothesis: that the main spectral components (namely, the DF) are better preserved than the morphology of the EGMs or their phases. Validation with more complex mathematical models would only make these results worse.

Another limitation of the study is that only two patients were used for validation. However, these two patients represent two different locations of the highest DF site location (i.e. right vs. left) and may be representative of a broader range of atrial DF patterns.

7.5. Conclusion and Clinical Implications

Atrial high frequency sources can be identified noninvasively by solving the inverse problem of electrocardiography with a higher accuracy than the morphology of potentials or their phase. Noninvasive computation of DF maps prior to and during an ablation procedure may help in patient selection and personalized procedure planning.

8. Discussion

8.1. Main findings

The general objective of electrocardiography is the quantitative and qualitative explanation of the relationship between the electrical activity of the heart and the electrical activity on the torso, achieved by the resolution of the "forward" and "inverse" problems of electrocardiography.

In this thesis, different strategies for the noninvasive reconstruction of the electrical activity of the myocardium were developed and tested for different activation patterns and diseases, including the moving-dipole estimation and myocardial inverse solutions. In this thesis the inverse problem resolution strategy was fitted to each propagation pattern in order to minimize the error and increase the stability of the resolution system.

For simple propagation patterns that can be summarized into a single or double dipolar source located in the myocardium, a novel iterative method for indirectly solving the inverse problem of electrocardiography was implemented. This method iteratively finds the linear combination of stored torso potentials, previously generated by solving the forward problem for linear independent dipoles, which best matches with the surface potentials recorded. This method may allow the noninvasive diagnosis of cardiac diseases by the identification and location of the region of the myocardium with an electrical disturbance.

This simplified representation of the activity of the heart, widely used in the clinical field, has a higher stability than other inverse problem resolution methods that can lead to non-physiological solutions under noise conditions. By restricting the myocardial activity to a limited number of dipoles to solve the inverse problem, the solution is more robust against noise. However, this simplification of the electrical activity of the heart into a limited number of dipoles does not always allow for an accurate representation of the electrical activity of the heart, in particular during electrical disorders such as atrial fibrillation or multiple re-entrant propagation patterns.

Inverse solutions in terms of epicardial potentials allow for a more complete reconstruction of the myocardial electrical activity and thus the analysis of other parameters of the EGMs, like the morphology, the duration or the activation time. The duration, activation time and morphology of the non-invasively computed EGMs in 6 patients with diagnosed Brugada syndrome and 6 controls were analysed and compared. Inverse-computed EGMs of Brugada syndrome patients showed activation abnormalities in the RVOT region, independently of the BrS type, being consistent with experimental observations. The study showed a significant ($p<0.01$) longer duration and later activation in the reconstructed EGMs in the RVOT region

of the BrS patients, but not in the apex or the septum regions. The noninvasive reconstruction of the ventricular EGMs in BrS patient was consistent with experimental observations, and thus may allow the noninvasive clinical diagnosis with independence of the BrS phenotype and without infusion of cardiac channel blockers. Inverse problem resolution was also applied in patients for the reconstruction of the activation sequence for different atrial activation patterns including sinus rhythm and pulmonary veins pacing. The activation sequence was computed non-invasively by solving the inverse problem and allowed locating accurately the source of the atrial activation. The results were always consistent with the simultaneous intracardiac recordings, which evidenced that the inverse problem can be used for the noninvasive location of atrial ectopic foci during atrial tachyarrhythmia, and may be a promising tool for planning an ablation procedure.

These methods were implemented for the noninvasive reconstruction of the intracardiac EGMs in the voltage and time domain, and demonstrated a good accuracy for simple propagation patterns such as atrial ectopic sources or ventricular activation in BrS. However, for complex signals like atrial fibrillation, the inverse problem overregulates the solution and therefore, the solution in the voltage and phase domains is over-smoothed, which hampers source location. An alternative strategy for solving the inverse problem of electrocardiography was implemented that consisted in the detection of highest dominant frequency (DF) sources during atrial fibrillation. The noninvasive reconstruction of the DF maps was validated with mathematical cell models and real patients with AF. For the mathematical validation, realistic atrial models were used and AF patterns with different DF distributions were generated and surface potentials were computed by solving the forward problem and adding noise at signal-to-noise ratio of 10 dB. The clinical study included patients with a history of AF in which body surface potential mapping recordings were recorded simultaneously to endocardial EGMs during the electrophysiological study. Mathematical and patient validation of the inverse problem resolution in the voltage, phase and frequency domains were compared and it was shown that for atrial fibrillation propagation pattern, the noninvasive reconstruction of the frequency maps is significantly ($p<0.01$) more accurate than in the voltage or phase domains. The noninvasive identification of the AF frequency gradient and the location of the highest dominant frequency sources can be accurately achieved by solving the inverse problem of electrocardiography, which may help in planning ablation procedures, since the prior knowledge of the frequency gradient and AF source location may avoid interseptal procedures for right-to-left frequency gradients cases and could facilitate the targeting of the AF source.

Each method showed a good performance for each different application and propagation pattern, even for complex myocardial activity, proving its advantages and disadvantages for different diseases, depending on their myocardial activation pattern.

8.2. Comparison with previous studies

The inverse problem of electrocardiography has a potential value for the noninvasive diagnosis and treatment of cardiac diseases, allowing the noninvasive reconstruction of the electrical activity of the heart. Due to its ill-posed nature and multiple solutions, the accuracy of inverse problem of electrocardiography solution depends mainly on the input signal to noise ratio, the geometrical input model and the potential pattern to be calculated. The scientific community has proposed different solutions for the inverse problem computation by using different regularization methods, different volume models or surface meshing or by using different electrical cardiac models, seeking for the method that minimizes the inverse reconstruction error and increases the stability of the system [Gabor 1954, Barr 1966, Geselowitz 1960, Savard 1982, Barr 1976, Messinger-Rapport 1990]. However, the best inverse resolution method does depend on the underlying propagation pattern. This thesis focused on the analysis of the inverse problem resolution for different electric heart models and analysis domains by comparing and classifying each propagation pattern and disease with the corresponding optimal resolution strategy.

In this thesis an alternative indirect method based on a multiple moving dipole representation of the heart electrical activity was proposed and validated. Although different solutions for the dipolar inverse problem resolution were proposed by the scientific community, they were solved for infinite homogeneous models [Armoundas 2003, Geselowitz 1960, Gulrajani 1984]. Gulrajani et al. presented a method for solving numerically the inverse problem on an infinite homogeneous model by solving numerical complex method based on multipole expansions [Gulrajani 1984]. However this solution does not correspond to the reality and requires a complex formulation. In contrast, the method proposed in this thesis finds the optimal dipole configuration that minimizes the error between the generated torso potentials by solving the forward problem and the recorded potentials and then, it works in realistic models with any volume conductor complexity, without restricting the model to an infinite homogeneous medium [Pedron-Torrecilla 2010_a, Pedron-Torrecilla 2010_b]. The scientific community also presented inverse dipolar solutions for locating a single moving dipole for a realistic torso [Nelder 1965, Fukuoka 2006,] based on the minimization of a function of *n* variables [Nelder 1965, Lai 2010,], determining the 6 variables (x, y, z dipolar location and orientation), adapting itself to the local landscape, contracting on to the final minimum error. As an alternative to these analytic dipolar inverse resolutions, the proposed method does not solve the forward problem for each iteration [Lai 2010, Nelder 1965], but uses a previously stored potential database which simplifies the computation.

Inverse solution in terms of epicardial potentials is the most widely used method for inverse computing the actual intracardiac sources, since it allows the complete

estimation of the electrical activity of the myocardium. This technique was validated for simple propagation patterns and demonstrated its ability to reconstruct the myocardial electrical activity in the voltage and phase domains for atrial and ventricular diseases.

Morphology of intracardiac electrograms is a useful marker for the diagnosis in BrS since EGMs reflect abnormalities in the action potentials [Wilde 2010, Meregalli 2005, Nademanee 2011, Antzelewitch 2005_a, Antzelewitch 2002, Antzelewitch 2001, Morita 2010]. Although BrS action potentials and ECGs are widely studied by the scientific community, inverse reconstruction of the EGMs of BrS patients has not been performed for the noninvasive diagnosis of the disease independently of their phenotype. Our analysis of the morphology and activation times of the ventricular activity in BrS-I and BrS-nI patients was consistent with the experimental results of BrS in animal models and human subjects but from a noninvasive perspective [Antzelevitch 2005_a, Meregalli 2005, Wilde 2010, Antzelevitch 2001, Antzelevitch 2002].

Inverse solution in terms of epicardial potentials is also used for the noninvasive reconstruction of atrial electrical activity. Some authors have reported the noninvasive location of the ectopic focus or macrorrentries in atrial flutter [Roten 2012, Messinger-Rapport 1990, Seger 2006, Han 2013, Zhang 2013]. Similarly to these works, in this thesis inverse solutions in terms of epicardial potentials achieved accurate results for simple propagation patterns, like atrial arrhythmias due to ectopic foci, validated with simultaneous intracardiac mapping.

However, the accuracy of the inverse solution is strongly limited for complex propagation patterns like AF. Although inverse solution has been recently studied in the voltage and phase domains [Cuculich 2010, Haïssaguerre 2013], results are often over smoothed and over optimistic, simplifying the complex AF activity that has been reported in intracardiac recordings of human [Allessie 2010]. In this work, inverse solutions in the voltage and phase domain for complex AF propagation pattern were also over smoothed, especially for low signal-to-noise ratios, showing propagation patterns similar to the solutions presented by Cuculich et al. or Haïssaguerre et al. [Cuculich 2010, Haïssaguerre 2013], which appear to be paradoxically simple as compared to the complexity of intracadiac electrograms. In this thesis, we propose the noninvasive identification and location of high dominant frequency sources, based on the assumption that in many cases atrial drivers present the highest activation rate with an intermittent propagation to the rest of the tissue that activates at a slower rate [Atienza 2009, Mansour 2001, Lazar 2006, Narayan 2012]. Although, the voltage and phase inverse solutions were over smoothed and inaccurate for increasing noise levels on the torso signals, inverse reconstruction of DF maps was accurate for AF complex propagation patterns even for a low signal-to-noise ratio, allowing the identification of the atrial site with the highest activation rate.

8.3. Limitations

The presented inverse problem solution in terms of epicardial potentials was solved with zero order Tikhonov regularization and we did not test alternative regularization methods. As reported in the literature, Greensite combined time-space regularization method to improve the inverse solution by including prior knowledge or the solution obtained in previous time instants [Greensite 2003]. However, zero-order Tikhonov is still the most widely used in the literature and offers a good solution for simple propagation patterns and for this reason we wanted to test its accuracy in the reconstruction of epicardial electrograms.

A realistic validation of the inverse problem of electrocardiography should not only consider the addition of noise but also inaccuracies in the volume conductor geometry and conductivity. Our inverse problem validation included the addition of noise at different signal to noise ratios but was performed with the same torso model for the forward and inverse problem resolutions. However, we believe that the main conclusions of this thesis would also hold for these complex validation scenarios.

In this thesis different methods for solving the inverse problem were implemented and tested for different diseases and propagation patterns, however, a complete parametric analysis was not performed in order to study the influence of the different parameters and variables for each developed algorithm and therefore we cannot rule out for more accurate solutions as those presented here. However, our accuracy was similar to that reported in the literature.

The databases used for the evaluation of the inverse problem had several limitations regarding the number of patients, the number of the simultaneous intracardiac electrodes used for validating the reconstructed potentials in the atrial fibrillation database or the absence of CAT images in the BrS patients. Therefore, the extrapolation of the results to a general population is limited. Although the intracardiac electrodes used for evaluation under AF provided an estimation of the general propagation and activation time in the myocardium, it was not possible to have complete intracardiac maps of the electrical activity. In either case, we had a higher number of electrodes for evaluation than most inverse problem studies. In order to support the clinical results and compensate for these limitations, we generated different propagation patterns with mathematical models, allowing a complete knowledge of the electrical activity in the myocardium and thus allowed us to confirm our observations in patients.

9. Conclusions and future works

9.1. Conclusions

The main purpose of electrocardiography is to describe the electrical activity of the heart based on the torso surface ECGs. Solution of the inverse problem resolution is a big challenge since it is ill-posed, very sensitive to noise and has multiple solutions. The selection of the optimal parameters, methodology or electrical cardiac model is critical for achieving a stable and accurate inverse computed reconstruction.

This thesis focused on the analysis of the inverse problem resolution for different diseases and propagation patterns by developing different algorithms and strategies for solving the inverse problem of electrocardiography. The algorithms were applied in the noninvasive diagnosis of ventricular and atrial arrhythmias and evaluated with mathematical cellular models and clinical data bases.

Different strategies for the inverse problem resolution were proposed, minimizing the error and increasing the stability of the system for the different propagation patterns.

Noninvasive reconstruction of the dipolar electrical activity was accurate for simple propagation patterns that can be represented by a dipolar approach, allowing the diagnosis of diseases electrically characterized by a limited number of dipoles. This method added additional constrains to the solution, increasing the stability of the solution. However, this technique shows the qualitative behavior of the electrical activity but it is not possible to have an accurate estimation of the myocardial activity at all myocardial regions.

The noninvasive estimation of the heart electrical activity in terms of epicardial potentials is of great importance for diseases characterized by an abnormal morphology of the action potentials. The analysis of the morphological parameters, like the duration, fragmentation or activation time of the inverse computed ventricular EGMs could be used for the noninvasive diagnosis of BrS.

Noninvasive epicardial activation map reconstruction, based on the inverse solution of the epicardial potentials, allowed the complete knowledge and visualization of the isochrones maps in the myocardium. This method is of great importance for organized and stationary propagation patterns, like ectopic foci or simple reentrant propagation patterns, being very easy the identification and location of reentries and initiation sites. However, for complex propagation patterns like AF, this method showed simplistic and over-smoothed solutions that do not correspond to the actual intracardiac electrograms recorded in patients.

In this thesis we proposed a novel noninvasive high dominant frequency maps reconstruction, based on the theory that atrial fibrillation sources activates at a

higher frequency rate leading to intermittently propagation patterns. In this thesis we proved with mathematical and patient results that, although voltage and phase inverse computed results during AF were over-smoothed and inaccurate, the noninvasive estimation of frequency maps was significantly more accurate than in the voltage and phase domains, allowing the identification of the AF frequency gradient and location of high frequency sources, even for complex non-stationary activation of the myocardium of the myocardium or with a low signal-to-noise ratio. This novel technique may be of great importance since it may avoid unnecessary interseptal punctures for right-to-left frequency gradients cases and facilitate the targeting of the AF drivers, reducing risks and time of ablation procedures.

9.2. Future works

The methodology described in this thesis focuses on the inverse resolution with different strategies and methodologies for different cardiac propagation patterns. However, the inverse problem is still a great challenge in electrocardiography and is in continuous improvement. In this section, a guide for performing further studies of the inverse problem based on the work described in this thesis is presented.

The only way to improve a method is to know how the different parameters and variables present in a real application of the inverse problem affect the system. A parametric analysis of the inverse problem accuracy could be implemented, comparing the inverse-computing error in function of the noise level, torso model meshing and error reconstruction, or the conductivity estimation. L-curve behavior is strongly linked to the inverse solution error and, therefore, the study of the L-curve morphology (slope of the two regions of the L-Curve and magnitude of the curvature and corner location) and their relationship with the analyzed parameters may be a promising tool to adjust model parameters such as surface meshing, location and conductivities of the different volume conductors and thus reduce reconstruction errors. In particular, the slopes in the L-curve are related with the model reconstruction accuracy, since the steeper corner of the L-curve is reached for the best match between real and estimated anatomies. Therefore, these results could be used to refine the 3D model reconstruction, adjust the conductivity of the different volume conductors or for noise filtering, which could improve stability and reduce the estimation errors.

Iterative dipolar algorithm proved a good behavior for simple propagation patterns; however, this method was not performed for real clinical cases. The morphological study of the electrograms for the BrS patients was performed, but the dipolar iterative method could also be validated for BrS or other diseases with a simple propagation pattern, characterizing the dipolar activation sequence in the different regions of the myocardium. Following this methodology, a BrS patient may present an abnormal behavior of the dipole located in the RVOT or a patient with an ectopic focus may present additional dipoles at the same location of each

source. A comparative study between the inverse computed activation maps, activation sequence of the dipoles, and the morphology of the electrograms could be implemented for different clinical cases, quantifying their accuracy depending on the disease.

Isochrone maps and inverse resolution in the voltage, phase and frequency domain were performed for simple and complex propagation pattern. Although the simplicity of the wave propagation for an atrial tachycardia due to an ectopic focus or BrS and the higher complexity during AF are obvious, the grade of complexity and curvature of the different myocardial waves could be quantified and compared with the accuracy of the different methods described in this thesis. Thereby, we may know accurately the grade of complexity and morphology of the propagation patterns and, consequently, establish a system based on an objective criterion for the optimal selection of the inverse problem strategy.

Although different methods and strategies were presented in this work, they are based on the BEM systems and most of them are based on the Tikhonov regularization and the L-curve selection of the regularization parameter. Other methods for the surface meshing, system regularization, regularization parameter selection or time-space additional constrains presented in sections 2.5 and 2.6 could be used and compared for the different methods, domains and propagation patterns analyzed in this thesis.

10. Contributions

10.1. Main publications of this thesis

10.1.1. Journal papers

- Pedrón-Torrecilla J, Rodrigo M, Climent AM, Liberos A, Pérez-David E, Bermejo J, Arenal A, Millet J, Fernández-Avilés F, Berenfeld O, Atienza F, Guillem MS. Noninvasive Estimation of Epicardial Dominant High-Frequency Regions during Atrial Fibrillation. Journal of Cardiovascular Electrophysiology. (Under review)

10.1.2. International conferences

- Pedrón-Torrecilla J, Climent AM, Liberos A, Rodrigo M, Pérez-David E, Millet J, Fernández-Avilés F, Berenfeld O, Atienza F, Guillem MS. Accuracy of Inverse Solution Computation of Dominant Frequencies and Phases during Atrial Fibrillation. Computing in Cardiology 2014. 41:537-540.
- Atienza F, Pedrón-Torrecilla J, Climent AM, Liberos A, Pérez-David E, Millet J, Fernández-Avilés F, Berenfeld O, Guillem MS. Noninvasive Estimation of Dominant High-Frequency Regions during Atrial Fibrillation: Validation of the Inverse Problem Resolution. Hearth Rhythm Scientific Sessions 2014. 11:S440.
- Pedrón-Torrecilla J, Liberos A, Millet J, Climent AM, Guillem MS. Accuracy of non-invasive frequency estimation using atrial fibrillation. Computing in Cardiology 2013. 40:1183-1186.
- Pedrón-Torrecilla J, Climent AM, Liberos A, Pérez-David E, Millet J, Atienza F, Guillem MS. Noninvasive Estimation of the Activation Sequence in the Atria during Sinus Rhythm and Atrial Tachyarrhythmia. Computing in Cardiology 2012. 39:901-904.
- Pedrón-Torrecilla J, Climent AM, Millet J, Berné P, Brugada J, Brugada R, Guillem MS. Characteristics of inverse-computed epicardial electrograms of Brugada syndrome patients. 33rd Annual International Conference of the IEEE Engineering in Medicine and Biology Society (EMBC '11) 2011. 2011:235-238.

- Pedrón J, Climent AM, Millet J, Guillem MS. An Iterative Method for Indirectly Solving the Inverse Problem of Electrocardiography. Computing in Cardiology 2010. 37:89-92.

10.1.3. National conferences

- Pedrón-Torrecilla J, MS Guillem, AM Climent, Liberos Mascarell A, Rodrigo Bort M, Berenfeld O, Atienza F, Fernández-Avilés F. Reconstrucción no invasiva de los mapas electroanatómicos de frecuencia dominante durante fibrilación auricular. Congreso de las Enfermedades Cardiovasculares 2014. 67:391.
- Pedrón-Torrecilla J, Climent AM, Liberos A, Pérez-David E, Millet J, Atienza F, Guillem MS. Estimación no invasiva de la secuencia de activación auricular durante el ritmo sinusal y taquiarritmia auricular. XXX Congreso Anual de la Sociedad Española de Ingeniería Biomédica 2012. 2012:1-4.
- Pedrón-Torrecilla J, Climent AM, Millet J, Berné P, Brugada J, Brugada R, Guillem MS. Características de los potenciales epicárdicos de pacientes son síndrome de Brugada: aplicación del problema inverso. XXIX Congreso Anual de la Sociedad Española de Ingeniería Biomédica 2011. 2011:1-4.
- Pedrón Torrecilla J, Martínez Climent A, Liberos Mascarell A, Millet Roig J, Guillem Sánchez MS. Estudio Comparativo de un Método Iterativo para la Resolución Indirecta del Problema Inverso de la Electrocardiografía. XXVIII Congreso Anual de la Sociedad Española de Ingeniería Biomédica 2010. 2010:1-4.

10.2. Publications related to this thesis

10.2.1. Journal papers

- Rodrigo M, Guillem MS, Climent AM, Pedrón-Torrecilla J, Liberos A, Millet J, Fernández-Avilés F, Atienza F, Berenfeld O. Body surface localization of left and right atrial high-frequency rotors in atrial fibrillation patients: a clinical-computational study. Heart Rhythm 2014. 11:1584-1591.
- Liberos A, Climent AM, Rodrigo M, Pedrón-Torrecilla J, Millet J, Atienza F, Berenfeld O, Quesada A, Guillem MS. Non-invasive Characterization of Atrial Macroreentries during Typical and Atypical Atrial Flutter. Europace. (Submitted)

10.2.2. Book chapter

- Miguel Rodrigo, Jorge Pedrón-Torrecilla, Ismael Hernández, Alejandro Liberos, Andreu M. Climent, María S. Guillem. Data Analysis in cardiac arrhythmias. Eds: Carlos Fernández-Llatas, Juan Miguel García-Gómez. Data Mining in Clinical Medicine. Methods in Molecular Biology 2014. 1246:217-236.

10.2.3. International conferences

- Pedrón-Torrecilla J, Liberos A, Rodrigo M, Millet Roig J, Felipe A, Berenfeld O, Climent AM, Guillem Sánchez MS. Non-invasive imaging of the atrial arrhythmia sources: patient study during atrial tachyarrhythmia and atrial fibrillation. ITACA-WIICT 2014. 1:10-17.
- Liberos A, Climent AM, Rodrigo M, Pedrón-Torrecilla J, Millet J, Quesada A, Guillem MS. Non-Invasive Phase Analysis in Atrial Flutter Electrographic Maps. CARDIOSTIM 2014. S96:16.
- Rodrigo M, Guillem MS, Climent AM, Liberos A, Pedrón-Torrecilla J, Fernández-Avilés F, Atienza F, Berenfeld O. Body surface detection of reentrant activity during atrial fibrillation. CARDIOSTIM 2014. S96:17.
- Rodrigo M, Climent AM, Liberos A, Pedrón-Torrecilla J, Millet J, Fernández-Avilés F, Atienza F, Berenfeld O, Guillem MS. Non-invasive Location of Re-Entrant Propagation Patterns during Atrial Fibrillation. Computing in Cardiology 2013. 40:1235-1238.
- Berenfeld O, Rodrigo M, Climent AM, Liberos A, Pedrón-Torrecilla J, Millet J, Arenal A, Fernández-Avilés F, Atienza F and Guillem MS. Noninvasive

identification of reentrant drivers of atrial fibrillation using multi-channel surface recordings. Hearth Rhythm Scientific Sessions 2013. 10:310.

- Liberos A, Pedrón-Torrecilla J, Rodrigo M, Millet J, Climent AM, Guillem MS. Body surface Potential Propagation Maps During Macroreentrant Atrial Arrhythmias: A Simulation Study. Computing in Cardiology 2013. 40:915-918.

10.2.4. National conferences

- Rodrigo Bort M, Climent AM, Liberos Mascarell A, Pedrón Torrecilla J, Fernández-Avilés F, Berenfeld O, Atienza F, Guillem MS. El análisis causal de la actividad eléctrica durante fibrilación auricular permite identificar los patrones de propagación dominante. Congreso de las Enfermedades Cardiovasculares 2013. 66:15-21.
- Rodrigo Bort M, Guillem MS, Climent AM, Liberos Mascarell A, Pedrón Torrecilla J, Millet Roig J, Berenfeld O, Atienza F. Identificación no invasiva de patrones fibrilatorios mediante registro electrocardiográfico de superficie. Congreso de las Enfermedades Cardiovasculares 2013. 66:15-21.
- Liberos Mascarell A, Martínez Climent A, Pedrón Torrecilla J, Millet Roig J, Guillem Sánchez MS. Arquitectura Reconfigurable para el Mapeo Eléctrico de Potenciales Cardiacos basada en LabVIEWTM XXVIII Congreso Anual de la Sociedad Española de Ingeniería Biomédica 2010. 2010:5-8.

10.3. Author contribution

The theoretical work and computer programming related to the forward and inverse problem resolution was carried out by Jorge Pedrón Torrecilla, the author of this thesis. The author also implemented the tools for the analytical validation and the subsequently validation of the methods. The author accomplished the patient data analysis necessary for the development of the work, including the BSPM signal processing and the image segmentation for the torso model construction, and analysed the results extracted during the research development. During the research stay in the "Hospital Gregorio Marañón", the author also contributed in increasing the patient data base previously recorded by Dr. Andreu Martínez Climent. Main publications of this thesis were written by the author and by Dr. María de la Salud Guillem Sánchez.

Mr. Alejandro Liberos computed the mathematical models and test scenarios needed for the in-silico validation of the implemented methods.

Mr. Miguel Rodrigo implemented the algorithms for the phase signal analysis.

Dr. Esther Pérez-David performed the Computer Tomography images acquisition necessary for the 3D torso model reconstruction.

Dr. Atienza, Fernández-Avilés, Josep and Ramón Brugada gave us access to patients and performed intracardiac recordings when it was necessary.

Dr. Fernández-Avilés, Dr. Millet, Dr. Berenfeld and Dr. M.Climent revised and approved final versions of the publications.

10.4. Research stays

Research stay at "*The University of Minnesota*", Minneapolis, U.S.A, in the "*Biomedical Functional Imaging and Neuroengineering Laboratory*", leaded by the Pr. He.
Dates: From 1st September until 30th November 2011.
Main tasks: Noninvasive imaging of atrial arrhythmias in terms of current density.

Research stay at the "*Hospital General Universitario Gregorio Marañón*", Madrid, Spain, leaded by the Dr. Fernández-Avilés and Dr. Atienza.
Dates: From 1st September until 31th December 2012.
Main tasks: Signal processing and analysis for the noninvasive localization of atrial arrhythmias. Body surface potential mapping and simultaneous intracardiac recording in patients with atrial fibrillation. Magnetic Resonance Imaging recording and image segmentation.

Work exchange at "*Université de Bordeaux*", Pessac, France, in the "*L'Institut de RYthmologie et Modélisation Cardiaque (LIRYC)",* leaded by Dr. Haïssaguerre, Dr. Bernus and Dr. Dubois. In collaboration with Mauna Kea Technologies™.
Dates: From 1st September until 30th November 2014.
Main tasks: Firmware programming and hardware design of a configurable electronic system for the automatic triggering of the cardiac recording system in function of the systolic pressure.
Discussion of topics in inverse problem during lab meetings.

References

[Abboud 1994] Abboud S, Eshel Y, Levy S, Rosenfeld M. Numerical calculation of the potential distribution due to dipole sources in a spherical model of the head. Comput Biomed Res 1994. 27:441-455.

[Allessie 2010] Allessie MA, de Groot NM, Houben RP, Schotten U, Boersma E, Smeets JL, Crijns HJ. Electropathological substrate of long-standing persistent atrial fibrillation in patients with structural heart disease: longitudinal dissociation. Circ Arrhythm Electrophysiol 2010. 3:606-615.

[Antzelewitch 1998] Antzelevitch C. The Brugada syndrome. J Cardiovasc Electrophysiol 1998. 9:513-16.

[Antzelewitch 2001] Antzelevitch C. The Brugada syndrome: ionic basis and arrhythmia mechanisms. J Cardiovasc Electrophysiol 2001. 12:268-272.

[Antzelewitch 2002] Antzelevitch C. Late potentials and the Brugada syndrome. J Am Coll Cardiol 2002. 39:1996-1999.

[Antzelevitch 2005_a] Antzelevitch C, Brugada J, Brugada P, Brugada R. The Brugada syndrome: From Bench to Bedside. Blackwell 2005.

[Antzelevitch 2005_b] Antzelevitch C, Brugada P, Borggrefe M, Brugada J, Brugada R, Corrado D, Gussak I, LeMarec H, Nademanee K, Perez Riera AR, Shimizu W, Schulze-Bahr E, Tan H, Wilde A. Brugada syndrome: report of the second consensus conference. Circulation 2005. 111:659-670.

[Antzelewitch 2006] Antzelevitch C. Brugada syndrome. Pacing Clin Electrophysiol 2006. 29:1130-1159.

[Armoundas 2003] Armoundas AA, Feldman AB, Mukkamala R, He B, Mullen TJ, Belk PA, Lee YZ, Cohen RJ. Statistical accuracy of a moving equivalent dipole method to identify sites of origin of cardiac electrical activation. IEEE Trans Biomed Eng 2003. 50:1360-1370.

[Arthur 1972] Arthur RM, Geselowitz DB, Briller SA, Trost RF. Quadrupole components of the human surface electrocardiogram. Am Heart J 1972. 83:663-677.

[Atienza 2006] Atienza F, Almendral J, Moreno J et al: Activation of inward rectifier potassium channels accelerates atrial fibrillation in humans-Evidence for a Reentrant mechanism. Circulation 2006. 114:2434-2442.

[Atienza 2007] Atienza F, Jalife J. Reentry and atrial fibrillation. Heart Rhythm 2007. 4:S13-16.

[Atienza 2009] Atienza F, Almendral J, Jalife J, Zlochiver S, Ploutz-Snyder R, Torrecilla E, Arenal A, Kalifa J, Fernandez Aviles F, Berenfeld O. Real-time dominant frequency mapping and ablation of dominant frequency sites in atrial fibrillation with left-to-right frequency gradients predicts long-term maintenance of sinus rhythm. Heart Rhythm 2009. 6:33-40.

[Atienza 2011] Atienza F, Calvo D, Almendral J, Zlochiver S, Grzeda KR, Martínez-Alzamora N, González-Torrecilla E, Arenal A, Fernández-Avilés F, Berenfeld O: Mechanisms of fractionated electrograms formation in the posterior left atrium during paroxysmal atrial fibrillation in humans. J Am Coll Cardiol 2011. 57:1081-1092.

[Atienza 2014] Atienza F, Almendral J, Ormaetxe JM, Moya A, Martínez-Alday JD, Hernández-Madrid A, Castellanos E, Arribas F, Arias MÁ, Tercedor L, Peinado R, Arcocha MF, Ortiz M, Martínez-Alzamora N, Arenal A, Fernández-Avilés F, Jalife J. Comparison of Radiofrequency Catheter Ablation of Drivers versus Circumferential Pulmonary Vein Isolation in Patients with Atrial Fibrillation: A Noninferiority Randomized Multicenter RADAR-AF Trial. J Am Coll Cardiol 2014. 64:2455-2467.

[Barr 1976] Barr RC, Spach MS. Inverse solutions directly in terms of potentials. The theoretical basis of the electrocardiography 1976. 294-304.

[Barr 1977] Barr RC, Ramsey M, Spach MS. Relating epicardial to body surface potential distributions by means of transfer coefficients based on geometry measurements. IEEE Trans Biomed Eng 1977. 24:1-11.

[Barr 1999] Barr RC, Pilkington TC, Boineau JP, Spach MS. Determining surface potentials from current dipoles with application to electrocardiography. lEEE Trans Biomed Eng 13 1966. 88-92.

[Belhassen 1999] Belhassen B, Viskin S, Fish R, Glick A, Setbon I, Eldar M. Effects of electrophysiologic guided therapy with class 1A antiarrhythmic drugs on the longterm outcome of patients with idiopathic ventricular fibrillation with or without the Brugada syndrome. J Cardiovasc Electrophysiol 1999. 10:1301-1312.

[Belhassen 2002] Belhassen B, Viskin S, Antzelevitch C. The Brugada syndrome. Is an implantable cardioverter defibrillator the only therapeutic option? Pacing Clin Electrophysiol 2002. 25:1634-1640.

[Berenfeld 2000] Berenfeld O, Mandapati R, Dixit S, Skanes AC, Chen J, Mansour M, Jalife J. Spatially distributed dominant excitation frequencies reveal hidden organization in atrial fibrillation in the Langendorff-perfused sheep heart. J Cardiovasc Electrophysiol 2000. 11:869-879.

[Berruezo 2004] Berruezo A, Mont L, Nava S, Checa E, Bartholomay E, Brugada J. Electrocardiographic recognition of the epicardial origin of ventricular tachycardias.

Circulation 2004. 109:1842-1847.

[Bollmann 1998] Bollmann A, Kanuru NK, McTeague KK, Walter PF, DeLurgio DB, Langberg JJ: Frequency analysis of human atrial fibrillation using the surface electrocardiogram and its response to ibutilide. Am J Cardiol 1998. 81:1439-1445.

[Botteron 1996] Botteron GW, Smith JM. Quantitative assessment of the spatial organization of atrial fibrillation in the intact human heart. Circulation 1996. 93:513-518.

[Brugada 1992] Brugada P, Brugada R. Right bundle branch block, persistent ST segment elevation and sudden cardiac death: a distinct clinical and electrocardiographic syndrome. JACC 1992. 20:1391-1396.

[Brugada 2000] Brugada J, Brugada R, Brugada P. Pharmacological and device approach to therapy of inherited cardiac diseases associated with cardiac arrhythmia and sudden death. J Electrocardiol 2000. 33:41-47.

[Bruns 2002] Bruns HJ, Eckardt L, Vahlhaus C, Schulze-Bahr E, Haverkamp W, Borffrefe M, Breithardt G, Wichter T. Body surface potential mapping in patients with Brugada syndrome: right precordial ST segment variations and reverse changes in left precordial leads. Cardiovascular Research 2002. 54:58-66.

[Calkins 2007] Calkins H, Brugada J, Packer DL, Cappato R, Chen SA, Crijns HJ, Damiano RJ Jr, Davies DW, Haines DE, Haïssaguerre M, Iesaka Y, Jackman W, Jais P, Kottkamp H, Kuck KH, Lindsay BD, Marchlinski FE, McCarthy PM, Mont JL, Morady F, Nademanee K, Natale A, Pappone C, Prystowsky E, Raviele A, Ruskin JN, Shemin RJ. HRS/EHRA/ECAS Expert consensus statement on catheter and surgical ablation of atrial fibrillation: Recommendations for personnel, policy, procedures and follow-up. Heart Rhythm 2007. 4:816-861.

[Carley 2003] Carley S.D. Beyond the 12 Lead: Review of the use of additional leads for the early electrocardiographic diagnosis of acute myocardial infarction. Emerg Med 2003. 15:143-154.

[Campuzano 2013] Campuzano O, Allegue C, Iglesias A, Brugada R. Genetic Basis of Brugada síndrome. Genet Syndr Gene Ther 2013. 4:167.

[Cerqueira 2002] Cerqueira MD, Weissman NJ, Dilsizian V, Jacobs AK, Kaul S, Laskey WK, Pennell DJ, Rumberger JA, Ryan T, Verani MS. Standarized Myocardial Segmentation and Nomenclature for Tomographic imaging of the Heart: A Statement for Healthcare Professionals From the Cardiac Imaging Committee of the Council on Clinical Cardiology of the American Heart Association. Circulation 2002. 105:539-542.

[Connoly 2000] Connoly S, Gent M, Robin S. Canadian Implantable Defibrillator Study (CIDS). A randomized trial of the implantable cardioverter defibrillator

against amiodarone. Circulation 2000. 101:1297-1302.

[Courtemanche 1998] Courtemanche M, Ramirez RJ, Nattel S. Ionic mechanisms underlying human atrial action potential properties: Insights from a mathematical model. Am J Physiol -Heart Circul Physiol 1998. 275:H301-H321.

[Cowper 1972] Cowper GR. Gaussian Quadrature Formulas For Triangles. Int J Num Meth Eng 1972. 7:405-408.

[Cuculich 2010] Cuculich PS, Wang Y, Lindsay BD, Faddis MN, Schuessler RB, Damiano Jr RJ, Li L, Rudy Y. Noninvasive characterization of epicardial activations in humans with diverse atrial fibrillation patterns. Circulation 2010. 122:1364-1372.

[De Ambroggi 1986] De Ambroggi L, Bertoni T, Locati E, Stramba-Badiale M, Schwartz PJ. Mapping of body surface potentials in patients with the idiopathic QT syndrome. Circulation 1986. 74:1334-1345.

[de Groot 2010] de Groot NM, Houben RP, Smeets JL, Boersma E, Schotten U, Schalij MJ, Crijns H, Allessie MA. Electropathological substrate of longstanding persistent atrial fibrillation in patients with structural heart disease: epicardial breakthrough. Circulation 2010. 122:1674-1682

[De Guise 1985] De Guise J, Gulrajani RM, Savard P, Guardo R, Roberge FA. Inverse Recovery of two Moving Dipoles from Simulated Surface Potential Distributions on a Realistic Human Torso Model. IEEE Trans Biomed Eng 1985. 32:126-134.

[De Munck 1992] De Munck JC. A linear Discretization of the Volume Conductor Boundary Integral Equation Using Analytically Integral Elements. IEEE Trans Biomed Eng 1992. 39:986-990.

[Dibs 2008] Dibs SR, Ng J, Arora R, Passman RS, Kadish AH, Goldberger JJ. Spatiotemporal characterization of atrial activation in persistent human atrial fibrillation: multisite electrogram analysis and surface electrocardiographic correlations: a pilot study. Heart Rhythm 2008 5:686-693.

[Dunavant 1985] Dunavant DA. High degree efficient symmetrical Gaussian quadrature rules for the triangle. Int J Numer Meth Eng 1985. 21:1129-1248.

[Eckardt 2002] Eckardt L, Bruns H. J, Paul M, Kirchhof P, Schulze-Bahr E, Wichter T, Breithardt G, Borggrefe M, Haverkamp W. Body surface area of ST elevation and the presence of late potentials correlate to the inducibility of ventricular tachyarrhythmias in brugada syndrome. J Cardiovasc Electrophysiol 2002. 13:742-749.

[Einthoven 1895] Einthoven W. Über die Form des menschlichen Electrocardiogramms. Arch Ges Physiol 1895. 60:101-123.

[Einthoven 1903] Einthoven W. Die galvanometrische Registrierung des menschlichen Elektrokardiogramms, zugleich eine Beurteilung der Anwendung des Kapillar-Elektrometers in der Physiologie. Pflügers Arch Ges Physiol 1903. 99:472-480.

[Einthoven 1908] Einthoven W. Weiteres ber das elektrokardiogram. Pfger Arch Ges Physiol 1908. 122:517-548.

[Einthoven 1912] Einthoven W. The different forms of the human electrocardiogram and their signification. Lancet 1912. 1:853-861.

[Fedorov 2012] Fedorov A, Beichel R, Kalpathy-Cramer J, Finet J, Fillion-Robin JC, Pujol S, Bauer C, Jennings D, Fennessy F, Sonka M, Buatti J, Aylward S, Miller JV, Pieper S,Kikinis R. 3D Slicer as an Image Computing Platform for the Quantitative Imaging Network. Magn Reson Imaging 2012. 30:1323-1341.

[Finlay 2005] Finlay DD, Nugent CD, McCullagh PJ, Black ND. Mining for diagnostic information in body surface potential maps: A comparison of feature selection techniques. BioMedical Engineering OnLine 2005. 4:51 (http://www.biomedical-engineering-online.com/content/4/1/51#B1)

[Fischer 2000] Fischer G, Tilg B, Modre R, Huiskamp GJ, Fetzer J, Rucker W, Wach P. A bidomain model based BEM-FEM coupling formulation for anisotropic cardiac tissue. Ann Biomed Eng 2000. 28:1229-1243.

[Frank 1954] Frank E. Determination of the electrical center of ventricular depolarization in the human heart. American Heart Journal 1954. 49:670-692.

[Franzone 1985] Colli Franzone P, Gnerri L, Tentonia S, Viganotti C, Baruffi S. A mathematical procedure for solving the inverse potential problem of electrocardiography. Analysis of the timespace accuracy from in vitro experimental data. Math Biosci 1985. 77:353-396.

[Frijns 2000] Frijns JHM, de Snoo SL, Schoonhoven R. Improving the accuracy of the boundary element method by the use of second-order interpolation functions. IEEE Trans Biomed Eng. 2000. 47:1336-1346.

[Fukuoka 2006] Fukuoka Y, Oostendorp TF, Sherman DA, Armoundas AA: Applicability of the single equivalent moving dipole model in an infinite homogeneous medium to identify cardiac electrical sources: A computer simulation study in a realistic anatomic geometry torso model. IEEE Trans Biomed Eng 2006. 53:2436-2444.

[Fuster 2006] Fuster V, Ryden LE, Cannom DS, et al. ACC/AHA/ESC 2006 Guidelines for the Management of Patients with Atrial Fibrillation: a report of the American College of Cardiology/American Heart Association Task Force on Practice Guidelines and the European Society of Cardiology Committee for Practice

Guidelines (Writing Committee to Revise the 2001 Guidelines for the Management of Patients With Atrial Fibrillation): developed in collaboration with the European Heart Rhythm Association and the Heart Rhythm Society. Circulation 2006. 114:257-354.

[Gabor 1954] Gabor D, Nelson CV. Determination of the resultant dipole of the heart from measurements on the body surface. J AppL Phys 1954. 25:413-416.

[García 2011] García VM, Liberos A, Climent AM, Vidal A, Millet J, González A. An adaptive step size GPU ODE solver for simulating the electric cardiac activity. Computing in Cardiology 2011. 38:233-236.

[Garcia-Molla 2014] Garcia-Molla V, Liberos A, Vidal A, Guillem MS, Millet J, Gonzalez A, Martinez-Zaldivar FJ, Climent AM: Adaptive step ODE algorithms for the 3D simulation of electric heart activity with graphics processing units. Comput Biol Med 2014; 44:15-26.

[Gardner 1986] Gardner MJ, Montague TJ, Armstrong CS, Horácek BM, Smith ER. Vulnerability to ventricular arrhythmias: assessment by mapping of body surface potentials. Circulation 1986. 73:684-692.

[Golub 1979] Golub GH, Heath M, Wahba G. Generalized cross-validation as a method for choosing a good ridge parameter. Technometrics 1979. 21:215-223.

[Geselowitz 1960] Geselowitz DB. Multipole representation for an equivalent cardiac generator. Proc IRE 1960. 48:75-79.

[Geselowitz 1967] Geselowitz DB. On Bioelectric Potentials in an Inhomogeneous Volume Conductor. Biophys J 1967. 7:1-11.

[Greensite 2003] Greensite F. The temporal prior in bioelectromagnetic source imaging problems. IEEE Trans Biomed Eng 2003. 50:1152-1159.

[Groetsch 1984] Groetsch CW. The Theory of Tikhonov Regularization for Fredholm Equations of the First Kind. Pitman Publishing 1984. 43-52.

[Guillem 2009_a] Guillem MS, Quesada A, Donis V, Climent AM, Mihi N, Millet J, Castells F. Surface wavefront propagation maps: Non-invasive characterization of atrial flutter circuit. Int J Bioelectromagn 2009. 11:22-26.

[Guillem 2009_b] Guillem MS, Climent A.M, Castells F, Husser D, Millet J, Arya A, Piorkowski C, Bollmann A. Noninvasive mapping of human atrial fibrillation. J Cardiovasc Electrophysiol 2009. 20:507-513.

[Guillem 2009_c] Guillem MS, Bollmann A, Climent A, Husser D, Millet J, Castells A. How many leads are necessary for a reliable reconstruction of surface potentials during atrial fibrillation. IEEE Trans Inf Technol Biomed 2009. 13:330-340.

[Guillem 2010] Guillem MS, Climent AM, Millet J, Berne P, Ramos R, Brugada J, Brugada R. Conduction abnormalities in the right ventricular outflow tract in Brugada syndrome detected Body Surface Potential Mapping. Conf Proc IEEE Eng Med Biol Soc 2010. 2010:2537-2540.

[Guillem 2013] Guillem MS, Climent A.M, Millet J, Arenal Á, Fernández-Avilés F, Jalife J, Atienza F, Berenfeld O. Noninvasive localization of maximal frequency sites of atrial fibrillation by body surface potential mapping. Circ Arrhythm Electrophysiol 2013. 6:294-301.

[Gulrajani 1984] Gulrajani RM, Roberge FA, Savard P. Moving dipole inverse ECG and EEG solutions. IEEE Trans. Biomed Eng 1984. BME-31:903-910.

[Hadamard 1902] Hadamard J. Sur Les Problèmes Aux Dérivées Partielles et Leur Signification Physique. Princeton University Bulletin 1902. 13:49-52.

[Hadamard 1923] Hadamard J. Lectures on the Cauchy Problem in Linear Partial Differential Equations. Yale University Press 1923. New York NY, USA.

[Haïssaguerre 1998] Haïssaguerre M, Jaïs P, Shah D, Takahashi A, Hocini M, Quiniou G, Garrigue S, Le Mouroux A, Le Métayer P, Clémenty J. Spontaneous initiation of atrial fibrillation by ectopic beats originating in the pulmonary veins. N Engl J Med 1998. 339:659-666.

[Haïssaguerre 2013] Haïssaguerre M, Hocini M, Shah AJ, Derval N, Sacher F, Jais P, Dubois R. Noninasive panoramic mapping of human atrial fibrillation mechanisms: A feasibility report. JCE 2013. 24:711-717.

[Han 2013] Han C, Pogwizd SM, Killingsworth CR, Zhou Z, He B. Noninvasive cardiac activation imaging of ventricular arrhythmias during drug-induced QT prolongation in the rabbit heart. Heart Rhythm 2013. 10:1509-1515.

[Hansen 1993] Hansen PC, O'Leary DP: The use of the L-curve in the regularization of discrete ill-posed problems. SIAM J Sci Stat Comput 1993. 14:1487-1503.

[Harrild 2000] Harrild DM, Henriquez CS. A computer model of normal conduction in the human atria. Circ Res 2000. 87:E25-E36.

[Hodgkin 1952] Hodgkin AL, Huxley AF. A quantitative description of membrane current and its application to conduction and excitation in nerve. J Physiol 1952. 117:500-544.

[Hoekema 1999] Hoekema R, Uijen GJH, van Oosterom A. On selecting a Body Surface Mapping Procedure. J Electrocardiol 1999. 32:93-101.

[Horácek 1997] Horácek BM, Clements JC. The Inverse Problem of Electrocardiography: A Solution in Terms of Single- and Double-Layer Sources on

the Epicardial Surface. Math Biosci 1997. 144:119-154.

[Hren 1998] Hren R, Stroink G, Horácek BM. Accuracy of single-dipole inverse solution when localizing ventricular pre-excitation sites: Simulation study. Med Biol Eng Comput 1998. 36:323.329.

[Huebner 1982] Huebner KH, Thorntou EA. The Finite-Element Method for Engineers 1982. 2nd ed., Wiley, New York.

[Jain 1995] Jain R, Kasturi R, Schunck BG, Machine Vision, Mc Graw Hill 1995. 196. New York NY, USA.

[Jais 1997] Jaïs P, Haïssaguerre M, Shah DC, Chouairi S, Gencel L, Hocini M, Clémenty J.. A focal source of atrial fibrillation treated by discrete radiofrequency ablation. Circulation 1997. 95:572-576.

[Jais 2002] Jaïs P, Hocini M, Macle L, Choi KJ, Deisenhofer I, Weerasooriya R, Shah DC, Garrigue S, Raybaud F, Scavee C, Le Metayer P, Clémenty J, Haïssaguerre M. Distinctive electrophysiological properties of pulmonary veins in patients with atrial fibrillation. Circulation 2002. 106:2479-2485.

[Johnston 2000] Johnston PR, Gulrajani RM. Selecting the Corner in the L-Curve Approach to Tikhonov Regularization. IEEE transactions on biomedical engineering 2000. 47:1293-1296.

[Konings 1994] Konings KT, Kirchof CJ, Smeets JR, Wellens HJ, Penn OC, Allessie MA. High-density mapping of electrically induced atrial fibrillation in humans. Circulation 1994. 89:1665-80.

[Konings 1997] Konings KTS, Smeets JLRM, Penn OC, et al. Configuration of unipolar atrial electrograms during electrically induced atrial fibrillation in humans. Circulation 1997. 95:1231-1241.

[Kuck 2000] Kuck KH, Cappato R, Siebels J, Rüppel R. Randomized comparison of antiarrhythmic drug therapy with implantable defibrillators in patients resuscitated from cardiac arrest: the Cardiac Arrest Study Hamburg (CASH). Circulation 2000. 102:748-754.

[Kumagai 2000] Kumagai, K. et al.Role of rapid focal activation in the maintenance of atrial fibrillation originating from the pulmonary veins. Pacing Clin. Electrophysiol 2000. 23:1823-1827.

[Lai 2010] Lai D, Liu C, Eggen MD, Iaizzo PA, He B: Equivalent moving dipole localization of cardiac ectopic activity in a swine model during pacing. IEEE Trans Inf Technol Biomed 2010. 14:1318-1326.

[Lambiase 2009] Lambiase PD, Ahmed AK, Ciaccio EJ, Brugada R, Lizotte E, Chaubey S, Ben-Simon R, Chow AW, Lowe MD, McKenna WJ. High-Density

Substrate Mapping in Brugada Syndrome: Conbine Role of Conduction and Repolarization Heterogeneities in Arrhythmogenesis. Circulation 2009. 120:106-117.

[Lazar 2004] Lazar S, Dixit S, Marchlinski FE, Callans DJ, Gerstenfeld EP: Presence of left-to-right atrial frequency gradient in paroxysmal but not persistent atrial fibrillation in humans. Circulation 2004. 110:3181-3186.

[Lazar 2006] Lazar S, Dixit S, Callans DJ, Lin D, et al. Effect of pulmonary vein isolation on the left-to-right atrial dominant frequency gradient in human atrial fibrillation. Heart Rhythm. 2006; 3:889-895. Lemola K, Ting M, Gupta P, et al. Effects of two different catheter ablation techniques on spectral characteristics of atrial fibrillation. J Am Coll Cardiol 2006. 48:340-348.

[Liberos 2013] Liberos A, Pedrón-Torrecilla J, Rodrigo M, Millet J, Climent AM, Guillem MS. Body surface Potential Propagation Maps During Macroreentrant Atrial Arrhythmias: A Simulation Study. Comput in Cardiol 2013. 40:915-918.

[Liberos 2014] Liberos A, Climent AM, Rodrigo M, Pedrón-Torrecilla J, Millet J, Quesada A, Guillem MS. Non-Invasive Phase Analysis in Atrial Flutter Electrographic Maps. CARDIOSTIM 2014. S96:16.

[Lin 2003] Lin WS, Tai CT, Hsieh MH, Tsai CF, Lin YK, Tsao HM, Huang JL, Yu WC, Yang SP, Ding YA, Chang MS, Chen SA. Catheter Ablation of Paroxysmal Atrial Fibrillation Initiated by Non−Pulmonary Vein Ectopy. Circulation 2003. 107:3176-3183

[Litovsky 1990] Litovsky SH, Antzelevitch C. Differences in the electrophysiological response of canine ventricular subendocardium and subepicardium to acetylcholine and isoproterenol. A direct effect of acetylcholine in ventricular myocardium. Circ Res 1990. 67:615-627.

[Liu 2006] Liu Z, Liu C, He B. Noninvasive reconstruction of three-dimensional ventricular activation sequence from the inverse solution of distributed equivalent current density. IEEE Trans Biomed Eng. 2006. 25:1307-1318.

[MacLeod 1991] MacLeod RS, Johnson CR, Ershler PR. Construction of an inhomogeneous model of the human torso for use in computational electrocardiography. 13th Ann Int Conf, IEEE Eng Med and Biol Soc 1991.1991:688-989.

[MacLeod 1998] MacLeod RS, Brooks DH. Recent progress in Inverse Problems in Electrocardiology. IEEE Eng Med Biol 1998. 17:73-83.

[Malmivuo 1995] Malmivuo J, Plonsey R. Bioelectromagnetism. Principles and Applications of Bioelectric and Biomagnetic Fields. 1995.

[Mandapati 2000] Mandapati, R, Skanes, A, Chen, J, Berenfeld, O, Jalife, J. Stable

microreentrant sources as a mechanism of atrial fibrillation in the isolated sheep heart. Circulation 2000. 101:194-199.

[Mansour 2001] Mansour MC, Mandapati R, Berenfeld O, Chen J, Samie FH, Jalife J. Left-to-right gradient of atrial frequencies during acute atrial fibrillation in the isolated sheep heart. Circulation 2001. 103:2631-2636.

[Meijs 1989] Meijs JWH, Weier OW, Peters MJ, Van Oosterom A. On the Numerical Accuracy of the Boundary Element Method. IEEE Trans Biomed Eng 1989. 36:1038-1049.

[Messinger-Rapport 1990] Messinger-Rapport BJ, Rudy Y. Noninvasive recovery of epicardial potentials in a realistic heart-torso geometry. Normal sinus rhythm. Circ Res 1990. 66:1023-1039.

[Meregalli 2005] Meregalli PG, Wilde AA, Tan HL. Pathophysiological mechanisms of Brugada syndrome: depolarization disorder, repolarization disorder, or more? Cardiovasc Res 2005. 67:367-378.

[Miller 1970] Miller K. Least squares methods for ill-posed problems with a prescribed bound. SIAM J Math Anal 1970. 1:52-74

[Mitchell 1992] Mitchell LB, Hubley-Kozey CL, Smith ER, Wyse DG, Duff HJ, Gillis AM, Horácek BM. Electrocardiographic body surface mapping in patients with ventricular tachycardia: assessment of utility in the identification of effective pharmacological therapy. Circulation 1992. 86:383-393.

[Miyazaki 1996] Miyazaki T, Mitamura H, Miyoshi S, Soejima K, Aizawa Y, Ogawa S. Autonomic and antiarrhythmic drug modulation of ST segment elevation in patients with Brugada syndrome. J Am Coll Cardiol 1996. 7:1061-1070.

[Moe 1959] Moe GK, Abildskov JA. Atrial fibrillation as a self-sustaining arrhythmia independent of focal discharge. Am Heart J 1959. 58:59-70.

[Morita 2008] Morita H, Zipes DP, Fukushima-Kusano K, Nagase S, Nakamura K, Morita ST, et al. Repolarization heterogeneity in the right ventricular outflow tract: correlation with ventricular arrhythmias in Brugada patients and in an in vitro canine Brugada model. Heart Rhythm 2008. 5:725-733.

[Morita 2009] Morita H, Zipes DP, Wu J. Brugada syndrome: insights of ST elevation, arrhythmogenicity, and risk stratification from experimental observations. Heart Rhythm 2009. 6:34-43.

[Morozov 1984] Morozov VA. Methods for Solving Incorrectly Posed Problems. Springer-Verlag 1984, New York. 44-47.

[Nademanee 2004] Nademanee K, McKenzie J, Kosar E, et al. A new approach for catheter ablation of atrial fibrillation: mapping of the electrophysiologic substrate. J

Am Coll Cardiol 2004. 43:2044 -2053.

[Nadenamee 2011] Nademanee K, Veerakul G, Chandanamattha P, Chaothawee L, Ariyachaipanich A, Jirasirirojanakorn K, Likittanasombat K, Bhuripanyo K, Ngarmukos T. Prevention of Ventricular Fibrilation Episodes in Brugada Syndrome by Catheter Ablation Over the Anterior Right Ventricular Outflow Trat Epicardium. Circulation 2011. 123:1270-1279.

[Narayan 2012] Narayan SM, Krummen DE, Shivkumar K, Clopton P, Rappel WJ, Miller JM. Treatment of Atrial Fibrillation by the Ablation of Localized Sources. JACC 2012. 60:628-636.

[Nattel 1998] Nattel S. Experimental evidence for proarrhythmic mechanisms of antiarrhythmic drugs. Cardiovasc Res 1998. 37:567-577.

[Nattel 2002] Nattel S. New ideas about atrial fibrillation 50 years on. Nature 2002. 415:219-226.

[Nelder 1965] Nelder JA, Mead R. A simplex method for function minimization. Comput J 1965. 7:308-313.

[Olgin 1995] Olgin JE, Kalman JM, Fitzpatrick AP, Lesh MD. Role of right atrial endocardial structures as barriers to conduction during human type I atrial flutter. Activation and entrainment mapping guided by intracardiac echocardiography. Circulation 1995. 92:1839-1848.

[O'Neil 2010] O'Neil BJ, Hoekstra J, Pride YB, Lefebvre C, Diercks D, Frank Peacock W, Fermann G.J, Michael Gibson C, Pinto D, Giglio J.F, Chandra A, Cairns CB, Clark C, Massaro J, Krucoff M. Incremental benefit of 80-lead electrocardiogram body surface mapping over the 12-lead electrocardiogram in the detection of acute coronary syndromes in patients without ST-elevation myocardial infarction: Results from the Optimal Cardiovascular Diagnostic Evaluation Enabling Faster Treatment of Myocardial Infarction (OCCULT MI) trial. Acad Emerg Med 2010.17:932-939.

[Oosterom 1983] van Oosterom A, Strakee J. The solid angle of a plane triangle. IEEE Trans Biomed Eng 1983. 30:125-126.

[Oral 2002] Oral H, Knight BP, Tada H, et al. Pulmonary vein isolation for paroxysmal and persistent atrial fibrillation. Circulation 2002. 105:1077-1081.

[Oral 2003] Oral H, Scharf C, Chugh A, Hall B, Cheung P, Good E, Veerareddy S, Pelosi F Jr, Morady F. Catheter ablation for paroxysmal atrial fibrillation: segmental pulmonary vein ostial ablation versus left atrial ablation. Circulation 2003. 108:2355-2360.

[Oral 2007] Oral H, Chugh A, Good E, Wimmer A, Dey S, Gadeela N, Sankaran S, Crawford T, Sarrazin JF, Kuhne M, Chalfoun N, Wells D, Frederick M, Fortino J,

Benloucif-Moore S, Jongnarangsin K, Pelosi F Jr, Bogun F, Morady F. Radiofrequency catheter ablation of chronic atrial fibrillation guided by complex electrograms. Circulation 2007. 115:2606-2612.

[Oster 1992] Oster H, Rudy Y. The use of temporal information in the regularization of the inverse problem of electrocardiography. IEEE Trans Biomed Eng 1992. 39:65-75.

[Pedrón-Torrecilla 2010_a] Pedrón J, Climent AM, Millet J, Guillem MS. An Iterative Method for Indirectly Solving the Inverse Problem of Electrocardiography. Computing in Cardiology 2010. 37:89-92.

[Pedrón-Torrecilla 2010_b] Pedrón-Torrecilla J, Climent AM, Guillem MS. Implementación y estudio de métodos numéricos para la resolución del problema inverso de la electrocardiografía: modelado de la actividad eléctrica en la superficie del torso. Master dissertation 2010, Universitat Politècnica de València.

[Pedrón-Torrecilla 2010_c] Pedrón Torrecilla J, Martínez Climent A, Liberos Mascarell A, Millet Roig J, Guillem Sánchez MS. Estudio Comparativo de un Método Iterativo para la Resolución Indirecta del Problema Inverso de la Electrocardiografía. XXVIII Congreso Anual de la Sociedad Española de Ingeniería Biomédica 2010. 2010:1-4.

[Pedrón-Torrecilla 2011] Pedrón-Torrecilla J, Climent AM, Millet J, Berné P, Brugada J, Brugada R, Guillem MS. Characteristics of inverse-computed epicardial electrograms of Brugada sindrome patients. 33rd Ann Int Conf IEEE Eng Med Biol Soc 2011. 2011:235-238.

[Pedrón-Torrecilla 2012] Pedrón-Torrecilla J, Climent A, Liberos A, Pérez-David E, Millet J, Atienza F, Guillem MS: Non-Invasive Estimation of the Activation Sequence in the Atria during Sinus Rhythm and Atrial Tachyarrhythmia. Comput Cardiol 2012. 39:901-904.

[Pedrón-Torrecilla 2014] Pedrón-Torrecilla J, Climent AM, Liberos A, Rodrigo M, Pérez-David E, Millet J, Fernández- Avilés F, Berenfeld O, Atienza F, Guillem MS. Accuracy of Inverse Solution Computation of Dominant Frequencies and Phases during Atrial Fibrillation. Comput Cardiol 2014. 41:537-540.

[Petrutiu 2009] Petrutiu S, Sahakian AV, Fisher W, Swiryn S. Manifestation of left atrial events and interatrial frequency gradients in the surface electrocardiogram during atrial fibrillation: contributions from posterior leads. J Cardiovasc Electrophysiol 2009. 20:1231-1236.

[Pilkington 1982] Pilkington TC, Morrow MN. The usefulness of multipoles in electrocardiography. CRC Crit Rev Biomed Eng 1982. 7:175-192.

[Porter 2008] Porter M, Spear W, Akar JG, Helms R, Brysiewicz N, Santucci

P, Wilber DJ. Prospective study of atrial fibrillation termination during ablation guided by automated detection of fractionated electrograms. J Cardiovasc Electrophysiol 2008. 19:613-620.

[Postema 2008] Postema PG, van Dessel PF, de Bakker JM, Dekker LR, Linnenbank AC, Hoogendijk MG, Coronel R, Tijssen JG, Wilde AA, Tan HL. Slow and discontinuous conduction conspire in Brugada syndrome: a right ventricular mapping and stimulation study. Circ Arrhythm Electrophysiol 2008. 1:379-386.

[Postema 2010] Postema PG, van Dessel PF, Kors JA, Linnenbank AC, van Herpen G, Ritsema van Eck HJ, van Geloven N, de Bakker JM, Wilde AA, Tan HL. Local depolarization abnormalities are the dominant pathophysiologic mechanism for type 1 electrocardiogram in brugada syndrome a study of electrocardiograms, vectorcardiograms, and body surface potential maps during ajmaline provocation. J Am Coll Cardiol 2010. 55:789-797.

[Purcell 1991] Purcell CJ, Stroink G. Moving dipole inverse solutions using realistic torso models. IEEE Trans BiomedEng 1991. 38: 82-84.

[Ralston 1978] Ralston A, Rabinowitz P. A First Course in Numerical Analysis. McGraw-Hill 1978, New York. Chap 8.

[Ramanathan 2004] Ramanathan C, Ghanem RN, Jia P, Ryu K, Rudy Y. Noninvasive electrocardiographic imaging for cardiac electrophysiology and arrhythmia. Nat Med 2004. 10:422-428.

[Richter 2009] Richter S, Sarkozy A, Veltmann C, Chierchia GB, Boussy T, Wolpert C, Schimpf R, Brugada J, Brugada R, Borggrefe M, Brugada P. Variability of the diagnostic ECG pattern in an ICD patient population with Brugada syndrome. J Cardiovasc Electrophysiol 2009. 20:69-75.

[Rodrigo 2014] Rodrigo M, Guillem MS, Climent AM, Pedrón-Torrecilla J, Liberos A, Millet J, Fernández-Avilés F, Atienza F, Berenfeld O: Body surface localization of left and right atrial high-frequency rotors in atrial fibrillation patients: a clinical-computational study. Heart Rhythm 2014. 11:1584-1591.

[Rosenfeld 1996] Rosenfeld M, Tanami R, Abboud S. Numerical solution of the potential due to dipole sources in volume conductors with arbitrary geometry and conductivity. IEEE Trans Biomed Eng 1996. 43:679-689.

[Roten 2012] Roten L, Pedersen M, Pasacale P, Shah A, Eliautou S, Scherr D, Sacher F, Haïssaguerre M. Noninvasive Electrocardiographic Mapping for Prediction of Tachycardia Mechanism and Origin of Atrial Tachycardia Following Bilateral Pulmonary Transplantation. J Cardiovasc Electrophysiol 2012. 23:553-555.

[Rudy 1979] Rudy Y, Plonsey R. The Eccentric Spheres Model as the Basis for a Study of the Role of Geometry and Inhomogeneities in Electrocardiography. IEEE

Trans Biomed Eng 1979. 26:392-399.

[Rudy 1988] Rudy Y, Messinger-Rapport BJ. The inverse problem in electrocardiography: solutions in terms of epicardial potentials. Crit Rev Biomed Eng 1988. 16:215-268.

[Sahadevan 2004] Sahadevan J, Ryu K, Peltz L, Khrestian CM, Stewart RW, Markowitz AH, Waldo AL. Epicardial mapping of chronic atrial fibrillation in patients: preliminary observations. Circulation 2004. 110:3293-3299.

[Sanders 2005] Sanders P, Berenfeld O, Hocini M, et al: Spectral analysis identifies sites of high-frequency activity maintaining atrial fibrillation in humans. Circulation 2005. 112:789-797.

[Sarvas 1987] Sarvas J. Basic mathematical and electromagnetic Concepts of the biomagnetic inverse problem. Phys Med Biol 1987. 32:11-22.

[Savard 1982] Savard P, Mailloux GE, Roberge FA, Gulrajani RM, Guardo R. A simulation study of the single moving dipole representation of cardiac electrical activity. IEEE Trans Biomed Eng 1982. 29:700-707.

[Schlitt 1995] Schlitt HA, Heller L, Aaron R, Best E, Ranken DM. Evaluation of Boundary Element Methods for the EEG Forward Problem: Effect of Linear Interpolation. IEEE Trans Biomed Eng 1995. 42:52-58.

[Seger 2005] Seger M, Fischer G, Modre R, Messnarz B, Hanser F, Tilg B. Lead field computation for the electrocardiographic inverse problem: finite elements versus boundary elements. Comput Methods Programs Biomed 2005. 77:241-252.

[Seger 2006] Seger M, Modre R, Pfeifer B, Hintermüller C, B Tilg. Non-invasive Imaging of Atrial Flutter. Computing in Cardiology 2006. 33:601-604.

[Shah 2003] Shah D, Haïssaguerre M, Jais P, et al. Nonpulmonary vein foci: do they exist? Pacing Clin Electrophysiol 2003. 26:1631-1635.

[Skanes 1998] Skanes AC, Mandapati R, Berenfeld O, Davidenko JM, Jalife J. Spatiotemporal periodicity during atrial fibrillation in the isolated sheep heart.Circulation 1998. 98:1236-1248.

[SippensGroenewegen 1998] SippensGroenewegen A, Roithinger F.X, Peeters H.A.P, Linnenbank AC, van Hemel NM, Steiner PR, Lesh MD. Body surface mapping of atrial arrhythmias - atlas of paced P wave integral maps to localize the focal origin of right atrial tachycardia. J Electrocardiol 1998. 31:85-91.

[SippensGroenewegen 2000] SippensGroenewegen A, Lesh M.D, Roithinger F.X, Ellis W.S, Steiner P.R, Saxon L.A, Lee R.J, Scheinman M.M. Body surface mapping of counterclockwise and clockwise typical atrial flutter: A comparative analysis with endocardial activation sequence mapping. J Am Coll Cardiol 2000.

35:1276-1287.

[Stenroos 2008] Stenroos M, Haueisen J. Boundary element computations in the forward and inverse problems of electrocardiography: comparison of collocation and Galerkin weightings. IEEE Trans Biomed Eng 2008. 55:2124-2133.

[Stenroos 2009] Stenroos M. The transfer matrix for epicardial potential in a piece-wise homogeneous thorax model: boundary element formulation. Phys Med Biol 2009. 54:5443-5455.

[Sueda 2001] Sueda T, Imai K, Ishii O, Orihashi K, Watari M, Okada K. Efficacy of pulmonary vein isolation for the elimination of chronic atrial fibrillation in cardiac valvular surgery. Ann Thorac Surg 2001. 71:1189-1193.

[Taccardi 1963] Taccardi B. Distribution of heart potentials on the thoracic surface of normal human subjects. Circ Res 1963. 12:341-352.

[Tikhonov 1963] Tikhonov AN. On the solution of incorrectly posed problems and the method of regularization. Sov Math Dokl 1963. 4:1035-1038.

[Twomey 1963] Twomey S. On the numerical solution of Fredholm integral equations of the first kind by the inversion of the linear system produced by quadrature. JACM 1963. 10: 97-101.

[Urie 1978] Urie PM, Burgess MJ, Lux RL, Wyatt RF, Abildskov JA. The electrocardiographic recognition of cardiac states at high risk of ventricular arrhythmias. Circ Res 1978. 42:350-358.

[Verma 2011] Verma A, Lakkireddy D, Wulffhart Z, Pillarisetti J, Farina D, Beardsall M, Whaley B, Giewercer D, Tsang B, Khaykin Y. Relationship between complex fractionated electrograms (CFE) and dominant frequency (DF) sites and prospective assessment of adding DF-guided ablation to pulmonary vein isolation in persistent atrial fibrillation (AF). J Cardiovasc Electrophysiol 2011. 22:1309-1316.

[Wahha 1977] Wahha G. Practical approximate solutions to linear operator equations when the data are noisy. SIAM J NumAnal 1977. 14:651-661.

[Walker 1987] Walker S, Kilpatrick D: Forward and inverse electrocardiographic calculations using resistor network models of the human torso. Circ Res 1987. 61:504-513.

[Waller 1887] Waller AD. A demonstration on man of electromotive changes accompanying the heart's beat. J Physiol 1887. 8:229-234.

[Wang 2007] Wang Y, Schuessler RB, Damiano RJ, Woodard PK, Rudy Y. Noninvasive electrocardiographic imaging (ECGI) of scar-related atypical atrial flutter. Heart Rhythm 2007. 4:1565-1567.

[Wilson 1944] Wilson FN, Johnston FD, Rosenbaum FF, Erlanger H, Kossmann CE, Hecht H, Cotrim N, Menezes de Olivieira R, Scarsi R, Barker PS. The precordial electrocardiogram. Am Heart J 1944. 27:19-85.

[Wilde 2002] Wilde AA, Antzelevitch C, Borggrefe, Brugada J, Brugada R, Brugada P, Corrada D, Hauer RNW, Nademanee K, Priori S.G, Towbin J.A. Proposed diagnostic criteria for the Brugada syndrome. Eur Heart J 2002. 23:1648-1654.

[Wilde 2010] Wilde AA, Postema PG, Di Diego JM, Viskin S, Morita H, Fish JM, Antzelevitch C. The pathophysiological mechanism underlying Brugada syndrome: depolarization versus repolarization. J Mol Cell Cardiol 2010. 49:543-553.

[Winfree 1978] Winfree AT. Stably rotating patterns of reaction and diffusion. Theor Chem 1978. 4:1-51.

[Yamashita 1984] Yamashita Y, Takahashi T: Use of the finite element method to determine epicardial from body surface potentials under a realistic torso model. IEEE Trans Biomed Eng 1984. BME-31:611-621.

[Yan 1999] Yan GX, Antzelevitch C. Cellular basis for the Brugada syndrome and other mechanisms of arrhythmogenesis associated with ST-segment elevation. Circulation 1999. 100:1660-1666.

[Zhang 2013] Zhang J, Desouza KA, Cuculich PS, Cooper DH, Chen J, Rudy Y. Continuous ECGI mapping of spontaneous VT initiation, continuation, and termination with antitachycardia pacing. Heart Rhythm 2013. 10:1244-1245.